HYBRID/TANDEM LASER-ARC WELDING OF THICK LOW CARBON MARTENSITIC STAINLESS STEEL PLATES

by

Fatemeh MIRAKHORLI

MANUSCRIPT-BASED THESIS PRESENTED TO
ÉCOLE DE TECHNOLOGIE SUPÉRIEURE
IN PARTIAL FULFILLMENT FOR THE DEGREE OF
DOCTOR OF PHILOSOPHY
PH.D

MONTREAL, 19 SEPTEMBER 2016

ÉCOLE DE TECHNOLOGIE SUPÉRIEURE
UNIVERSITÉ DU QUÉBEC

Fatemeh MIRAKHORLI, 2016

.

This Creative Commons licence allows readers to download this work and share it with others as long as the author is credited. The content of this work can’t be modified in any way or used commercially.

BOARD OF EXAMINERS

THIS THESIS HAS BEEN EVALUATED

BY THE FOLLOWING BOARD OF EXAMINERS

Prof. Tan Pham, Thesis Director
Département de génie mécanique, École de technologie supérieure

Prof. Jean-Luc Fihey, Thesis Co-director
Département de génie mécanique, École de technologie supérieure

Dr. Xinjin Cao, Thesis Co-supervisor
Structures, Materials and Manufacturing Laboratory
National Research Council Canada-Aerospace

Prof. Mohammad Jahazi, Member of the jury
Department of Mechanical Engineering at École de technologie supérieure

Prof. Patricio Mendez, External Evaluator
Department of Chemical and Materials Engineering, University of Alberta

THIS THESIS WAS PRESENTED AND DEFENDED

IN THE PRESENCE OF A BOARD OF EXAMINERS AND PUBLIC

7 SEPTEMBER 2016

AT ÉCOLE DE TECHNOLOGIE SUPÉRIEURE

This thesis is dedicated to the memory of my parent, my mom, who was my inspiration for education and my dad who supported me unconditionally throughout my life. I miss you every day but your belief in my abilities is always with me and encouraged me to continue to grow and succeed.

ACKNOWLEDGMENT

First, I express my sincere gratitude to my director, Professor Tan Pham for giving me the opportunity to conduct this research under his supervision. Thank you Tan, for your support and encouragement at every important moment of this project. Through your guidance and support, you have taught me to become an independent and critical thinker. Without your consistent and enlightening support, this thesis would not have reached its present form.

I would also like to extend my appreciation to my co-director, Professor Jean-Luc Fihey for his valuable support and advice. This project would not have been successful without your timely assistance. Undoubtedly, you were one of the most influential person during my Ph.D.

I would like to extend my special thanks to my co-supervisor Dr. Xinjin Cao for having devoted so much time to pass on his knowledge to me. In all our discussions he always had tough questions and inspiring ideas to provoke further thinking. From our discussions, I learned a lot about how to be an academic researcher. Many thanks for your extensive comments and input that made this work possible.

Also, I would like to thank Professor Mohammad Jahazi for his insightful comments which encouraged me to widen my research from various perspectives.

I extend my sincere thanks to the other committee members: Prof Simon Joncas and prof, Patricio Mendez for their advice during my research.

I would also like to give thanks and a special acknowledgement to Dr. Priti Wanajara and Dr. Florent Bridier for providing valuable comments supporting me to improve my publications.

My sincere thanks also go to Dr. Denis Thibault, Dr. Michel Sabourin and Mr. Louis Mathieu for their support and suggestion during the project. This dissertation would not have been possible without the financial support of GE Renewable Energy (formerly Alstom Renwable Power Canada) and Natural Sciences and Engineering Research Council of Canada (NSERC).

I extend my sincere thanks to all members of the materials laboratory at ETS, and all those who contributed directly or indirectly to this dissertation. In particular, thanks to Radu Romanica, Mario Corbin, Olivier Bouthot and Dr. Hossein Monajati for their support and consideration. My sincere thanks extend to all my colleagues at NRC-Aerospace, in particular, Eric Poirier and Xavier Pelletier for their technical assistance during the welding experiments and metallographic preparation.

My sincere thanks also go to my colleagues from NOVIKA Company who gave me access to their laboratory and welding facilities. Special thanks to Lorraine Blais, Michaël Saucier and Mathieu Foster for all their help, interest, and valuable advice.

I would like to thanks to my friends and colleagues at ETS for their accompanying and support during the hard and the joyful times.

I am particularly grateful to my partner, Martin, for his friendship and putting me up when I needed a break from the thesis work and inspired me to hold tight to my work, no matter how complicated it gets.

Last but not the least; I would like to give my special thanks to my family, particularly my sister and my brothers for their understanding, support, patience, and presence in spite of the distance between us.

ÉTUDE DU SOUDAGE HYBRIDE LASER-ARC DE PLAQUES ÉPAISSES EN ACIER INOXYDABLE MARTENSITIQUE À BAS CARBONE

Fatemeh MIRAKHORLI

RÉSUMÉ

Lorsqu'il est question de produire des turbines pour l'industrie de l'hydroélectricité, il est crucial d'atteindre de hauts standards d'efficacité dans le processus de production et de maximiser la durée de vie à long terme du produit final. Des plaques épaisses d'acier inoxydable martensitique à faible carbone sont couramment utilisées pour la fabrication de ce type de turbine. Le soudage des composantes d'une turbine à hydroélectricité est un défi considérable, car les pièces à assembler sont de très grande dimension. Le procédé conventionnel de soudage requiert dans ce cas des préparations très larges et un soudage en plusieurs passes pour remplir la préparation, ce qui génère d'assez grandes zones de fusion et élargit la zone affectée par la chaleur.

Le nouveau procédé de soudage hybride/tandem laser-arc a été développé pour offrir un rendement très avantageux dans la production et pour améliorer la qualité globale des roues de turbines hydroélectriqu. C'est en combinant l'énergie à haute densité et la rapidité du soudage au laser, avec la facilité de remplissage du soudage à l'arc, que ce nouveau procédé a le potentiel d'augmenter la productivité et de diminuer la quantité de consommable.

L'objectif général de cette recherche est de mieux expliquer les multiples problèmes reliés au soudage hybride laser-arc dans l'assemblage de plaques épaisses d'acier inoxydable martensitique à faible carbone (13%Cr – 4%Ni), et de trouver des solutions pour réduire le nombre de passes nécessaires au soudage du joint avec ce procédé développé assez récemment.

La qualité du joint de soudage a été examinée au niveau de la microstructure afin d'évaluer les défauts et les propriétés mécaniques directement après le soudage et après le traitement thermique. Une attention particulière a été portée au procédé hybride/tandem laser-arc ainsi qu'passe d'amorçage à la racine.

En visant le soudage de différentes épaisseurs de plaques d'acier inoxydable martensitique à faible carbone, cette recherche se concentre sur deux objectifs particuliers:

- le soudage en une seule passe avec le procédé de soudage hybride laser-arc de l'acier inoxydable martensitique à faible carbone d'une épaisseur de 10 mm
- Le soudage en plusieurs passes avec le procédé hybride/tandem laser-arc de l'acier inoxydable martensitique à faible carbone d'une épaisseur de 25 mm.

Mots clés : soudage hybride laser-arc, acier inoxydable martensitique à faible carbone, microstructure, propriétés mécaniques, traitement thermique après soudage.

HYBRID/TANDEM LASER-ARC WELDING OF THICK LOW CARBON MARTENSITIC STAINLESS STEEL PLATES

Fatemeh MIRAKHORLI

ABSTRACT

High efficiency and long-term life of hydraulic turbines and their assemblies are of utmost importance for the hydropower industry. Usually, hydroelectric turbine components are made of thick-walled low carbon martensitic stainless steels. The assembly of large hydroelectric turbine components has been a great challenge. The use of conventional welding processes involves typical large groove design and multi-pass welding to fill the groove which exposes the weld to a high heat input creating relatively large fusion zone and heat affected zone.

The newly-developed hybrid/tandem laser-arc welding technique is believed to offer a highly competitive solution to improve the overall hydro-turbine performance by combining the high energy density and fast welding speed of the laser welding technology with the good gap bridging and feeding ability of the gas metal arc welding process to increase the productivity and reduce the consumable material.

The main objective of this research work is to understand different challenges appearing during hybrid laser-arc welding (HLAW) of thick gauge assemblies of low carbon 13%Cr-4%Ni martensitic stainless steel and find a practical solution by adapting and optimizing this relatively new welding process in order to reduce the number of welding passes necessary to fill the groove gap. The joint integrity was evaluated in terms of microstructure, defects and mechanical properties in both as-welded and post-welded conditions. A special focus was given to the hybrid and tandem laser-arc welding technique for the root pass.

Based on the thickness of the low carbon martensitic stainless steel plates, this work is mainly focused on the following two tasks:

- Single pass hybrid laser-arc welding of 10-mm thick low carbon martensitic stainless steel
- Multi-pass hybrid/tandem laser-arc welding of 25-mm thick martensitic stainless steel

Keywords: Hybrid laser-arc welding; Low carbon martensitic stainless steel; Microstructure; Mechanical properties; Post-weld heat treatment.

PUBLICATIONS

Parts of the work presented in this thesis have been published by the authors in the following articles;

- Mirakhorli, F., Cao, X., Pham, X. T., Wanjara, P., & Fihey, J. L. Phase Structures and Morphologies of Tempered CA6NM Stainless Steel Welded by Hybrid Laser-Arc Process, Mater. Charact., submitted, 2016.

- Mirakhorli, F., Cao, X., Pham, X. T., Wanjara, P., & Fihey, J. L. Hybrid Laser-Arc Welding of 10-mm-Thick Cast Martensitic Stainless Steel CA6NM: As-Welded Microstructure and Mechanical Properties, Metall. Mater. Trans. A, 47 (7), 2016, 3545–3563.

- Mirakhorli, F., Cao, X., Pham, X. T., Wanjara, P., & Fihey, J. L. Post-Weld Tempered Microstructure and Mechanical Properties of Hybrid Laser-Arc Welded Cast Martensitic Stainless Steel CA6NM, Metall. Mater. Trans. B, in press, 2016, 1-12.

- Mirakhorli, F., Cao, X., Pham, X. T., Wanjara, P., & Fihey, J. L. Technical Challenges in Narrow-Gap Root Pass Welding during Tandem and Hybrid Laser-Arc Welding of a Thick Martensitic Stainless Steel, Mater. Sci. Forum, in press, 2017.

- Mirakhorli, F., Cao, X., Pham, X. T., Wanjara, P., & Fihey, J. L. Hybrid Laser-Arc Welding of CA6NM: Post-Weld Tempered, Microstructure and Mechanical Properties, COM 2015, Toronto, Canada, 2015, 1-16.

- Mirakhorli, F., Cao, X., Pham, X. T., Wanjara, P., & Fihey, J. L: Hybrid Fiber Laser–Arc Welding of 10-mm Thick CA6NM Stainless Steel, MS&T 2014 Conf., Pittsburgh, PA, USA, 2014, 1891-900.

TABLE OF CONTENTS

Page

INTRODUCTION 1

CHAPTER 1 LITERATURE REVIEW 7
1.1 Hybrid laser-arc welding principle 7
1.2 Different parameters in hybrid laser arc welding 9
  1.2.1 Distance between laser and arc 10
  1.2.2 Relative position of the heat sources 11
1.3 Hybrid laser-arc welding of thick plates 12
1.4 Low carbon 13%Cr-4%Ni martensitic stainless steels 15
  1.4.1 Different phases in low carbon martensitic stainless steels 15
    1.4.1.1 Martensite 15
    1.4.1.2 Delta ferrite 17
    1.4.1.3 Austenite 17
  1.4.2 Welding metallurgy of low carbon 13%Cr 4%Ni martensitic stainless steels 17
1.5 Summary 18

CHAPTER 2 HYBRID LASER-ARC WELDING OF 10-MM THICK CAST MARTENSITIC STAINLESS STEEL CA6NM: AS-WELDED MICROSTRUCTURE AND MECHANICAL PROPERTIES 21
2.1 Introduction 23
2.2 Experimental procedures 24
2.3 Results and discussion 28
  2.3.1 Weld bead geometry 28
  2.3.2 Weld defects 29
  2.3.3 Microstructures 33
    2.3.3.1 Base metal 34
    2.3.3.2 Fusion zone 35
    2.3.3.3 Heat-affected zones 38
  2.3.4 Mechanical properties 43
    2.3.4.1 Microindentation hardness 43
    2.3.4.2 Tensile properties 46
    2.3.4.3 Charpy impact properties 50
2.4 Conclusions 52

CHAPTER 3 POST-WELD TEMPERED MICROSTRUCTURE AND MECHANICAL PROPERTIES OF HYBRID LASER-ARC WELDED CAST MARTENSITIC STAINLESS STEEL CA6NM 59
3.1 Introduction 60
3.2 Experimental 62
3.3 Results and discussion 65

3.3.1 Macrostructure ... 65
3.3.2 Microstructure ... 66
3.3.3 Microindentation hardness ... 71
3.3.4 Tensile strength ... 74
3.3.5 Charpy impact property ... 78
3.4 Conclusions ... 80

CHAPTER 4 PHASE STRUCTURES AND MORPHOLOGIES OF TEMPERED CA6NM STAINLESS STEEL WELDED BY HYBRID LASER-ARC PROCESS ... 85
4.1 Introduction ... 87
4.2 Material and experimental procedures ... 89
4.3 Results and discussion ... 91
4.3.1 Base metal ... 92
4.3.2 Fusion zone ... 92
4.3.3 Heat affected zone microstructure ... 102
4.3.4 Microindentation hardness ... 107
4.4 Conclusions ... 109

CHAPTER 5 TECHNICAL CHALLENGES IN NARROW-GAP ROOT PASS WELDING DURING TANDEM AND HYBRID LASER-ARC WELDING OF A THICK MARTENSITIC STAINLESS STEEL ... 115
5.1 Introduction ... 116
5.2 Experimental ... 116
5.3 Results and discussion ... 119
5.3.1 Thermal cycles ... 119
5.3.2 Weld macrographs and defects ... 119
5.3.3 Microstructure ... 124
5.4 Conclusions ... 124

CHAPTER 6 HYBRID/TANDEM LASER-ARC WELDING OF 25-MM THICK 415SS PLATES WITH A NARROW-GAP GROOVE CONFIGURATION ... 127
6.1 Introduction ... 128
6.2 Experimental procedures ... 129
6.3 Results and discussion ... 132
6.3.1 Thermal cycles ... 132
6.3.2 Root pass geometry and macrostructure ... 133
6.3.3 Defects ... 140
6.3.1 Tensile tests ... 142
6.3.2 Charpy impact property ... 144
6.4 Conclusions ... 148

SUMMARIES ... 153

RECOMMENDATIONS FOR FUTUR WORK ... 157

LIST OF BIBLIOGRAPHICAL REFERENCES..159

LIST OF TABLES

Page

Table 2-1 Chemical composition of the cast CA6NM SS and ER410NiMo filler metal 25

Table 2-2 Experimental design for HLAW 26

Table 2-3 Ultimate tensile strength and impact energy obtained at different welding speeds........46

Table 3-1 Chemical composition of cast CA6NM stainless steel and ER410NiMo filler metal........63

Table 3-2 Experimental design for HLAW 64

Table 3-3 Microhardness of the FZ and HAZs in the tempered welds assembled at different welding speeds 73

Table 3-4 Tensile strength and impact energy of the tempered CA6NM welds assembled at different welding speeds 74

Table 4-1 Chemical composition of the CA6NM martensitic SS and ER410NiMo filler metal........89

Table 5-1 Chemical compositions of 410 SS plates and ER410NiMo filler wire (wt. %) 117

Table 5-2 Process parameters used for the root pass in the narrow groove and BOP tests 118

Table 6-1 Chemical compositions of 410 SS plates and ER410NiMo filler wire (wt. %) 130

Table 6-2 Process parameters used in the narrow groove 131

Table 6-3 Tensile property of the full joint respectively at the top and bottom of the weld........143

Table 6-4 Impact energy of the 415 SS root pass at two different preheating temperatures 146

LIST OF FIGURES

Page

Figure 1-1 Hybrid laser-arc welding process 7

Figure 1-2 Macrograph comparing the FZ of single-pass hybrid weld vs. a multiple conventional weld (Reutzel et al., 2008) 8

Figure 1-3 Schematic set-up for (a) hybrid and (b) tandem laser arc welding (Paul andNicolae, 2011) 8

Figure 1-4 The flow chart of process parameters in HLAW 9

Figure 1-5 Schematic representation of hybrid welding with leading arc and leading laser arrangement (Kah, Salminen and Martikainen, 2010) 11

Figure 1-6 Groove design and Cross section of the hybrid weld with thickness of 20 mm filled with four passes (Jokinen et al., 2003a) 13

Figure 1-7 Cross-section of 14 mm thick X70 material, single V-butt joint preparation, 6 mm root face and 45° include angle (Grünenwald et al., 2010) 14

Figure 1-8 Cross-section of the three-pass hybrid MAG/laser weld in 25 mm AH36 structural steel (Webster et al., 2008) 14

Figure 1-9 Pseudobinary Fe-Cr-Ni phase diagram (Folkhard et al., 1988) 16

Figure 1-10 Microstructural hierarchy of the lath martensite structure (Kitahara et al., 2006) 16

Figure 2-1 Specimen geometries for (a) transverse tensile and (b) Charpy impact tests (the FZ is centered within the demarcated shaded region 27

Figure 2-2 Welding defects observed in the transverse cross-sections and root surfaces at a low welding speed of 0.5 m/min and laser powers of (a) 4.2 and (b) 5.2 kW 28

Figure 2-3 Transverse cross-sections of welds manufactured at different welding speeds for the three welding processes: (a, b, c) HLAW, (d, e, f) LW and (g, h, i) MIG 31

Figure 2-4 Weld defects: (a) excessive penetration and underfill depth, and (b) total porosity (Note: root humping height is taken as excessive penetration at a welding speed of 0.5 m/min) 32

Figure 2-5 Macrostructure from the FZ to the BM (at 1.0 m/min welding speed) according to the equilibrium Fe-Cr-Ni phase diagram [15] 34

Figure 2-6 SEM image of the BM showing regions A and B that were analyzed using EDS; (b) EDS results for region A indicating it as the martensite matrix; (c) EDS results for region B indicating it as delta ferrite; and (d) XRD spectrum for the BM 35

Figure 2-7 FZ characteristics of the weld manufactured at a welding speed of 1.0 m/min. (a) OM image of the FZ macrostructure, (b) OM image of FZ along the weld centerline in region A, (c) FZ microstructure in region B, and (d) SEM micrograph of the FZ microstructre showing fine stringers of delta ferrite 36

Figure 2-8 SEM-EDS mapping of the elemental distribution in the FZ microstructure corroborating the presence of delta ferrite between the martensitic laths..38

Figure 2-9 Microstructural evolution in the various HAZs in the weld manufactured at a welding speed of 1.0 m/min. (a-b) HAZ2/3 interface, (c-d) HAZ2, (e-f) HAZ3, (g-i) HAZ4, (j-l) HAZ5 39

Figure 2-10 SEM-EDS mapping of the elemental distribution in HAZ5 42

Figure 2-11 (a-d) Hardness profiles at different welding speeds, (e) 2D hardness map for 1.0 m/min welding condition and (f) dependency of FZ hardness on welding speed 44

Figure 2-12 Microstructure near the tensile fracture surface of the weld assembled at a welding speed of 1.0 m/min with failure occurring exclusively in the BM 47

Figure 2-13 Tensile fracture surfaces of the welds assembled at different welding speeds...48

Figure 2-14 SEM-EDS analyses of the tensile fracture surfaces of the weld 49

Figure 2-15 Fracture surfaces of Charpy impact tested samples of the welds assembled at different welding speeds 51

Figure 3-1 Specimen geometries for (a) transverse tensile (where the FZ is centered within the demarcated shaded region) and (b) Charpy impact tests 64

Figure 3-2 Macrostructure showing the FZ and HAZ located within the gage length of a transverse tensile specimen (at a welding speed of 1.0 m/min), (b) typical porosity in the FZ, and (c) macrostructure from the FZ to the BM according to a Fe-Cr-Ni ternary diagram............65

Figure 3-3 BM microstructures by (a) OM and (b) SEM 67

Figure 3-4 FZ microstructure in the weld assembled at 1.0 m/min by (a,b) OM and (c) SEM...68

Figure 3-5 Microstructural evolution in the various HAZs of the weld assembled at 1.0 m/min 69

Figure 3-6 Hardness profiles of the tempered welds assembled at welding speeds of (a) 0.75 m/min, (b) 1.0 m/min, and (c) 1.2 m/min; (d) effect of welding speed on the FZ hardness (tempered condition).....72

Figure 3-7 Microstructure along the tensile load direction near the tensile fracture surface of the welds assembled at welding speeds of 0.75 m/min (a,d,g,j), 1.0 m/min (b,e,h,k) and 1.2 m/min (c,f,i,l)............75

Figure 3-8 Secondary electron images of the tensile fracture surfaces for the welds assembled at welding speeds of 0.75 m/min (a,d,g), 1.0 m/min (b,e,h) and 1.2 m/min (c,f,i) 77

Figure 3-9 Secondary electron imaging of the Charpy impact fracture surfaces for the welds assembled at welding speeds of 0.75 m/min (a,d,g,j), 1.0 m/min (b,e,h,k) and 1.2 m/min (c,f,I,l)..79

Figure 4-1 Schematic illustration showing lath α′ structure in low carbon steels [5]...87

Figure 4-2 (a) Transverse section of a welded joint obtained at a welding speed of 1.0 m/min, and (b) macrostructure from the FZ to the BM according to the 4% Ni pseudobinary section of the Fe-Cr-Ni ternary phase diagram [19]...92

Figure 4-3 BM characteristics (a) SEM image and (b) XRD spectrum.....................93

Figure 4-4 (a) FZ macrostructure with the weld centerline demarcated by the two arrows, (b,c) EBSD IQ map at positions I and II, (d,e) IPF orientation map at positions I and II (b1 and b2 refer to two diferent blocks), and (f,g) PF at positions I and II...94

Figure 4-5 (a) High magnification SEM image in FZ, (b) IPF orientation map, (c-d) misorientation map and angles between the adjacent points and their distribution, related to (a) 96

Figure 4-6 Different δ morphologies in the horizontal (top) view (a-e) and transverse sections (e-i) 98

Figure 4-7 (a,b) Reversed austenite in FZ and (c) XRD spectrum 100

Figure 4-8 SEM image in FZ (a) and its corresponding EBSD phase map (b), (c-d) γ/α′ OR between α′ and reversed γ within the FZ....101

Figure 4-9 Microstructural evolution in various HAZs. (a-b) HAZ2, (c-d) HAZ3, (e-f) HAZ4, (g-h) HAZ5 103

Figure 4-10 SEM image in HAZ5 (a) and its corresponding EBSD phase (b), (c-d) γ/α′ OR between α′ and reversed γ in HAZ5 105

Figure 4-11 Primary δ in (a-c) HAZ2, (d-f) HAZ3, (g) HAZ4, (h) HAZ5, and (i) BM 106

Figure 4-12 Microindentation hardness: (a) distribution map and (b) profile at mid-thickness....108

Figure 5-1 Schematic of (a) hybrid welding, (b) tandem welding, and (c) groove design 118

Figure 5-2 Thermal cycles for root pass weld #4 (a, b) and transverse cross-sections of the 5 welds (c-g) 120

Figure 5-3 Defects observed in the weld cross-sections 121

Figure 5-4 BOP GMAW using three different shielding gases 122

Figure 5-5 Microstructure of the BM and FZ (TLAW with 10 mm laser-arc distance, #4)....124

Figure 6-1 Narrow-gap groove design 130

Figure 6-2 Specimen geometries for (a) transverse tensile and (b) Charpy impact tests 132

Figure 6-3 Thermal cycles for root pass weld # 6 (a) at different maximum temperature, (b) higher magnification from 16 s to 32 s....133

Figure 6-4 Weld root surfaces at different laser powers, and hybrid or tandem laser-arc welding 134

Figure 6-5 Transverse sections of the welds manufactured at different welding conditions: (a-c) for the laser root pass, (d) hybrid, trial #2, (e-h) tandem trial #3-6, (i-k) full joint....135

Figure 6-6 Vapour pressure cutting simulation using laser power [15] 138

Figure 6-7 Longitudinal cross-section of the root pass welds at different laser-arc distances 139

Figure 6-8 Defects observed in the weld cross-sections: (a,b) porosity at the bottom of second and third passes , (c,d) crack in the filling passes 141

Figure 6-9 SEM-EDS mapping of the elemental distribution near the crack 142

Figure 6-10 Microstructure near the tensile fracture surface of the weld at bottom (left side in figures (a-e) and top (right side in figures (f-j) of the joint 144

Figure 6-11 Tensile fracture surface of the weld at bottom (a-c) and top (d-f) of the full joint 145

Figure 6-12 Fracture direction after Charpy impact test: (a) trial #3, and (b) trial #4 146

Figure 6-13 Charpy fracture surfaces of root pass: trial#3 (a-c) and trial #4 (d-f) 147

LIST OF ABREVIATIONS

γ	Austenite
δ	Delta ferrite
α'	Martensite
Ac_1	Temperature at which austenite begins to form during heating
Ac_3	Temperature at which transformation of ferrite to austenite is completed during heating
Ac_4	Temperature at which austenite transforms to delta ferrite during heating
Ac_5	Temperature at which transformation of austenite to delta ferrite is completed during heating
BM	Base metal
BOP	Bead-on-plate
EBSD	Electron backscatter diffraction
EBW	Electron beam welding
EDS	Energy-dispersive X-ray spectroscopy
FCAW	Flux core arc welding
FE SEM	Field emission scanning electron microscope
FZ	Fusion zone
GMAW	Gas metal arc welding
HAZ	Heat-affected zone
HLAW	Hybrid laser-arc welding
IPF	Inverse pole figure
IQ	Image quality
K-S	Kurdjumov–Sachs
LW	Laser weld
MAG/MIG	Metal active gas/ metal inert gas
M_f	Martensite finish temperature
M_s	Martensite start temperature
ND	Normal direction

OM	Optical microscope
OR	Orientation relationship
PAGB	Prior austenite grain boundary
PF	Pole Figure
PMZ	Partially melted zone
PWHT	Post weld heat treatment
SEM	Scanning electron microscope
SS	Stainless steels
TD	Transverse direction
TLAW	Tandem laser-arc welding
WD	Welding direction
WFR	Wire feed rate
XRD	X-ray diffraction

INTRODUCTION

Successful joining and assembly of relatively thick-section components is an outstanding challenge in many heavy industries like shipbuilding, nuclear power plant, piping and hydropower manufacturing. The complexity of geometry, design and accessibility make joining process a key factor for the fabrication of large components. Among them, assembly and joining of hydroelectric power sub-components e.g. runner blade, crown and band is of great concern since they have large and complex geometries and are usually fabricated from martensitic stainless steels such as CA6NM and AISI 415, with thickness varying from 12 to 100 mm.

Presently for welding of turbine components, conventional arc welding techniques such as manual and/or semi-automatic gas metal arc welding (GMAW) and flux core arc welding (FCAW) are widely applied due to the relatively-low investment costs of these processes, process flexibility for wide gap tolerance, and the possibility of adding filler metal and thus controlling the fusion zone (FZ) composition. The main challenges associated with these conventional welding processes during manufacturing and/or repairing of hydroelectric turbine segments are the high heat input which imposes relatively-large heat affected zone (HAZ), high residual stresses and distortion, expansive groove machining for the thick-gauge sections which leads to the large number of passes necessary to fill the groove and consequently high amount of consumable material such as filler metal and shielding gas. Additionally, the relatively low speed processes with limited depth of penetration lead to very low productivity especially if we consider the time and cost for welding repair and training of skilled welders. Hence developing an advanced welding technique to improve the weld productivity and performance with low fabrication cost is essential, especially in heavy industry like hydroelectric turbine manufacturing.

Coupled laser-arc welding methods can be a promising alternative technique for joining of relatively thick gauge sections by providing beneficiary characteristics such as competitively high welding speed, deep penetration, low heat-input and consequently narrow FZ and HAZ, limited residual stress and distortion.

The first attempts to combine the laser and arc as a new welding technique to produce a unique weld pool (hybrid laser-arc welding) has been carried out by Steen and Eboo over two decades ago (Steen, 1980; Steen, 1979) and the investigation outcomes demonstrated that the combination of both laser beam and arc, impinging on the same weld pool, is more than a simple combination of the two heat sources. Tandem laser-arc welding (TLAW) technique is also a possibility of coupling two different heating sources in which laser and arc act separately, making two separate molten pools in a single-pass weld (Kah, 2012). To better understand the synergistic interactions of the laser and arc heating sources, especially in hybrid laser-arc welding several researches have been performed (El Rayes et al., 2004; Kah et al., 2010; Le Guen et al., 2011). In spite of many potential benefits of the laser technology, this process has not been extensively investigated in heavy industries, specifically for multi-pass welding of thick sections with a narrow groove. In addition, the weldability of the low carbon martensitic stainless steel (widely used in hydro-turbine manufacturing) has not been well investigated in term of microstructural evolution in the FZ and HAZ and the mechanical properties of the welds. In particular, no research has ever been reported on the HLAW or TLAW of the low carbon martensitic stainless steels.

Objective

This research project is part of the CReFaRRE (Consortium de recherche en fabrication et réparation des roues d'eau) project in collaboration with Hybro-Quebec, IREQ, GE Renewable Energy and NRC-Aerospace, Canada. It pursues the main objective of hydro-turbine runner manufacturing research and repair with a specific attention on developing an alternative welding technique.

Considering the requirement for developing an advanced welding method, such as coupled laser-arc welding technique, for assembly of the thick low carbon martensitic stainless steel plates, this dissertation is aimed to understand the technical challenges in this welding process, establish the processing-structure-property interrelationships, and thus develop an alternative coupled laser-arc welding technique for joining of thick-gauge components, applicable in hydro-turbine manufacturing.

This work is defined in two major sections and each is focused on one specific objective:

Objective 1: To investigate single-pass hybrid laser-arc welding (HLAW) of 10-mm thick CA6NM alloy at 5.2 kW laser power.

1.1 To analyse the weldability and possible defects during single pass HLAW of CA6NM alloys.
1.2 To characterize the microstructure evolution and evaluate the mechanical properties of CA6NM welds in as-welded condition.
1.3 To investigate the effect of post-weld tempering on microstructure and mechanical properties of hybrid laser-arc welded CA6NM alloy.

Objective 2: To investigate multi-pass tandem and/or hybrid laser-arc welding of 25-mm thick martensitic stainless steels with narrow-gap grooves.

2.1 To understand the technical challenges in narrow-gap root pass welding during tandem and hybrid laser-arc welding of a thick martensitic stainless steel at 5.2 kW laser power.
2.2 To evaluate the process stability and mechanical properties during multi-pass tandem and/or hybrid laser-arc welding of 25-mm thick 415 SS.

Structure of Thesis

To cover the objectives outlined above, the document begins with an overview of the coupled laser-arc welding process, as given in chapter 1 to describe the basis for the new suggestion and proposal, such as the principle of this advanced welding method, the main parameters, their effects, and the major progress achieved in this aspect. This chapter also includes the brief survey of low carbon 13%Cr-4%Ni martensitic stainless steel including its properties.

Since this research thesis is arranged as an article-based document, each of the afterward chapters represents the scientific results and analyses already published in or submitted to journals. The first scientific article published from this work is presented in Chapter 2. It discusses the appropriate parameters for single pass HLAW of 10 mm-thick CA6NM alloys, in particular, the possible defects formation during HLAW of this material and the effect of welding speed on microstructure and mechanical properties (hardness, tensile strength and impact energy) at different welding speeds in as-welded condition. This chapter responds to the part 1.1 and 1.2 of the first objective as mentioned above.

The effect of post-weld tempering on general microstructure and mechanical properties of CA6NM alloys at different welding speeds is addressed in the second article which is presented in chapter 3. The third article of this work focuses specifically on the phase analysis and phase morphology change during welding of CA6NM alloy after post-weld tempering, presented in chapter 4. Chapters 3 and 4 together respond to part 1.3 of the first objective for this study.

The fifth chapter of this study focuses on the main challenge specifically in the root pass tandem/hybrid laser-arc welding of 25-mm thick martensitic stainless steel. Designing a narrow-gap groove and finding the appropriate welding parameters and conditions for the root pass welding are one of the main outcomes in this part. This part responds to part 2.1 of the second objective of this research.

Based on the results driven from the fifth Chapter, 15 kW laser power was used for root pass laser and coupled laser-arc welding of 415 SS. The groove design was improved according to laser power used and the results are presented in Chapter 6. Specifically the stability of root pass welding is analysed using different laser-arc distances and laser powers, the groove was filled using HLAW technique and the mechanical properties of the joint were evaluated. This part is matched to the 2.2 part of the objective 2.

Finally the last section of this research, summarizes and concludes the important scientific contribution of this thesis and allows the outcomes of this work to be linked together to fulfill the main objective of this work. The summary of this study extends the existing knowledge on hybrid/tandem laser-arc welding of thick plates, discusses the applicability of hybrid/tandem laser-arc welding of thick gauge sections, by taking into account the main challenges encountered during the application of this welding technique which has not been comprehensively investigated using a narrow-gap groove. In addition, this research brings new steps in further understanding and analysis of this advanced welding technique, particularly with its effect on microstructure and mechanical properties of low carbon 13%Cr-4%Ni martensitic stainless steels, followed by some recommendations for future works in this field.

CHAPTER 1

LITERATURE REVIEW

1.1 Hybrid laser-arc welding principle

Hybrid laser-arc welding is a process which combines laser and arc sources (Figure 1-1) in order to take the advantages and compensate the disadvantages of both methods. Different types of laser sources can be used for the HLAW process, such as CO2, Nd:YAG, fibre, diode and disk lasers, The high energy density laser beam provides characteristic such as deep penetration, high welding speed, low heat-input and root extension. The arc sources used are mostly GMAW but there are also industrial applications that use tungsten inert gas or plasma as the electric source. In contrast, conventional GMAW process offers the ability to add filler metal and control weld metal chemical composition and increase gap-bridge ability.

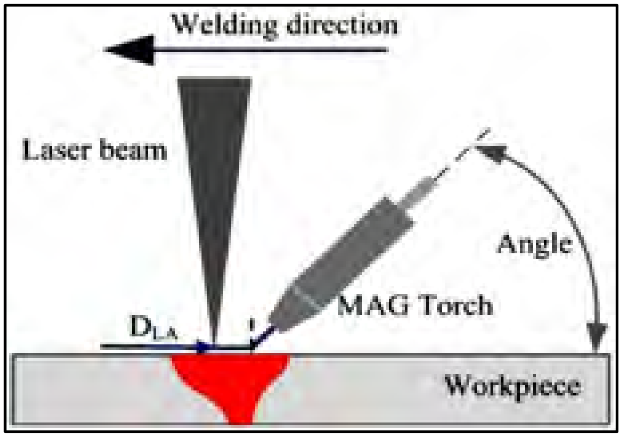

Figure 1-1 Hybrid laser-arc welding process

The comparison between the FZ of hybrid laser-arc weld with that of conventional arc welding for 12.7-mm thick plate is shown in Figure 1-2 which emphasises the effect of

HLAW process on reducing the amount of filler metal consumable, number of passes needed to fill the groove and FZ and HAZ areas.

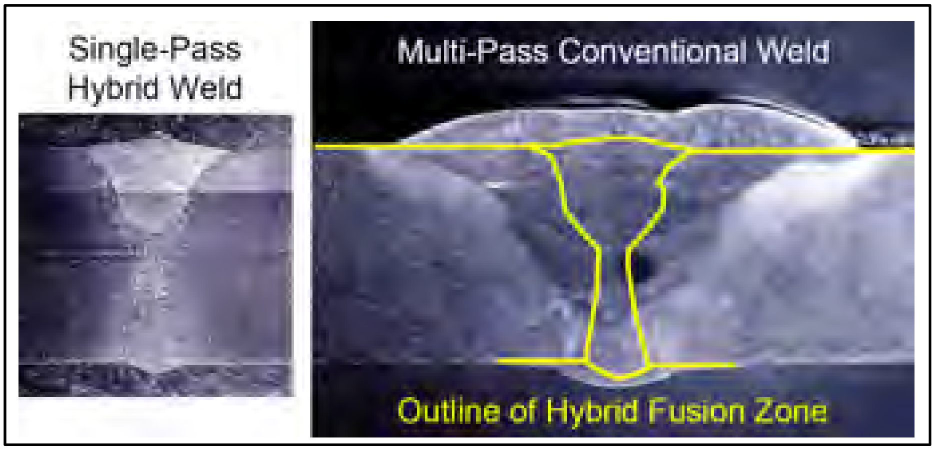
Single-Pass
Hybrid Weld
Multi-Pass Conventional Weld
Outline of Hybrid Fusion Zone

Figure 1-2 Macrograph comparing the FZ of single-pass hybrid weld vs. a multiple conventional weld (Reutzel et al., 2008)

Another possibility of hybrid welding, using two heat sources of laser and arc, is to use them in tandem mode, in which the two heat sources are separated from each other by increasing the laser-arc distance. In tandem laser-arc welding (TLAW), the arc and laser act separately on the workpiece and form two distinct molten pools (Ribic et al., 2009; Zhang et al., 2014a). The comparison between hybrid and tandem laser-arc welding is depicted in Figure 1-3.

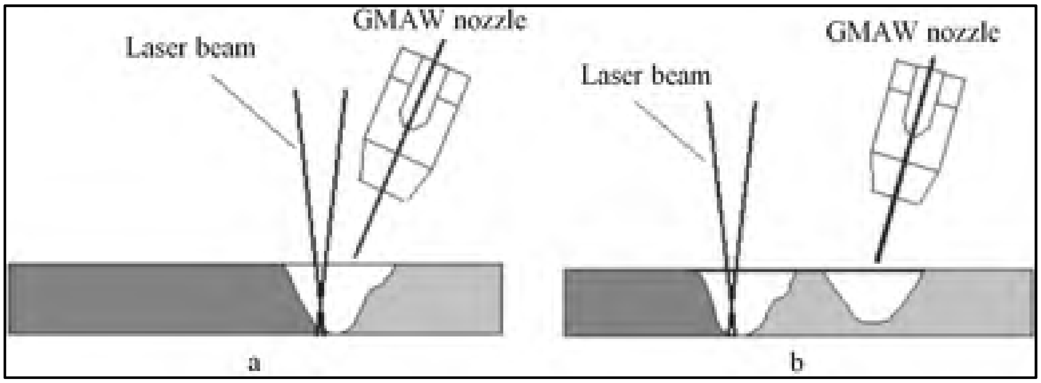
Laser beam
GMAW nozzle
a
Laser beam
GMAW nozzle
b

Figure 1-3 Schematic set-up for (a) hybrid and (b) tandem laser arc welding (Paul andNicolae, 2011)

1.2 Different parameters in hybrid laser arc welding

Hybrid laser-arc welding technique contains a large number of parameters as shown in figure 1-4.

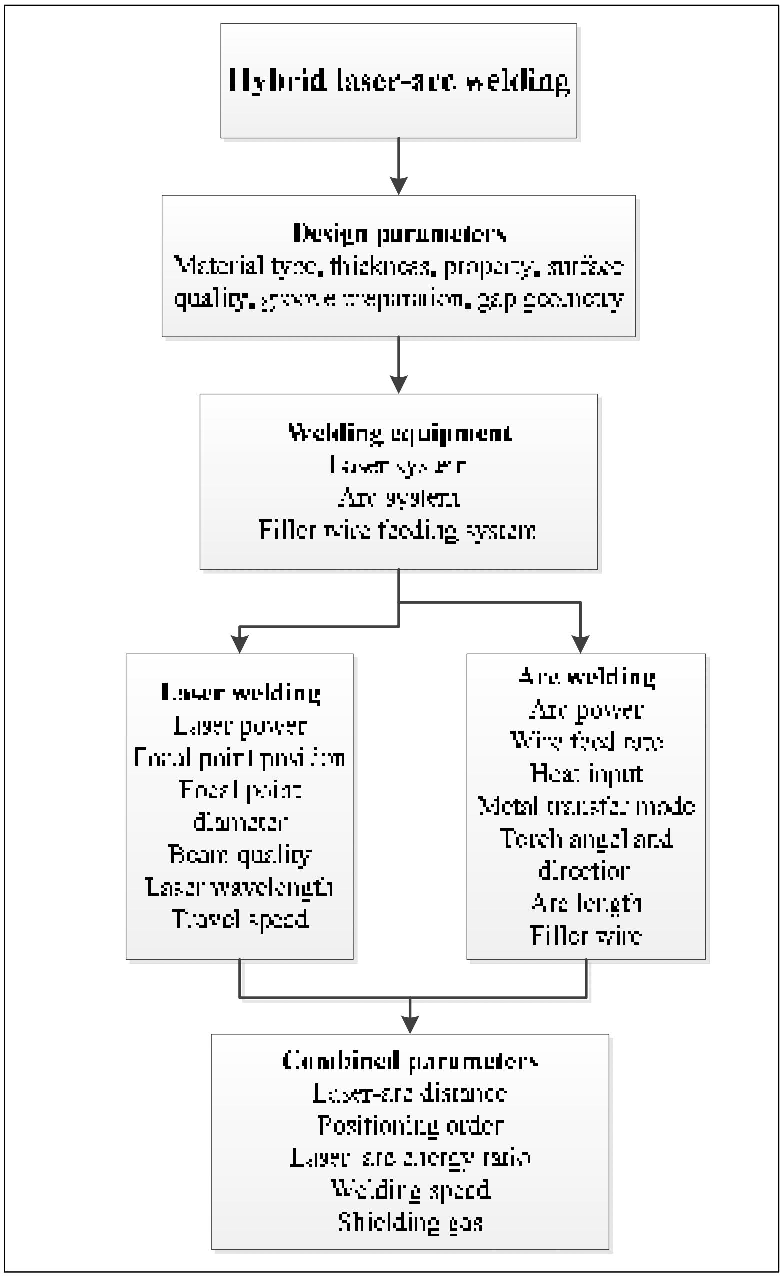
Hybrid laser-arc welding
Design parameters
Material type, thickness, property, surface quality, groove preparation, gap geometry
Welding equipment
Laser system
Arc system
Filler wire feeding system
Laser welding
Laser power
Focal point position
Focal point diameter
Beam quality
Laser wavelength
Travel speed
Arc welding
Arc power
Wire feed rate
Heat input
Metal transfer mode
Torch angel and direction
Arc length
Filler wire
Combined parameters
Laser-arc distance
Positioning order
Laser/arc energy ratio
Welding speed
Shielding gas

Figure 1-4 The flow chart of process parameters in HLAW

Besides the parameters related to the individual laser (e.g. laser power, travel speed, focal spot size, defocus distance…) and GMAW process (e.g. wire feed speed, arc length, current, intensity), some additional important parameters are added due to the interaction between laser and arc heating source such as: laser-arc distance and positioning order of heating source. (Olsen, 2009).

Accurate selection of HLAW parameters is very important in order to achieve appropriate joint assembly in terms of defect free weld, appropriate mechanical and metallurgical properties and improved productivity. In the following the main parameters are discussed.

1.2.1 Distance between laser and arc

The distance between laser and arc is a key parameter influencing the interaction between the laser beam and the arc plasma, and consequently the depth of penetration and weld geometry. When the distance between the laser and arc is short enough such as the plasma of individual processes interacts, they can form a united fusion zone and weld bead. For achieving the maximum penetration depth, the laser-arc distance should be within certain limits and it is when the plasma of individual processes combines, but at the same time the arc and filler metal should not disturb the key hole made by the laser. Specific differences in the distance lead to differences in penetration for the same parameters. According to (Zhao et al., 2009) researches, for an arc leading hybrid process, a deep penetration is acquired when the laser beam is placed just outside the arc, but within the vapour cloud surrounding the arc. However, penetration noticeably reduces when the laser beam moves into the center of the plasma arc. This is due to an absorption and reflection of the laser beam by the droplets and density of fumes in the plasma. In contrast, when the laser-arc distance is significantly long, then a laser beam cannot easily couple with the arc and there is no interaction between the arc and laser plasma. In this case, they form two separated welding pool and in this situation, the process is called tandem hybrid laser-arc welding (as shown in Figure 1-3). In this case it is just the laser beam which is responsible for penetration and the MIG process accompanies the laser, mostly for feeding the groove or compensate metal lost due to evaporation or spatter during welding (Bagger andOlsen, 2005). Different studies claim that the optimum distance between laser and arc to achieve stable process with good penetration during HLAW occurs at 1-3 mm (Bagger andOlsen, 2005), but in general defining an appropriate laser-arc distance must take into account the individual heating source characteristics like laser power, focal spot diameter, arc geometry which can affect the plasma and melting pool configurations formed by each process.

1.2.2 Relative position of the heat sources

The MIG torch in hybrid or tandem laser-arc welding can be positioned either in a leading or trailing position relative to the laser beam axis as shown in Figure 1-5.

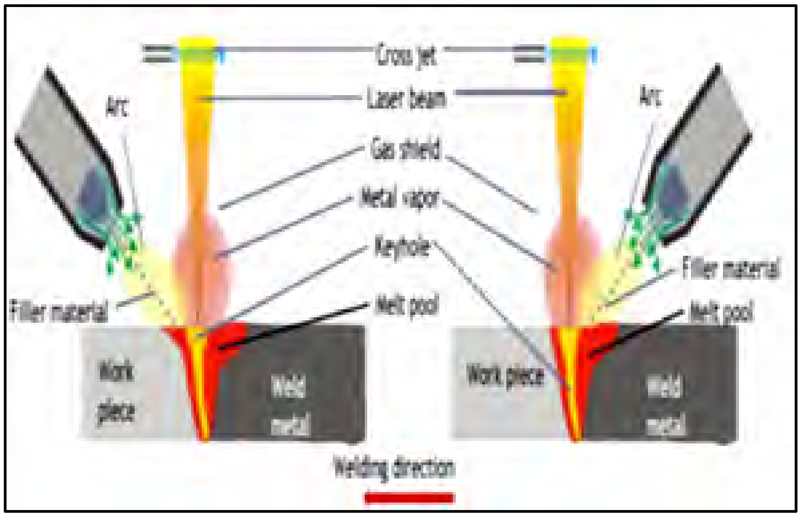
Cross jet
Laser beam
Arc
Arc
Gas shield
Metal vapor
Keyhole
Filler material
Filler material
Melt pool
Melt pool
Work piece
Work piece
Weld metal
Weld metal
Welding direction

Figure 1-5 Schematic representation of hybrid welding with leading arc and leading laser arrangement (Kah, Salminen and Martikainen, 2010)

Several researches have been performed on the effect of the laser leading hybrid technique (the laser beam precedes the arc) (Gao et al., 2008; Kim et al., 2008; Olsen, 2009) and of the arc leading hybrid technique (the arc precedes the laser beam) (Gao et al., 2008; LIU et al., 2006; Qin, 2007). For example Steen (Steen, 1980) found that the laser leading process could be appropriate regarding to the bead appearance. Because in this case the shielding gas flow, does not interfere with the molten pool created by the arc. Whereas in the leading arc arrangement, the shielding gas blows into the molten pool and disrupts the shape of the bead surface. But according to different researches, the arc leading arrangement gives a more stable arc and deeper penetration (Dilthey et al., 1999; Steen, 1980).

1.3 Hybrid laser-arc welding of thick plates

Laser and hybrid laser-arc welding of thick walled components has gained more attention recently using narrow-gap groove joint design. Conventional arc welding methods of thick gage plates are associated with large groove design which increases the number of passes necessary to fill the joint, thus increasing filler metal and gas consumable, the amount of heat input and consequently the FZ and HAZ areas. Accordingly, the narrow-gap single/multi-pass HLAW can be a promising method to reduce the mentioned problems during welding of thick components. Depending on the laser power and material thickness used, single or multi-pass hybrid laser-arc welding process can be applied. Several researches have been done on single pass laser welding of thick section plates, including full penetration butt joint of 20 mm and 25-mm thick structural steel plate with a 30 kW fiber laser (Sokolov et al., 2011) and deep penetration laser welding of 12-mm thick stainless steel plates using a 10 kW high-power fiber laser (Zhang et al., 2014b). Other researches have shown that laser-arc welding with a 4.5 kW diode pumped laser is capable of welding 12 mm steel plate in a single pass at 0.5 m/min weld travel speed (Reutzel et al., 2006). Single pass HLAW with 5 kW fiber laser was also investigated to obtain full penetration in 9.3-mm thick HSLA-65 using a butt joint Y-groove configuration. (Cao et al., 2011). Whereas laser power is the major factor in HLAW process to determine the maximum thickness that can be welded in a single pass, HLAW of very thick plates can be performed using multi-pass welding technique. The laser source in HLAW allows designing a narrow-gap groove to increase the productivity and reduce the FZ area. However in term of multi-pass HLAW few researches have been carried out, we can categorise them generally in three different steps as following;

1. Two steps weld; root pass with laser process and filling pass with hybrid process.
2. Two steps weld; root pass with hybrid process and filling pass with conventional arc.
3. Multi-pass welding with hybrid process for both root and filling passes.

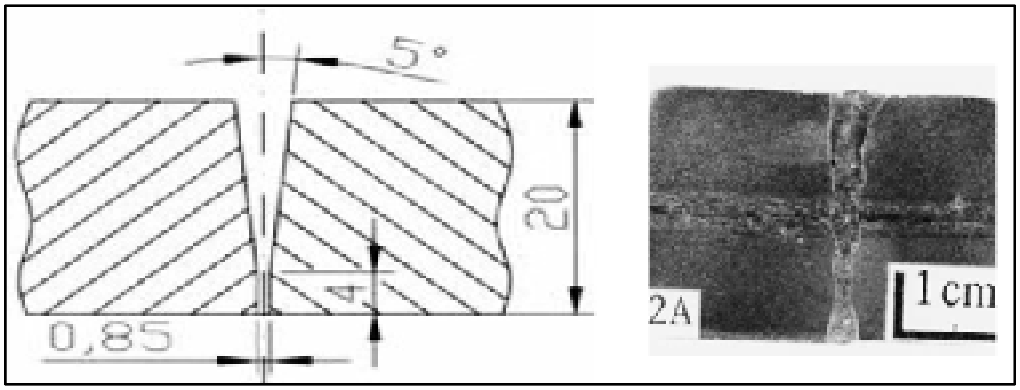

Figure 1-6 Groove design and Cross section of the hybrid weld with thickness of 20 mm filled with four passes (Jokinen et al., 2003a)

In the first cases, the weld is done in two separate steps. First, the root pass is welded with the laser process (with or without filler metal) to give the maximum penetration and second the filling pass is made using the hybrid laser welding to fill the groove. Multipass HLAW of 20-mm thick austenitic stainless steel was performed using a narrow-gap groove configuration (Figure 1-6) with a root face of 4 mm and included angle of 8 to 12° (Jokinen et al., 2003b). In this welding experiment, HLAW process was used after two passes made by laser welding with filler metal addition. The main interest in welding with a hybrid process for the narrow-gap configuration was to determine whether it is possible to have the arc inside a narrow groove.

In the second case, the root pass is performed using hybrid laser-arc welding process and the subsequent filling passes are accomplished using conventional arc welding processes. After the root has been fused, subsequent passes with keyhole-mode HLAW would re-melt and solidify the existing root pass and to avoid repeated re-melting, the groove is filled by the GMAW process alone. If the available laser power is insufficient to weld the entire joint thickness in a single pass, the joint can be designed to use a deep-penetration HLAW root pass, with subsequent filling passes using GMAW process (Grünenwald et al., 2010; Vollertsen et al., 2010). Figure 1-7a shows the cross-sections of a root pass using HLAW process, and Figure 1-7b displays filling pass using GMAW added to the root pass on 14 mm X70, with 8 kW laser power (Grünenwald et al., 2010).

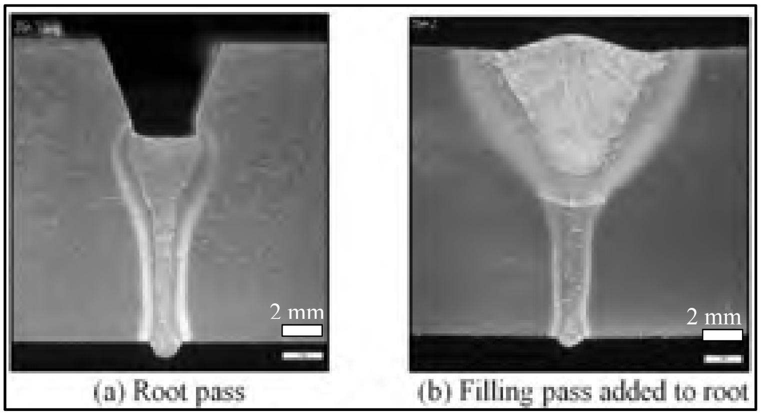

Figure 1-7 Cross-section of 14 mm thick X70 material, single V-butt joint preparation, 6 mm root face and 45° include angle (Grünenwald et al., 2010)

Another technique used for HLAW of thick plates is to perform all the passes with HLAW process. Few researches have been conducted with this method but it can be beneficial in terms of process time and productivity improvement. Weldability of AH36 structural steel has been investigated using multi-pass HLAW for thicknesses of 20 mm to 30 mm at maximum laser power of 17 kW. Three passes were used for fully welding 25 mm-thick plates (Figure 1-8) using a Y groove shaped with a 12 mm root face, full opening angle of 20°, and an initial gap of 0.5 mm.(Webster et al., 2008). However more details related to the challenges during multi-pass HLAW of thick plates was not discussed in this report.

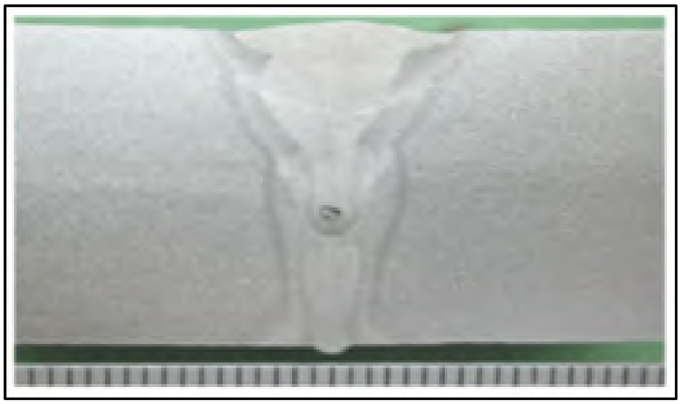

Figure 1-8 Cross-section of the three-pass hybrid MAG/laser weld in 25 mm AH36 structural steel (Webster et al., 2008)

1.4 Low carbon 13%Cr-4%Ni martensitic stainless steels

Low carbon 13%Cr-4%Ni martensitic stainless steels which are widely applied in hydraulic turbines, valve and high-pressure pipes manufacturing, are associated with the family of conventional martensitic stainless steels e.g., 410 and 420 SS. Low carbon 13%Cr-4%Ni martensitic stainless steels possess carbon content to values less than 0.06 wt.% and instead nickel is added to the percentages of 3.5-4.5 wt.% for stabilizing the austenite with addition of chromium (13-15% percentage) to increase the corrosion resistance of the alloy. Low carbon 13%Cr-4%Ni martensitic stainless steels are developed both as casting material (CA6NM) and wrought material (415 SS) especially for heavy section turbine manufacturing which, gives the combination of good impact properties, high strength and good weldability. Noteworthy that this material is generally used in annealed and tempered condition.

1.4.1 Different phases in low carbon martensitic stainless steels

Low carbon 13%Cr-4%Ni martensitic stainless steels solidify as delta ferrite according to the cooling path at 13 % Cr in the 4 % Ni pseudobinary section of Fe-Cr-Ni equilibrium ternary phase diagram (Figure 1-9) (Folkhard et al., 1988). The delta ferrite transforms to austenite at high temperature during cooling and the austenite transforms to non-equilibrium lath martensite structure. Other phases observed in this material are: delta ferrite, retained austenite and chromium carbides. Each phase is explained briefly in the following.

1.4.1.1 Martensite

The lath martensite is a predominat phase in low carbon martensitic stainless steels which is formed during diffusionless transformation of austenite to martensite upon cooling. This transformation is also athermal which means the amount of martensite formed does not depend on time, but only on the undercooling below the M_s temperature (Porter and Easterling, 1992).

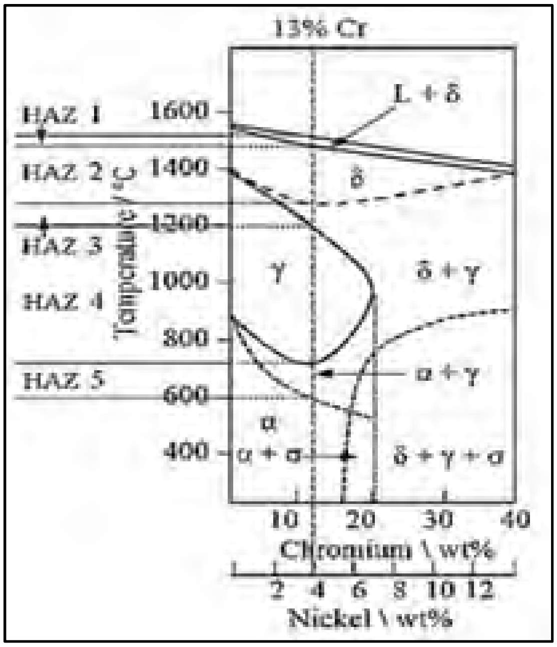

Figure 1-9 Pseudobinary Fe-Cr-Ni phase diagram (Folkhard et al., 1988)

The microstructural feature of lath martensite in general has a three-level hierarchy in its morphology; it is constituted of laths, blocks and packets as shown in Figure 1-10.

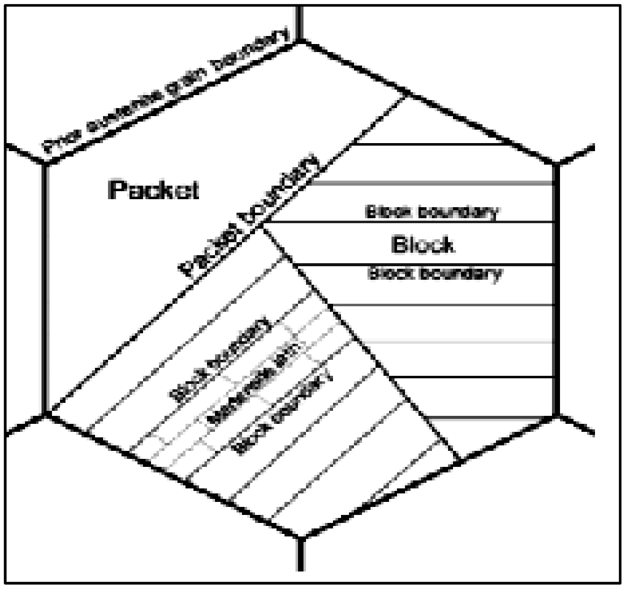
Prior austenite grain boundary
Packet
Packet boundary
Block boundary
Block
Block boundary
Block boundary
Martensite lath
Block boundary

Figure 1-10 Microstructural hierarchy of the lath martensite structure (Kitahara et al., 2006)

The lath is the smallest part of this structure which is a single crystal of martensite with a high amount of dislocations and lattice defects. Blocks are group of lathes with the same crystallographic orientation and packets are a group of blocks with the same habit plane.(Kitahara et al., 2006). To reveal all microstructure of lath martensite, high resolution electron microscopy is necessary.

1.4.1.2 Delta ferrite

Delta ferrite is another phase which forms in high temperature δ or $\gamma + \delta$ regions in the phase diagram (Figure 1-9) and can remains in the final microstructure due to a non-equilibrium solidification, predominantly at previous austenite grain boundaries. The ferrite stabilising elements such as, chromium, molybdenum and silicon are added to increase corrosion resistance and as a deoxidizer respectively.

1.4.1.3 Austenite

Austenite can be retained in the final microstructure due to an incomplete transformation of austenite to martensite or it can be formed as a reversed austenite during the tempering process. The formation of reversed austenite during tempering at ~ 600 °C is mostly due to the enrichment of austenite in elements such as nickel, carbon and nitrogen which strongly depresses the M_S temperature and consequently lead to formation of reversed austenite (Song et al., 2011)

1.4.2 Welding metallurgy of low carbon 13%Cr 4%Ni martensitic stainless steels

The fusion zone of low carbon martensitic stainless solidifies as delta ferrite, as the weld metal cools down in the solid state, the austenite will consume the delta ferrite, resulting in a fully austenitic structure below 1300 °C. The austenite will transform to martensite upon further cooling (Lippold et Kotecki, 2005) and the weld metal is expected to be fully martensite at room temperature, however residual delta ferrite may exist in the final microstructure due to the fast cooling rate and remains at previous austenite grain boundaries during cooling.

In low carbon martensitic stainless steels, the HAZ can be categorized into several zones (Carrouge, 2003; Thibault, 2010), corresponding to the different thermal cycles experienced during welding as shown on the pseudobinary phase diagram of Fe- 4%Ni -13% Cr in Figure 1-9. HAZ1 includes heating into the L + δ region and is often indicated as the partially melted zone (PMZ). HAZ2, refers to a single phase delta ferrite region where complete transformation of the BM microstructure to delta ferrite occurs during heating. HAZ3 corresponds to heating into the high temperature dual phase δ + γ region where partial transformation of the γ matrix to delta ferrite occurs during heating. HAZ4 is associated to the single phase γ region where the BM has completely transformed to austenite during heating. HAZ5 is the low temperature dual phase α' + γ region that is characterized by partial transformation of tempered martensite (α') to austenite during heating.

1.5 Summary

The definition of laser-arc welding technique (hybrid and tandem), the main parameters and the review of the recent works on hybrid laser-arc welding of thick plates were covered during this chapter. Much of the existing literature involves the use of hybrid welding for specific applications such as ship building and joining of structural and carbon steels thick section. A greater part of this research focused on optimising the parameters on bead-on plate HLAW and single pass laser and HLAW of structural steels. Few researches have been performed on multi-pass laser and HLAW of thick plates. In order to expand the application space for hybrid laser-arc welding, the current research concentrates on the single pass/ multipass hybrid and tandem laser-arc welding of thick martensitic stainless steels, applicable in hydro-turbine manufacturing. Parameter optimisation inside a narrow-gap groove, using coupled laser-arc welding has rarely been reported, and the amount of research on microstructural characterisation and mechanical properties of low carbon martensitic stainless using HLAW process is very limited. Thus it is worth to (1) characterize laser-arc welding technique in term of process parameters and appropriate groove design for welding of thick sections and (2) analyse the microstructure and mechanical properties of hybrid laser-arc weld 13%Cr-4%Ni low carbon martensitic stainless steel, applied in hydro-turbine manufacturing

CHAPTER 2

HYBRID LASER-ARC WELDING OF 10-MM THICK CAST MARTENSITIC STAINLESS STEEL CA6NM: AS-WELDED MICROSTRUCTURE AND MECHANICAL PROPERTIES

F. Mirakhorli[1,2], X. Cao[2] , X-T. Pham[1], P. Wanjara[2] and J. L. Fihey[1]

[1]École de technologie supérieure, Montréal, Québec, Canada, H3C 1K3
[2]National Research Council Canada – Aerospace, Montréal, Québec, Canada, H3T 2B2

This article has been published in Metallurgical and Materials Transactions A journal, 47(7), 2016, 3545-3563

Keywords: Welding and joining; Stainless steel; Microstructure studies (evolution); Mechanical testing.

Abstract

Cast CA6NM martensitic stainless steel plates, 10 mm in thickness, were welded using a hybrid laser-arc welding. The effect of different welding speeds on the as-welded joint integrity was characterized in terms of the weld bead geometry, defects, microstructure, hardness, ultimate tensile strength and impact energy. Significant defects such as porosity, root humping, underfill and excessive penetration were observed at a low welding speed (0.5 m/min). However, the underfill depth and excessive penetration in the joints manufactured at welding speeds above 0.75 m/min met the specifications of ISO 12932. Characterization of the as-welded microstructure revealed untempered martensite and residual delta ferrite dispersed at prior-austenite grain boundaries in the fusion zone. In addition, four different heat affected zones in the weldments were differentiated through hardness mapping and inference from the Fe-Cr-Ni ternary phase diagram. The tensile fracture occurred in the base metal for all the samples and fractographic analysis showed that the crack path is within the martensite matrix, along primary delta ferrite-martensite interfaces and within the primary delta ferrite. Additionally, Charpy impact testing demonstrated slightly higher fracture

energy values and deeper dimples on the fracture surface of the welds manufactured at higher welding speeds due to grain refinement and/or lower porosity.

NOMENCLATURE

γ	Austenite
δ	Delta ferrite
α'	Martensite
Ac_1	Temperature at which austenite begins to form during heating
Ac_3	Temperature at which transformation of ferrite to austenite is completed during heating
Ac_4	Temperature at which austenite transforms to delta ferrite during heating
Ac_5	Temperature at which transformation of austenite to delta ferrite is completed during heating
BM	Base metal
BOP	Bead-on-plate
EDS	Energy-dispersive X-ray spectroscopy
FCAW	Flux core arc welding
FZ	Fusion zone
GMAW	Gas metal arc welding
HAZ	Heat-affected zone
HLAW	Hybrid laser-arc welding
LW	Laser weld
MAG/MIG	Metal active gas/ metal inert gas
M_f	Martensite finish temperature
M_s	Martensite start temperature
OM	Optical microscope
SEM	Scanning electron microscope
WFR	Wire feed rate
XRD	X-ray diffraction

2.1 Introduction

To date, low carbon 13%Cr-4%Ni martensitic stainless steels are mainly used to manufacture hydraulic turbine components, such as turbine runners and guide vanes. For the majority of the assembly and repair work on these relatively large turbine components, conventional fusion welding processes, such as GMAW (gas metal arc welding) and FCAW (flux core arc welding), are commonly applied presently. However, these conventional arc welding processes involve several welding passes to fill the wide groove and, thus, high heat input, which increases distortion and generates large fusion and heat affected zones. In addition to the high consumable costs related to the filler metal and shielding gas consumption, these welding processes are usually performed in manual or semi-automated mode, which thus imparts a relatively high dependency of the product quality on the operator skills and a long manufacturing time is required for assembly of the component or repair of any defects. Hence, the introduction of advanced welding technologies offers considerable potential to eliminate or minimise these aforementioned issues.

Coupling a laser with arc welding, HLAW (hybrid laser-arc welding) is a relatively low heat input joining technology that combines the synergistic qualities of the high energy density laser beam for deep penetration at high welding speeds with the arc's tolerance for a wide fit-up gap via wire feeding [1, 2]. Thus, the two coupled heat sources (laser and arc) in the HLAW process lead to a lower number of welding passes and total heat input, which in turn reduces the weldment area, residual stress and distortion. Also, as compared to arc welding processes, the reduction in the amount of welding consumables and the higher welding speeds of the HLAW process render lower operational costs and reduced product time-to-market [1]. The combination of these advantages makes the HLAW process especially suitable for assembly of thick-gage section components. Previous work by the authors describes the possibility of using HLAW for single pass welding of CA6NM stainless steel [3], but the effect of the process parameters on the mechanical properties of the assembly have not yet been reported. Since the mechanical properties of the low carbon martensitic stainless steels strongly depend on the microstructural changes in the fusion zone (FZ) and

heat affected zone (HAZ) [4], a study on the inter-relationship between processing, structure and mechanical properties (hardness, toughness and ultimate tensile strength) is important.
In the present study, HLAW was applied to butt weld 10-mm thick CA6NM stainless steel using a single pass process with four different welding speeds, i.e. 0.5, 0.75, 1.0, and 1.2 m/min. The weld geometry, defects, FZ and HAZ microstructures, and microhardness evolution across the weldment were investigated. The ultimate tensile strength and toughness properties of the joints were also evaluated and correlated to the fracture surface characteristics through fractographic analysis.

2.2 Experimental procedures

CA6NM martensitic stainless steel plates with dimensions of 150 mm in length × 75 mm in width × 10 mm in thickness were extracted from a cast turbine runner blade that had a thickness range of 50 – 101 mm and a chemical composition as given in Table 2-1. It is noteworthy that prior to machining, the CA6NM turbine blade runner was heat treated in three stages: (1) normalization by heating at a rate of 60 K/hr (60°C/hr) to 1073 K (800°C) and soaking at this temperature for 8 hours, followed by heating at a rate of 25 K/hr (25°C/hr) to 1303 K (1030°C) and soaking at this temperature for 27 hours, (2) air cooling to a temperature below the martensite finish temperature (Mf) of 363 K (90°C), and (3) tempering by heating at a rate of 36 K/hr (36°C/hr) to 913 K (640 °C) and soaking at this temperature for 27 hours, followed by cooling at a rate of 25 K/hr (25°C/hr). The CA6NM plates were then prepared to form a Y-groove shape butt joint with a bevel angle of 30º and a root face size of 5 mm. Just before HLAW, the CA6NM plates were ground and cleaned with acetone and then fixed within a clamping device with a root opening (gap size) of ~0.2 mm. AWS ER410NiMo filler wire with a diameter of 1.14 mm and a chemical composition as given in Table 2-1 was used for the HLAW trials. A Fronius Trans Pulse Synergic 4000 CMT GMAW power supply was coupled with a IPG photonics 5.2 kW continuous wave (wavelength of 1070 nm) solid-state Yb-fiber laser equipped with a collimating lens of 200 mm, a focal lens of 300 mm and a fiber diameter of 0.2 mm, which produced a nominal focusing spot diameter of ~ 0.30 mm (with an actual measurement of 0.33 mm). The laser beam was focused at 2.5 mm under the top surface of the workpiece, while maintaining a laser-arc distance of 2 mm. During welding, the laser head was inclined 5° from the vertical plane perpendicular to the welding direction to avoid any damage from laser beam reflection. The angle between the electrode axis and the workpiece surface was 45°. To protect the molten weld pool during welding, the top surface of the workpiece was shielded using a mixture of 96% argon and 4% oxygen, fed by the MAG (metal active gas)/MIG (metal inert gas) torch nozzle at a flow rate of 23.6 l/min, while the bottom surface was shielded using argon at a flow rate of 9.5 l/min. In the present work, the HLAW trials were conducted in laser leading mode and optimization of the process was centered primarily on the welding speed. Table 2-2 lists the weld process parameters (laser power, welding speed, WFR, arc voltage and current) used in this study. The WFR (wire feed rate) was calculated according to the volume required to fill the groove.

Table 2-1 Chemical composition of the cast CA6NM SS and ER410NiMo filler metal

Elements (wt. %)	**Fe**	**C**	**Si**	**Mn**	**P**	**S**	**Cr**	**Ni**	**Mo**	**Cu**	**Other**
CA6NM	Bal.	0.041	0.45	0.75	0.032	0.008	13.28	4.31	0.520	0.071	0.11
410NiMo	Bal.	0.02	0.37	0.34	0.017	0.0009	12.18	4.57	0.42	0.12	-

For metallographic examination and microhardness evaluation, two transverse cross-sections were taken from each welded joint. The specimens were then mounted and subsequently ground and polished using automated processes. Specifically, the weld samples were ground using successively finer SiC papers from 220 grit to 1200 grit and then polished using 3 and 1 μm diamond suspensions with an alcohol based lubricant on silk polishing cloths. Beraha's reagent (1 g K2S2O5 + 20 ml HCl + 80 ml H2O) was used to reveal the martensite and delta ferrite phases in the microstructure. Alternatively, electro-etching in a 20% aqueous solution of NaOH at room temperature was used to reveal only the delta ferrite phase in the microstructure. The microstructure was observed with an inverted OM (Optical microscope) (Olympus GX71). The image analysis software (AnalySIS Five) on the OM was used to quantify the area and dimension of the porosity on the transverse sections and delta ferrite fraction in the BM and FZ microstructures. The austenite phase in the BM and FZ was identified by means of a Panalytical XRD (X-ray diffractometer) using a Cu-Kα radiation (wavelength of 0.1541 nm) at 40 mA and 45 kV via microdiffraction. The diffraction angle (2Θ), at which the X-rays impinged the sample varied from 30° to 110° with a step size of 0.017° and a pause of 100 seconds at each step. Quantification of the austenite fraction was performed using the direct method, as described in [5]. Vickers microhardness was measured using a Struers DuraScan machine equipped with a motorized x-y stage and a fully automated testing cycle (i.e. stage movement, loading, focusing, and measurement).

Table 2-2 Experimental design for HLAW

Sample #	**Laser power (kW)**	**Welding speed (m/min)**	**WFR (m/min)**	**Voltage (V)**	**Current (I)**
1	4.2	0.5	8	24	194
2	5.2	0.5	8	24	191
3	5.2	0.75	12	28	283
4	5.2	1.0	16	30	352
5	5.2	1.2	19	30	349

For the weld assembled at 1.0 m/min, Vickers microhardness mapping across the entire transverse cross-section was carried out with the ecos WorkflowTM software module using a uniform distribution of test points at a line interval of 0.5 mm (for mapping), a load of 200 g, indentation spacing of 0.2 mm and a dwell time of 15 seconds. Two-dimensional image mapping of the hardness distribution on the surface of this weld was then generated using the area MASTER function in the ecos WorkflowTM software module. Also, to understand the effect of welding speed on the hardness properties, Vickers microhardness profiles were measured under similar test conditions along the mid-thickness from the BM to FZ for each weld. It is noteworthy that the minimum test point separation distance for all measurements was at least three times the diagonal measurement of the indent to avoid contributions from the neighbouring strain fields.

Tensile and Charpy impact tests were performed in accordance with ASME Section IX [6] and VIII [7] standards, respectively. Prior to extracting the tensile and Charpy specimens from the welded plates, the top and bottom surfaces were machined slightly to remove the underfill on the crown and reinforcement at the root, which reduced the joint thickness to 9 mm. The rectangular tensile specimens were then machined from the transverse weld sections to have a gage length of 20 mm, a width of 13 mm and a thickness of 9 mm (Figure 2-1a). These tensile specimens were then tested at room temperature using a 300 kN Tinius Olsen frame. By contrast, the Charpy V-notch impact test specimens, extracted from the weldments at mid-section, were machined with a geometry of 55 mm × 10 mm × 9 mm and a 2-mm deep V-notch in the FZ through the thickness, as depicted in Figure 2-1b. The Charpy impact tests were conducted using a weighted pendulum hammer on a SATEC SI-1C3 system at 255 K (-18°C) based on hydraulic turbine manufacturing requirements, derived from AWS D1.1 specification: “at the LAST, (Lowest Anticipated Service Temperature), or at 0°F (-18°C), whichever is lower”. A Hitachi 3600N SEM (scanning electron microscope) equipped with an EDS (energy-dispersive X-ray spectroscopy) system was used for analysis of the metallographic specimens as well as for fractographic characterization of the fractured tensile and Charpy specimens.

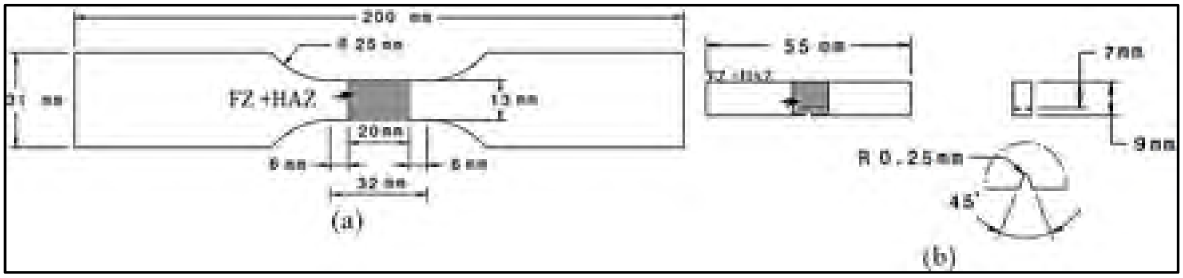

Figure 2-1 Specimen geometries for (a) transverse tensile and (b) Charpy impact tests (the FZ is centered within the demarcated shaded region)

2.3 Results and discussion

2.3.1 Weld bead geometry

Figure 2-2 illustrates the joint cross-sections of two welds assembled at a low welding speed of 0.5 m/min using laser powers of 4.2 kW and 5.2 kW. The formation of periodic drops at the root surface, which is called root humping [8] or sagging [1], shows the instability of the HLAW process at this welding speed. This phenomenon can be attributed to a high heat input, low surface tension and gravity [8], as will be discussed later. With increasing welding speed, fully penetrated welds with good surface characteristics (crown and root) were obtained with HLAW, as shown in Figure 2-3a-c. The FZ area in these welds decreased by ~18% with increasing welding speed from 0.75 m/min to 1.2 m/min and the corresponding weld bead width decreased by ~13%, which can be attributed to a reduction in the heat input. This relatively low heat input process with a high welding speed and associated high productivity is important for manufacturing industries.

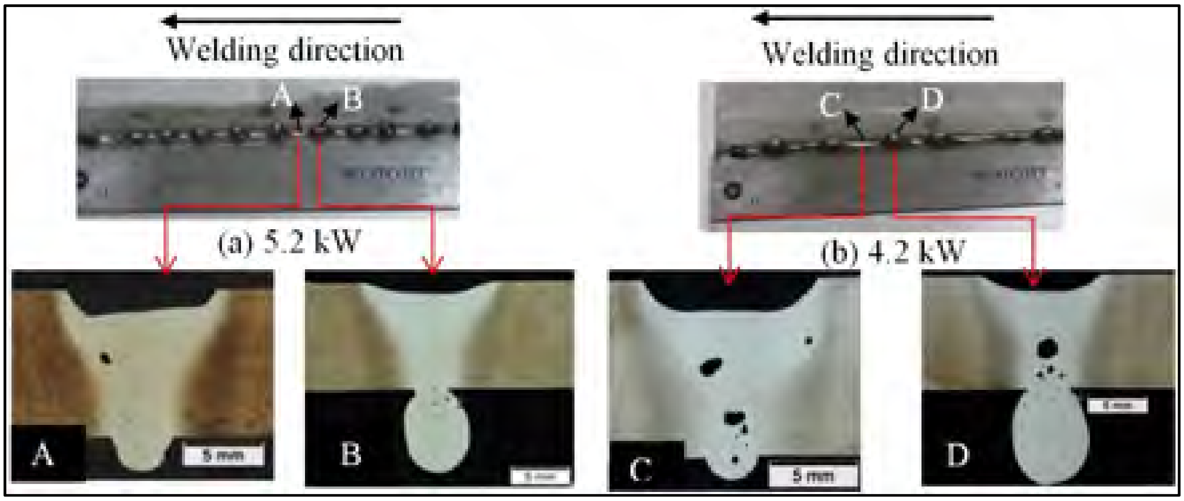

Figure 2-2 Welding defects observed in the transverse cross-sections and root surfaces at a low welding speed of 0.5 m/min and laser powers of (a) 4.2 and (b) 5.2 kW

In order to visualize the contribution of the individual processes (laser and arc) towards the weld bead geometry in the HLAW process, the cross-sections of the laser BOP (bead-on-plate) welds (with no filler wire) and MIG BOP welds (with addition of 410NiMo filler wire) are also illustrated in Figure 2-3d-i. It should be noted that the laser and MIG BOP welds were performed with the same process parameters (see Table 2-2, samples 3, 4 and 5) and set-up conditions as in the HLAW process. The MIG BOP welds exhibited a wide and shallow weld bead with a large reinforcement on the crown surface that formed due to filler metal buildup. On the other hand, the formation of a keyhole led to a narrow and deeply penetrated FZ in the laser BOP welds. For example, at a welding speed of 0.75 m/min, the penetration depth in the laser BOP weld (7.3 mm) is 54 % higher than that for the MIG BOP weld (3.7 mm). In comparison, the FZ of the hybrid laser-arc welds exhibited the good penetration depth and narrow weld bead width characteristics of the laser process and the gap tolerance capacity of GMAW.

2.3.2 Weld defects

The weld imperfections and defects observed in the hybrid laser-arc welds, as shown in the OM images given in Figure 2-2 and Figure 2-3a-c, are mainly underfill, excessive penetration, root humping, and porosity. No cracks were observed in these welds in the as-welded condition.

The root humping or sagging defect in the CA6NM hybrid laser–arc welds was mainly observed in this work for the lowest welding speed (0.5 m/min) condition. Specifically, at both laser power settings (4.2 and 5.2 kW), welding at 0.5 m/min resulted in periodic droplet formation on the root or bottom surface, as illustrated by the transverse sections – cut from two different locations in each weld – that are depicted in Figure 2-2a for a laser power of 5.2 kW (labelled A and B) and Figure 2-2b for a laser power of 4.2 kW (labelled C and D). The cross-sections labelled B and D indicate the presence of the humping defect at 5.2 and 4.2 kW of laser power, respectively, as compared to the cross-sections A and C taken from adjacent areas of the weld where there was no hump. Moreover, despite the lower heat input at 4.2 kW, the root surface quality showed no improvement relative to the weld at 5.2 kW. The formation of root humping in the hybrid laser-arc welds at 0.5 m/min can be attributed to factors such as gravity, reduced surface tension and downward flow of the molten metal at the high heat input [8]. At this lower welding speed, the width of the FZ at the weld root was also noted to increase, making the conditions more critical for gravity drop-out and keyhole collapse. Under these conditions, the pressure induced by the laser and arc was unsustainable by the molten metal. Therefore, vigorous fluid flow triggered the formation of regular droplets (humping) at the root during welding, as shown in Figure 2-2. Another imperfection observed on the root surface of the fully penetrated welds assembled at welding speeds of 0.75 m/min to 1.2 m/min was excessive penetration. Unlike root humping, the weld bead appeared relatively stable in this case. The excessive penetration usually occurred along the entire weld seam and had limited height compared to root humping or sagging.

The excessive penetration height decreased with increasing welding speed, which can be related to a decreasing weld bead width at the root. According to the ISO 12932 specification for HLAW of steels [9], the maximum limit for the excessive penetration height (h) is given by $h \leq (1\ \text{mm} + 1.0\ b)$ or 5 mm, whichever is smaller (where b is the width of the excessive penetration at the root surface of the work piece). In this work, except for the welds assembled at 0.5 m/min that showed serious humping defects, the largest excessive penetration height measured was 2.5 mm at a welding speed of 1.2 m/min. Considering that the measured value for "b" (2 mm) for the welds assembled at welding speeds of 0.75 m/min to 1.2 m/min was nearly constant, the measured excessive penetration height for all the welds was compared against the specified requirement of ~3 mm, as illustrated by the dotted line delineated in Figure 2-4a. This comparison indicated that for the welds manufactured with welding speeds of 0.75 m/min to 1.2 m/min, the excessive penetration height meets the requirements of the ISO 12932 specification [9]. By contrast, the excessive penetration height measured for the welding speed of 0.5 m/min varied periodically and the specified requirements were not met particularly in the area of the humping defect, as illustrated in Figure 2-4a by the error bar for this condition. It is noteworthy that the errors indicated in this work represent two standard deviations of uncertainty, unless specified otherwise. Underfill, an imperfection that appeared as a concave crown on the weld bead top surface of the FZ, can be seen in the transverse cross-sections of the welds illustrated in Figure 2-2 and Figure 2-3. The maximum underfill depth decreased with increasing welding speed (Figure 2-4a).

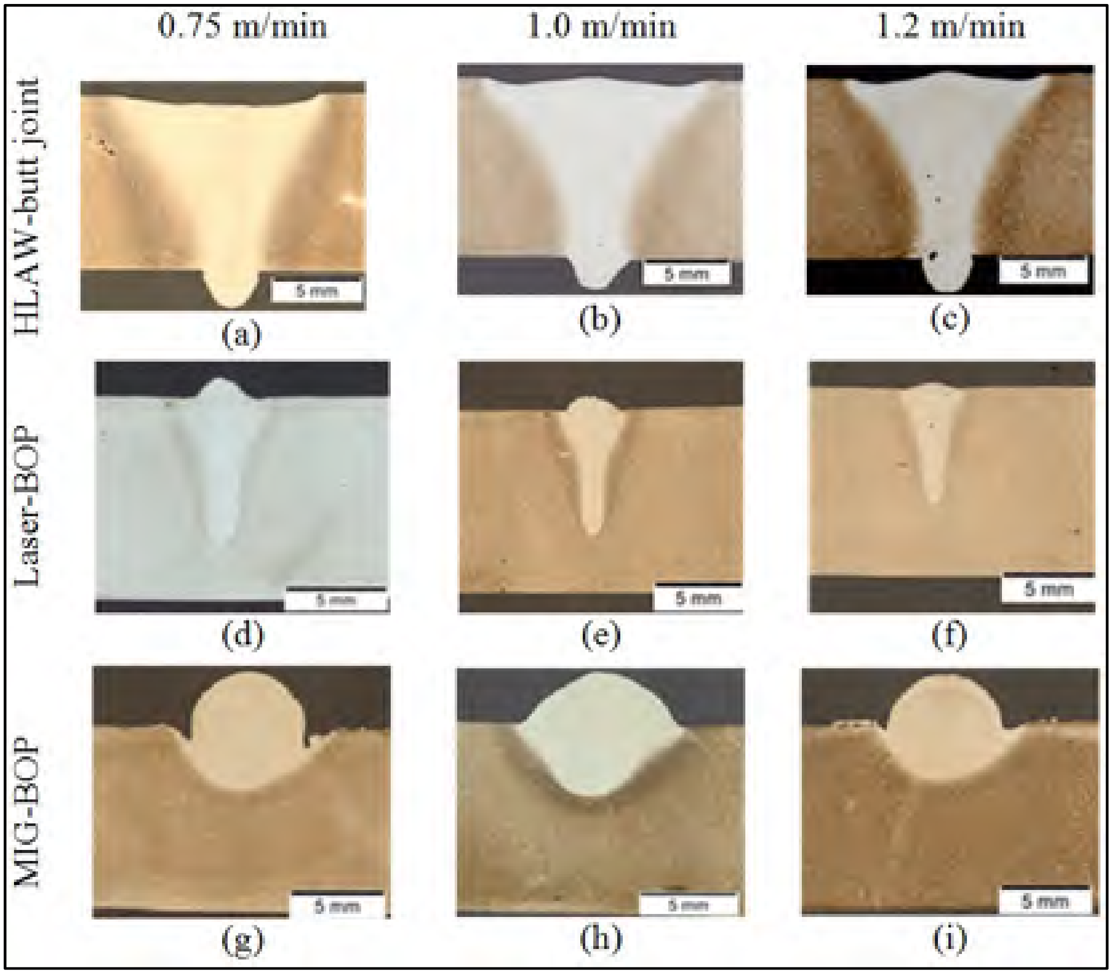

Figure 2-3 Transverse cross-sections of welds manufactured at different welding speeds for the three welding processes: (a, b, c) HLAW, (d, e, f) LW and (g, h, i) MIG

At the lowest welding speed of 0.5 m/min (highest heat input), the underfill depth on the top surface was greatest in the presence of the humping defect on the bottom surface, since severe material loss occurred from the crown due to molten metal flow to the root side.

The lower underfill depth with increasing welding speed can be attributed to less expulsion or evaporation of the molten metal. Therefore, the higher welding speeds (0.75-1.2 m/min) in this work suitably minimized the underfill defect, though its elimination was unattainable due to the fast solidification conditions after HLAW that prevented the possibility of refilling by the molten metal [10].

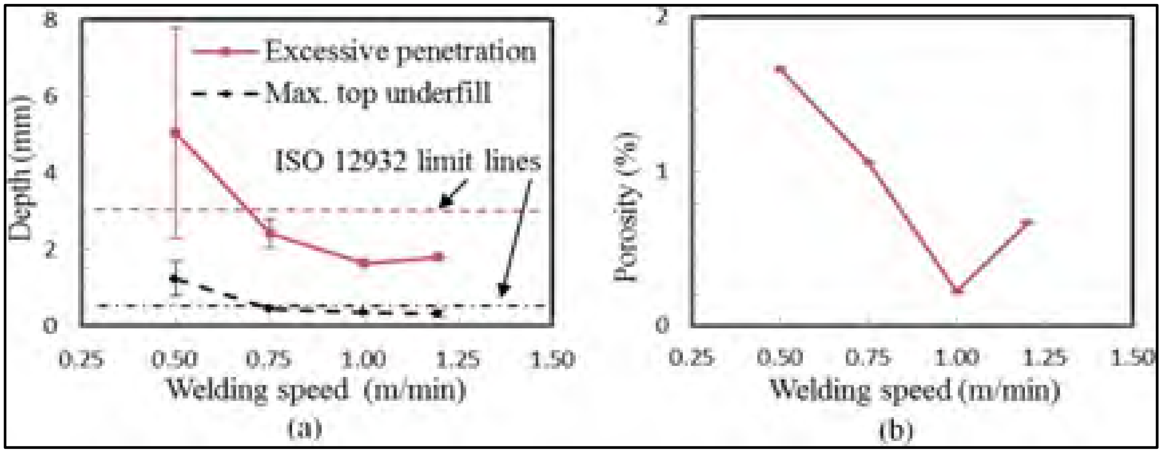

Figure 2-4 Weld defects: (a) excessive penetration and underfill depth, and (b) total porosity (Note: root humping height is taken as excessive penetration at a welding speed of 0.5 m/min)

Considering the highest requirement on a finished weld in ISO 12932 [9], i.e. quality level B, the acceptance criterion for the maximum underfill depth (d) is given by $d \leq 0.05 \times$ thickness or 0.5 mm maximum. As the thickness was 10 mm for the CA6NM plates, the acceptance criterion for the maximum underfill depth is 0.5 mm for the hybrid laser-arc welds to meet quality level B requirements. In Figure 2-4a, the maximum underfill depth according to the acceptance criterion of ISO 12932 [9] is delineated by the dotted line and the measured values indicate that for welding speed conditions between 0.75 m/min and 1.2 m/min, the hybrid laser-arc welds in CA6NM satisfy the Class B requirements.

Porosity appeared mainly in the lower half of the FZ, but was also distributed randomly at other locations in the FZ, probably due to the convective flow of the molten metal. Figure 2-4b shows the total porosity (expressed as a percentage of the FZ area) in the welds manufactured at the different welding speeds. At 0.5 m/min, the total porosity in the FZ was the highest (~1.7%). For welding speeds above 0.5 m/min, the total porosity was lower than ~1%. These pores in the FZ were spherical and/or irregularly shaped, as shown in Figure 2-2 and Figure 2-3. Excluding measurements from the 0.5 m/min welding speed condition, the average diameter of the spherical porosities measured from all the other welds was ~400 µm, but pores as fine as ~50 µm in diameter could also be observed under the OM. These pores are most likely gas porosity, which can be due to the entrapment of air or shielding gas inside the FZ or the precipitation of hydrogen in the molten pool at the solid/liquid interface during solidification [11]. The considerably larger size of the pores observed in the FZ of the weld assembled at a welding speed of 0.5 m/min is probably mainly due to the collapse of the unstable keyhole with possibly some secondary influence from the growth of the gas porosity. The stability of the keyhole depends on the balance between the forces that tend to close (surface tension and gravity) and open (vapor pressure) the keyhole. When the vapor pressure cannot withstand the increased molten metal volume, the keyhole becomes unstable, tends to collapse and entrap metal vapor, shielding gases, or even air, leading to the formation of porosity [12]. For example, Seto et al. remarked that the porosity formed during laser welding of stainless steels contains metal vapor and inert shielding gas [13], or Abbott et al. found that oxygen can be entrapped in the form of carbon monoxide in laser or hybrid laser-arc welded mild steel [14].

2.3.3 Microstructures

The general macrostructure from the FZ to the HAZs and BM of the weld manufactured at a welding speed of 1.0 m/min is displayed in Figure 2-5. For the hybrid laser-arc welds, the different HAZs, as distinguished under an OM, were correlated in the present work to the ternary Fe-Cr-Ni equilibrium phase diagram at 13% Cr and 4% Ni [15] in a similar manner to that defined by Carrouge [16] and Enerhaug and Steinsmo [17] for welded low carbon supermartensitic stainless steels, as well as Thibault et al. [18] and Sarafan et al. [19] for welded low carbon martensitic stainless steels. However, it is noteworthy that a phase diagram can only typify the different phase constituents possible in the alloy at equilibrium, but the extent of these phase transformations in the different regions of the weld are influenced by the non-equilibrium conditions during welding (fast heating and cooling rates) as well as the differences in chemistry.

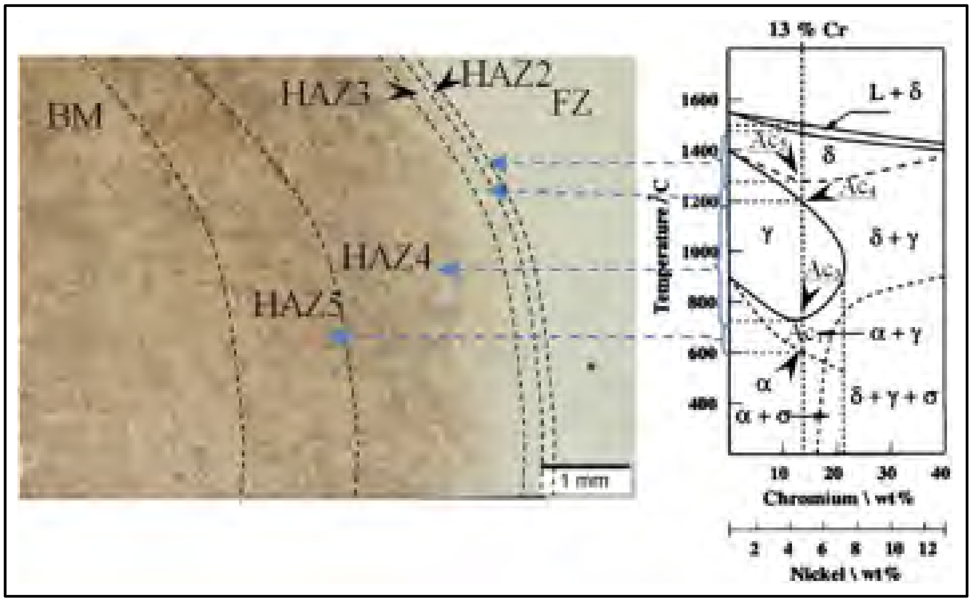

Figure 2-5 Macrostructure from the FZ to the BM (at 1.0 m/min welding speed) according to the equilibrium Fe-Cr-Ni phase diagram [15]

2.3.3.1 Base metal

The as-received microstructure of the low carbon 13%Cr-4%Ni CA6NM martensitic stainless steel BM is composed of mainly tempered lath martensite and plates of primary delta ferrite, as shown in Figure 2-6a. This lath martensite consists of several packets within which parallel blocks of narrow ruler shaped laths are formed [20]. EDS analysis of regions "A" and "B", as depicted in the BM microstructure given in Figure 2-6a, revealed lower chromium and more nickel in the former region (Figure 2-6b), as compared to the latter (Figure 2-6c). This indicates that the particle of region "B" is delta ferrite (δ), while the matrix of region "A" is martensite (α'). Delta ferrite, the high temperature phase in the equilibrium phase diagram given in Figure 2-5, can be retained in the room temperature microstructure through non-equilibrium cooling. The primary delta ferrite fraction in the BM microstructure was measured to be 6.5 ± 2%. It is noteworthy that the large primary delta ferrite is distinguished from the delta ferrite stringers formed in the FZ and HAZ on cooling after welding (as discussed below) to highlight the existence of the former in the BM from the casting process. In addition, according to literature, certain fractions of retained austenite and small amounts of chromium carbide precipitates can also be present [15]. The retained austenite fraction, estimated to be 9.6% in the as-received BM, was quantifiable through XRD, as illustrated by the spectrum in Figure 2-6d that consisted of four martensite and two austenite peaks. However, the chromium carbides could not be detected in the XRD spectrum, probably due to their fine size and low volume fraction.

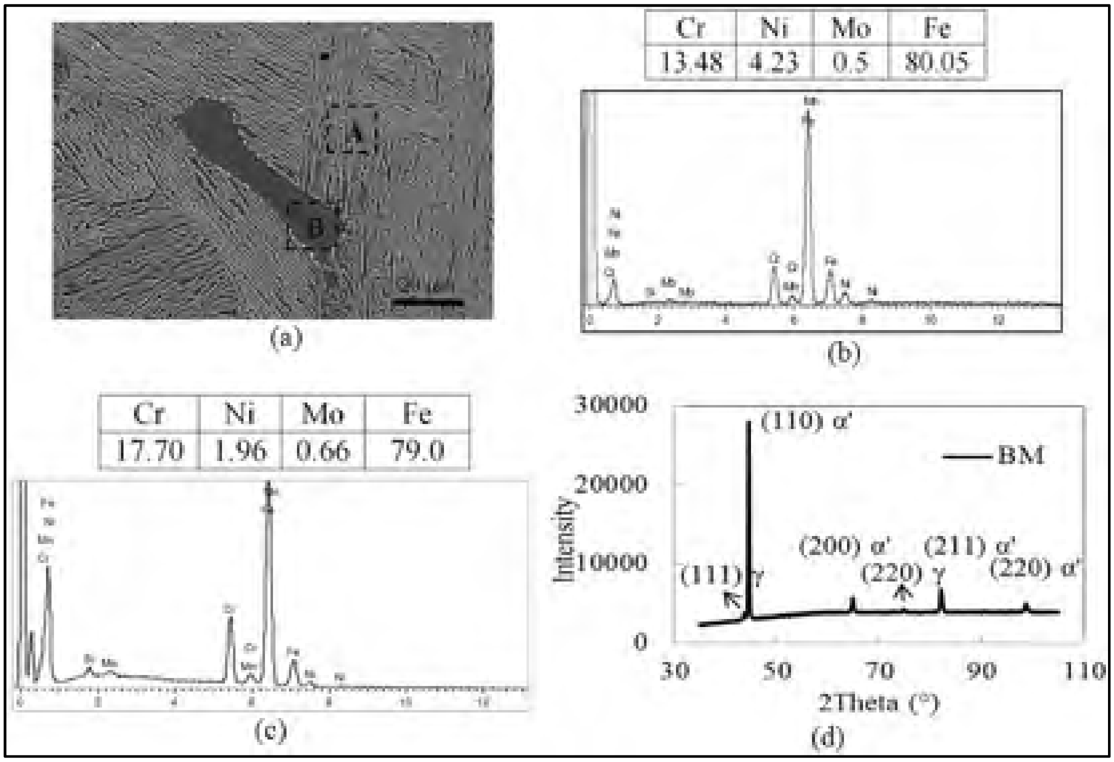

Cr	Ni	Mo	Fe
13.48	4.23	0.5	80.05

Cr	Ni	Mo	Fe
17.70	1.96	0.66	79.0

Figure 2-6 SEM image of the BM showing regions A and B that were analyzed using EDS; (b) EDS results for region A indicating it as the martensite matrix; (c) EDS results for region B indicating it as delta ferrite; and (d) XRD spectrum for the BM

2.3.3.2 Fusion zone

Figure 2-7a displays the macroscopic feature in the transverse section of the FZ under an OM and also defines regions "A" and "B" that were observed at higher resolution, as illustrated in Figure 2-7b-c.

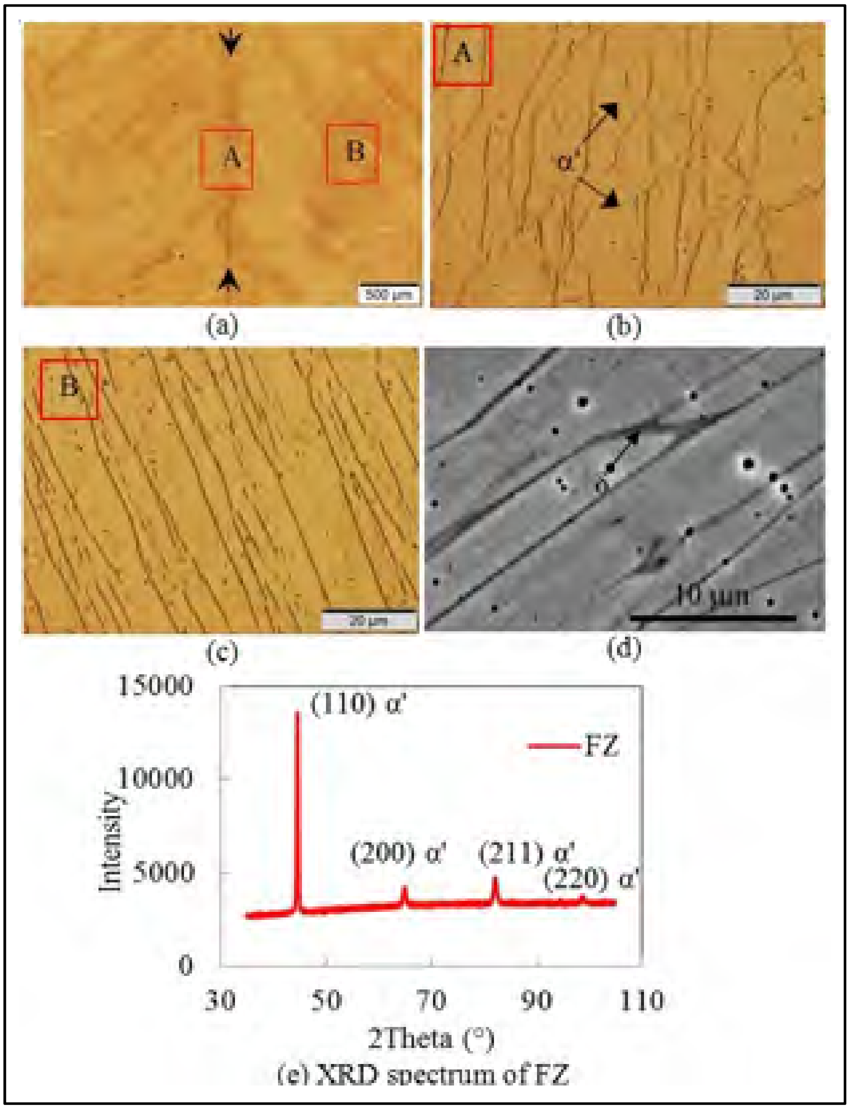
A
B
500 µm
A
α'
20 µm
B
20 µm
δ
10 µm
15000
10000
5000
0
Intensity
(110) α'
FZ
(200) α'
(211) α'
(220) α'
30
50
70
90
110
2Theta (°)

(a) (b) (c) (d) (e) XRD spectrum of FZ

Figure 2-7 FZ characteristics of the weld manufactured at a welding speed of 1.0 m/min. (a) OM image of the FZ macrostructure, (b) OM image of FZ along the weld centerline in region A, (c) FZ microstructure in region B, and (d) SEM micrograph of the FZ microstructre showing fine stringers of delta ferrite

From these observations, it is evident that the FZ consists of a columnar dendritic structure in which the matrix is lath martensite and some residual delta ferrite (dark etched) is present at the prior-austenite grain boundaries (Figure 2-7d). Also, it is interesting that Figure 7(d) shows some porosity appearing in the martensitic matrix. These very regular spherical pores with a small diameter in the range of approximately 0.1-0.5 μm were different from the typical porosity caused by gas precipitation, bubble entrainment, or collapse of unstable keyholes, as discussed above. The mechanism of their formation is unclear at the moment but these small pores might be due to the heavy etching during sample preparation.

On cooling after welding, the molten metal that comprised the FZ solidified first to delta ferrite, which then underwent solid state transformation to austenite (γ). In particular, this transformation (δ→ γ) would start from the boundaries of columnar delta ferrite grains; the new austenite grains would then form by "consuming" the delta ferrite gradually. Hence the residual delta ferrite remaining at the prior-austenite grain boundaries in the microstructure is due to the incomplete solid state phase transformation (δ→ γ), which is mainly controlled by the diffusion of alloying elements that is limited due to the high cooling rates experienced in welding. Subsequently, on further cooling to room temperature the austenite phase would then transform to martensite through another solid state phase transformation (γ→ α'). Owing to the fast cooling conditions after HLAW, austenite can also be retained, though its detection is often limited by its relatively small size and/or small fraction. The delta ferrite fraction in the FZ of the hybrid laser-arc welds was measured to be 3.8 ± 1.0%, which is comparable with the value of 4.7% reported for electron beam welding of CA6NM [19]. From observations at higher magnification (Figure 2-8), the very fine residual delta ferrite (~5 μm in width), which appeared as discontinuous stringers, was distinguished with the SEM-EDS elemental maps for chromium and nickel in the FZ Specifically, the delta ferrite should be enriched with ferrite-stabilizing elements (e.g. chromium and molybdenum) but depleted in austenite-stabilizing elements (e.g. nickel) relative to the martensitic matrix; the chromium enrichment and nickel depletion observed in Figure 2-8 for the discontinuous stringers then lends confidence to their identification as delta ferrite. For quantification of the retained austenite fraction in the FZ of the hybrid laser-arc welds, XRD was performed (Figure 2-7e) but noticeable peaks in the spectrum were not distinguishable, probably because the relative amount of austenite was lower than the detection limit of 2%.

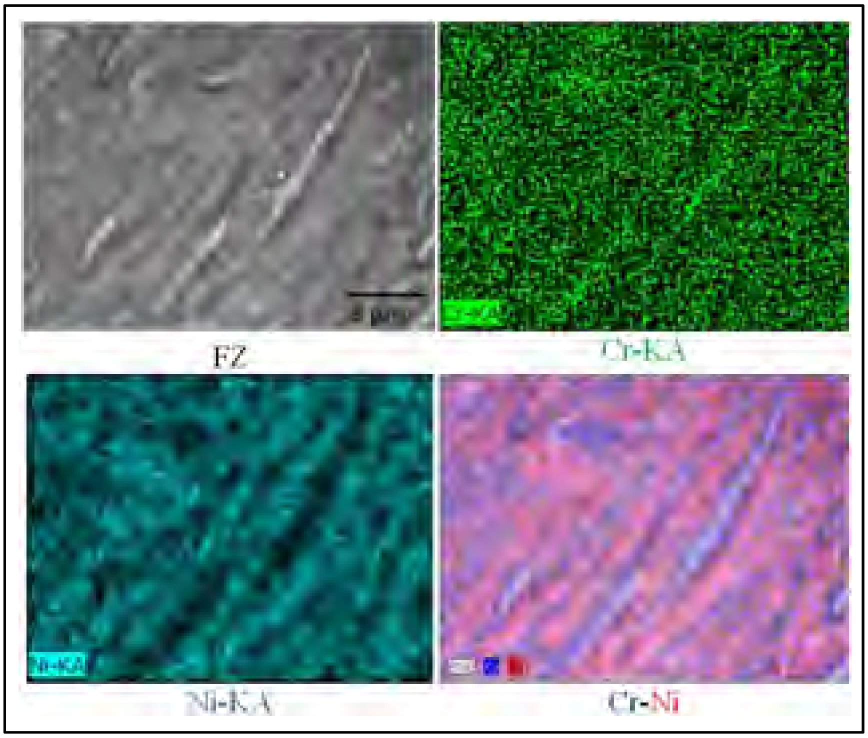

Figure 2-8 SEM-EDS mapping of the elemental distribution in the FZ microstructure corroborating the presence of delta ferrite between the martensitic laths

2.3.3.3 Heat-affected zones

In accordance with other weldability studies on low carbon martensitic stainless steels [16-18], the HAZ of the single pass hybrid laser-arc welds in CA6NM could also be subdivided into five different zones that concurred with the Fe-Cr-Ni ternary phase diagram, though only HAZ2, 3, 4 and 5 were discernable (Figure 2-5). It is worth mentioning that the phase constituents in the microstructure and the width of each region strongly depend on the local chemical composition, the peak temperature reached, and the heating and cooling rates [15].

The first HAZ (HAZ1), corresponding to the partially melted zone (L + δ), is located adjacent to the FZ. However, it was difficult to distinguish HAZ1 from the FZ in terms of the microstructural changes. In this region, the microstructure undergoes rapid heating and cooling that beget multiple transformations and lead to a final microstructure similar to the

FZ at room temperature. Difficulty in identifying this region in welded low carbon martensitic stainless steels has also been reported for electron beam [19] and arc [18, 16] welding processes.

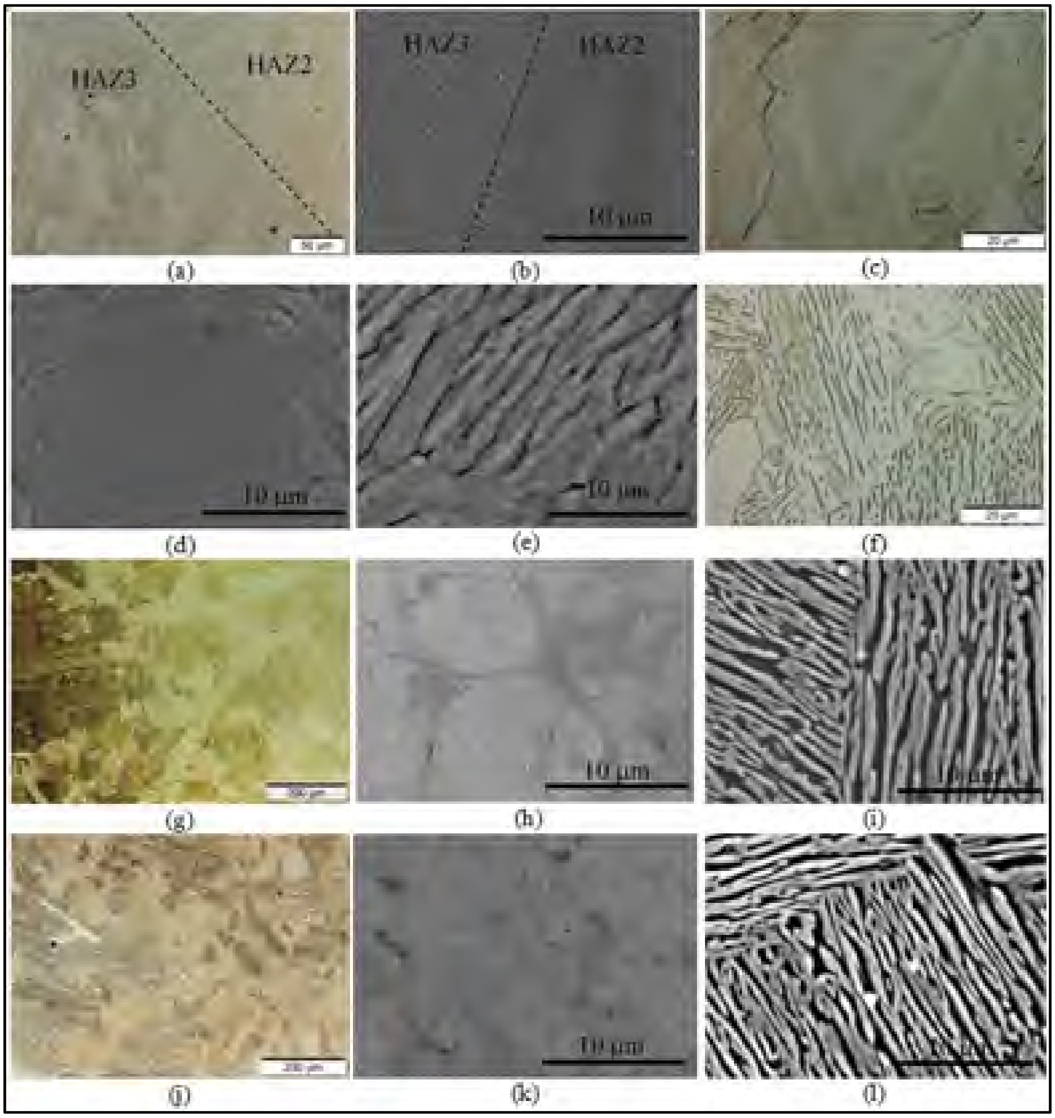
HAZ3
HAZ2
(a)
HAZ3
HAZ2
10 µm
(b)
(c)
10 µm
(d)
10 µm
(e)
(f)
(g)
10 µm
(h)
(i)
(j)
10 µm
(k)
(l)

Figure 2-9 Microstructural evolution in the various HAZs in the weld manufactured at a welding speed of 1.0 m/min. (a-b) HAZ2/3 interface, (c-d) HAZ2, (e-f) HAZ3, (g-i) HAZ4, (j-l) HAZ5

HAZ2, also called the single phase delta ferrite region, can be seen in the OM and SEM images presented in Figure 2-9a-d. This region represents a part of the BM that was heated above the Ac_5 temperature and under the solidus temperature during the weld thermal cycle. In HAZ2, the tempered lath martensite in the as-received BM transforms sequentially on heating during welding to austenite and then delta ferrite; on cooling to room temperature after welding, the delta ferrite transforms to austenite that in turn reverts to lath martensite, which is now untempered. Owing to the high peak temperatures experienced in HAZ2, substantial growth of the delta ferrite grains also occurs on heating during welding. Upon cooling to room temperature after welding, transformation of the high temperature phases (delta ferrite and austenite) occurs, but the coarsened grain structure remains a characteristic feature of the untempered lath martensitic microstructure in HAZ2 (Figure 2-9a-b). Hence, HAZ2 is also referred to as the coarse-grained region. Within the predominantly untempered lath martensite microstructure of HAZ2, some stringers of delta ferrite are also present. The retention of the high temperature delta ferrite phase in the room temperature microstructure of HAZ2 can be attributed to the incomplete solid state phase transformation ($\delta \rightarrow \gamma$), owing to the limited diffusion of substitutional alloying elements (such as chromium and molybdenum) into the austenite at the high weld cooling rates [21]. By contrast, in HAZ3, referred to as the high temperature dual phase ($\delta + \gamma$) region, the microstructure shown in Figure 2-9e-f is finer than HAZ2. In particular, HAZ3 represents the part of the BM that is heated during welding to temperatures between the Ac_4 and Ac_5, which transforms the tempered lath martensite microstructure of BM to austenite and partially to delta ferrite.

The lower temperatures and possibly the pinning effect of delta ferrite at the austenite grain boundaries limits grain growth in HAZ3. On cooling after welding, the high temperature phases (delta ferrite and austenite) in HAZ3 eventually revert to martensite, which again is untempered. As in HAZ2, some delta ferrite can be retained in the room temperature microstructure of HAZ3 due to incomplete solid state transformation from delta ferrite to austenite. Figure 2-9g-i represent the room temperature microstructure observed in HAZ4, which is also referred to as the single phase austenite region, as it represents the part of the BM that is rapidly heated during welding to temperatures between Ac_3 and Ac_4, the fully austenitic region of the phase diagram. Specifically, once the temperature reaches Ac_3 during the heating cycle, the tempered lath martensite structure of the BM transforms to austenite. At high heating rates, as usually experienced during welding, this transformation is controlled by a diffusionless shear mechanism [22]. By increasing the temperature from Ac_3 to Ac_4, the austenite grains grow, leading to a reduction in the M_s and hence increasing the hardenability [23]. Also, with increasing temperature from Ac_3 to Ac_4, the dissolution of chromium carbides, e.g. $M_{23}C_6$, during heating can occur [15, 18]. Since the full dissolution of chromium carbides in the austenitic phase is a time-temperature dependent process [15], the extent to which these carbides dissolve in HAZ4 is a function of the local composition, peak temperature, and heating rate. On cooling after welding, the austenite transforms and untempered lath martensite is the predominate phase in the final microstructure at room temperature, as presented in Figure 2-9g-i, but some undissolved or partially dissolved carbides may still be present in HAZ4 owing to the short time period and high heating rate experienced. It is noteworthy that carbide dissolution is mostly limited by the diffusion of substitutional elements, e.g. chromium, in the austenite. The process of carbide dissolution at first starts with the diffusion of interstitial elements, namely carbon into the matrix, as carbon has a higher diffusion rate than that of chromium [24]. The dissolution temperature of carbides in martensitic stainless steels significantly depends on the heating rate [25] and the temperature for the complete dissolution of chromium carbides in austenite increases as the heating rate rises. However, to the authors' knowledge, neither the dissolution temperature of the carbides nor the influence of the heating rate on the dissolution temperature has ever been reported for CA6NM. Previously, for a 13%Cr-4%Ni martensitic stainless steel composition, knowing the carbide dissolution with temperature, Thibault et al. [18] sub-categorised HAZ4 into three different areas in flux core arc welds: (1) at a higher temperature closer to Ac_4, both grain growth and carbide dissolution were considered; (2) at a lower temperature closer to Ac_3, carbide dissolution was reasoned to be insignificant; and (3) at an in-between temperature, partial carbide dissolution was inferred.

Termed as the low temperature dual phase region ($\alpha' + \gamma$), HAZ5 lies closest to the BM and corresponds to the region of the BM that has been heated to temperatures between Ac_1 and Ac_3 in the phase diagram. Here, the tempered martensite microstructure of the BM partially transforms to austenite on heating during welding. Upon cooling after welding, the austenite can either retransform to martensite (untempered martensite) or remain stable in the final microstructure (so-called reversed austenite). Thus, the final room temperature microstructure in the HAZ5 (Figure 2-9j-l) may consist of both tempered and untempered martensite, as well as some reversed austenite. EDS elemental mapping in HAZ5, as shown in Figure 2-10, revealed a strong accumulation of nickel (austenite stabilizer). The high magnification images also revealed chromium depletion between the lath martensite, which denotes the presence of austenite in this area. Thus, in the region of the BM where the peak temperatures experienced were near Ac_1, some reversed austenite can especially remain stable in the microstructure on cooling, which may lead to further softening, as will be discussed later.

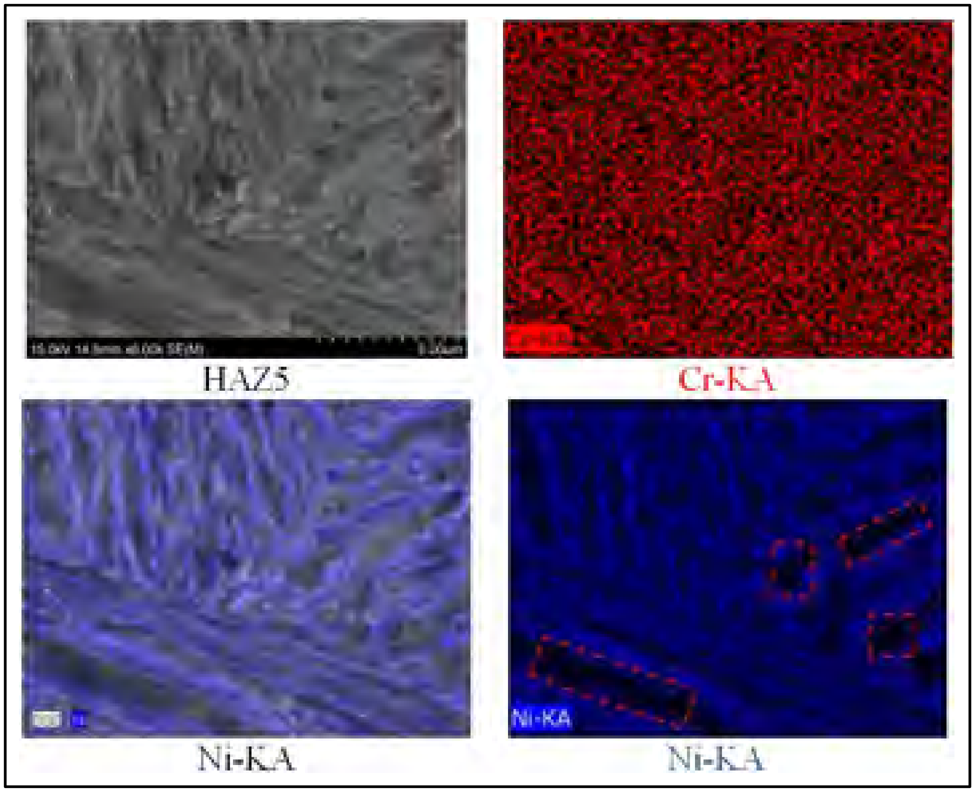

Figure 2-10 SEM-EDS mapping of the elemental distribution in HAZ5

By contrast, for the BM, at a temperature well above Ac_1, near Ac_3, the austenite formed on heating may be more unstable, which leads to complete or partial transformation of austenite to untempered martensite during cooling. According to a previous report [26], austenite becomes unstable mainly when the concentration of austenite-stabilizing elements, such as nickel, decreases. This occurs as the temperature increases due to the increasing diffusivity of nickel and the growth of austenite grains. This can also lead to an increase in the MS temperature and consequently contribute to the transformation of austenite to untempered martensite [26]. Reheating in the HAZ5 temperature range can also cause chromium carbides to precipitate, resulting in lower carbon content and softened martensite [27].

2.3.4 Mechanical properties

2.3.4.1 Microindentation hardness

The microindentation hardness evolution across the FZ, HAZs and BM was measured along the transverse cross-section of the welds assembled at different welding speeds (Figure 2-11a-e). The average measured hardness of the CA6NM BM was 297 ± 5 HV, which corroborates with the values reported for similar martensitic stainless steels [18-19]. The average hardness of the FZ in the welds assembled at different welding speeds ranged from 345 ± 8 HV at 0.5 m/min to 355 ± 11 HV at 1.2 m/min, as given in Figure 2-11f. These results indicate that the average hardness in the entire FZ increases ever-so-slightly and almost linearly as the welding speed increases from 0.5 m/min to 1.2 m/min. In particular, the heat input decreases and the cooling rate increases with increasing welding speed, such that the room temperature structure of the martensite matrix may undergo refinement and increased carbon saturation [27]. Nonetheless, the FZ hardness of 354 HV for the hybrid laser-arc weld assembled in this study at a welding speed of 1.2 m/min is lower than the mean hardness values of 365 HV and 362 HV reported for FCAW of a similar CA6NM material [28] and 415 stainless steel [18], respectively. The FZ hardness values in the hybrid laser-arc welds are also particularly low compared to reported values of 390 HV-408 HV for CA6NM electron beam welds [19]. This difference in the FZ hardness between these two high energy beam processes may be due to the addition of a lower carbon content (relative to the BM) filler metal in HLAW that leads to the formation of softer martensite in the FZ relative to that in the autogenous electron beam welds.

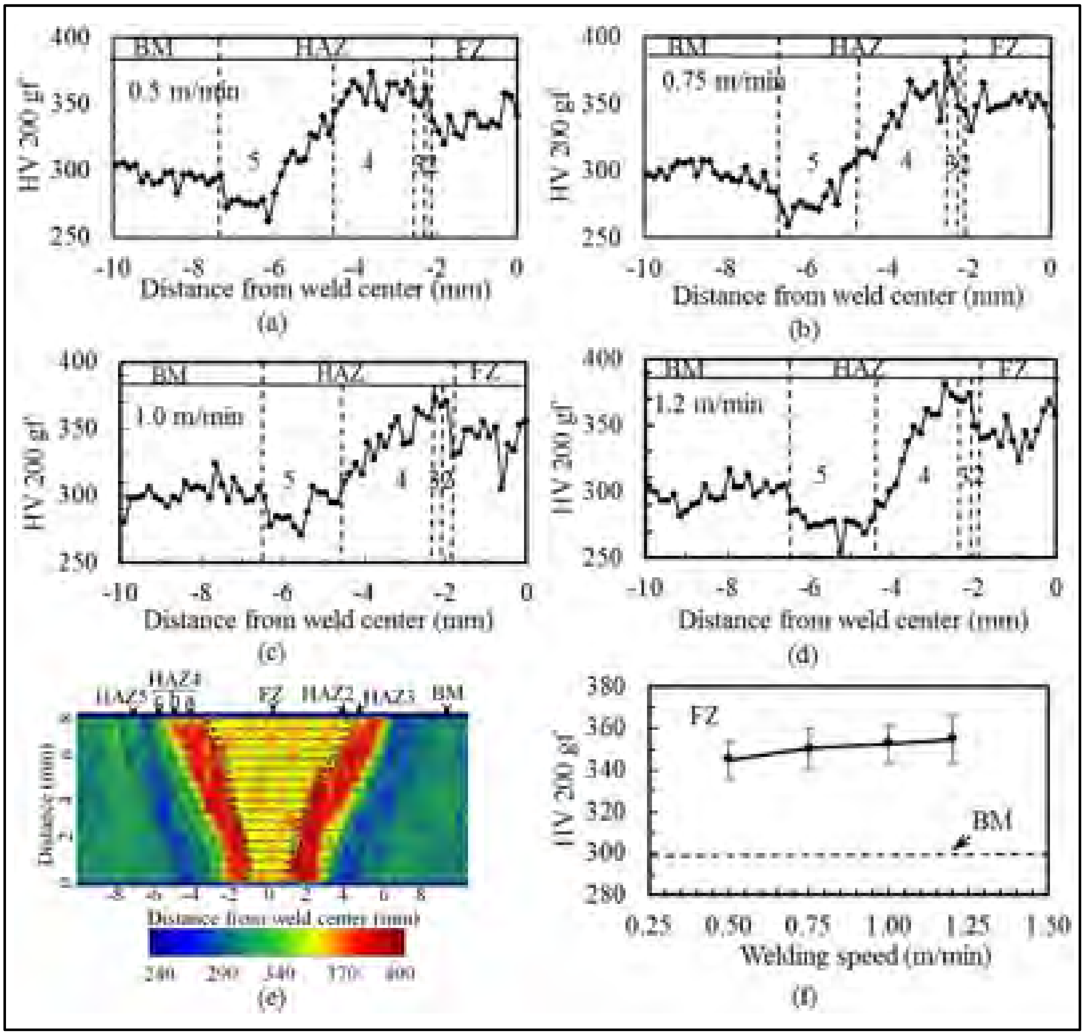

Figure 2-11(a-d) Hardness profiles at different welding speeds, (e) 2D hardness map for 1.0 m/min welding condition and (f) dependency of FZ hardness on welding speed

Significant differences in the hardness of the different HAZs were observed, but their variation with different welding speeds was not noticeable. However, the width of the HAZ varied with welding speed from ~5.3 mm at 0.5 m/min to ~4.7 mm at 1.2 m/min. The slight decrease in HAZ width at a higher welding speed is due to the slight decrease in heat input. The amount of heat input can affect the width of the HAZ, since this heat spreads from the FZ to the BM through the HAZ [29]. The 2D hardness contour map (Figure 2-11e) displays a "color" representation of the hardness variances across the weld from the BM to the FZ for the welding speed condition of 1.0 m/min. Different regions of the FZ, HAZs and BM can be distinguished based on the accompanying scale of the hardness values. Specifically, the microhardness increases from the fusion boundary to an average value of 340 ± 5 HV in HAZ2 (high temperature single phase δ region), 350 ±10 HV in HAZ3 (high temperature dual phase $\delta+\gamma$ region), and reaches the maximum single value of 380 HV in HAZ4 near the HAZ3/HAZ4 boundary. HAZ4 can be sub-divided into three different areas according to the hardness variations, as observed in the 2D microhardness map (Figure 2-11e). The maximum hardness in HAZ4a, as distinguished by the "red" colour in the 2D hardness map (Figure 2-11e), corresponds to the single phase austenitic region with peak temperatures close to Ac_4. During the heating cycle, the tempered martensite in the BM transforms to austenite in this region and the chromium carbides, already existing in the BM, mostly in the form of $M_{23}C_6$ [30], can fully dissolve. This can raise the carbon content in the austenite so that the untempered martensite formed from this austenite will be harder. As the peak temperature in HAZ4 decreases, the maximum hardness also decreases (going from HAZ4/HAZ3 to HAZ5/HAZ4) in Figure 2-11e. As clearly evident in the 2D hardness map, the second part of the single phase austenite region (HAZ4b) that was demarcated "yellow" in color has a lower average hardness of 350 ± 6 HV compared to HAZ4a (368 ± 10 HV). This may be attributed to the partial dissolution of the carbides at the lower temperatures in a single phase austenitic region of HAZ4b compared to HAZ4a. The third region of HAZ4 (HAZ4c), referred to as the area close to HAZ4/HAZ5 boundary, naturally experiences a lower austenitizing temperature compared to HAZ4b. In the 2D microhardness map, HAZ4c is identifiable as the "green" coloured region that corresponds to an average microhardness of 337 ± 7 HV. Relative to the other regions of HAZ4, the lowest hardness in HAZ4c is due to the lowest peak temperatures experienced locally and the associated lack of significant carbide dissolution. This subdivision (HAZ4a-c) according to the hardness variation is in good agreement with previous reported work on a similar material welded using FCAW [18]. HAZ5 tends to be significantly softer compared to HAZ4 and the BM; a minimum microhardness value of 270 ± 5 was evident in HAZ5. The lowest hardness value observed in HAZ5 may be attributed to partial transformation of martensite to austenite on heating and its possible retention on cooling to room temperature during the welding thermal cycle; this reversed austenite (being softer than martensite) would then reduce the hardness. In addition, the HAZ5 thermal cycle is compatible with the chromium carbide coarsening temperature [27]. The carbon content of martensite in this region can thus decrease due to carbide coarsening, leading to matrix softening compared to the BM. This softening behaviour in HAZ5 of the CA6NM hybrid laser-arc welds was also observed in the welds manufactured using FCAW [18]. It is noteworthy that the extent of this softening depends on the temper conditions applied to the BM and the weld thermal cycle. By contrast, the austenite that forms during heating in HAZ5, especially near the HAZ5/HAZ4 boundary, can also transform on cooling to martensite, which is untempered. Hence, with the co-existence of tempered and untempered martensite, an increase in hardness in this part of the HAZ5 near the HAZ5/HAZ4 boundary can occur. The co-existence of both tempered and untempered martensite in HAZ5 was also reported for flux core arc [18] and electron beam [19] welds of similar materials.

2.3.4.2 Tensile properties

Considering the lack of integral features in the welds assembled at a welding speed of 0.5 m/min, mechanical property testing (tensile and Charpy) was thus only conducted on the high integrity welds obtained at welding speeds of 0.75 m/min to 1.2 m/min.

Table 2-3 Ultimate tensile strength and impact energy obtained at different welding speeds

As-welded	Ultimate tensile strength (MPa)	Impact energy (J)
Specification	≥ 755[a]	≥27[b], ≥ 35[c]
0.75 m/min	948	20.5
1.0 m/min	959	21.0
1.2 m/min	941.5	28.5

[a] ASTM A 743 standard in annealed and tempered condition;
[b] ASME Sect. VIII Div.1;
[c] ALSTOM industrial specification

As given in Table 2-3, the measured ultimate tensile strength values (calculated from two tests using transverse tensile test specimens) were similar for the welds assembled at conditions of 0.75 m/min to 1.2 m/min. From these values an average ultimate tensile strength of 949 ± 7 MPa was calculated for the CA6NM hybrid laser-arc welds. Considering that the minimum ultimate tensile strength requirement in ASTM A743 standard is 755 MPa for CA6NM in the annealed and tempered condition [31], the hybrid laser-arc welds in the as-welded condition met quite sufficiently the specification.

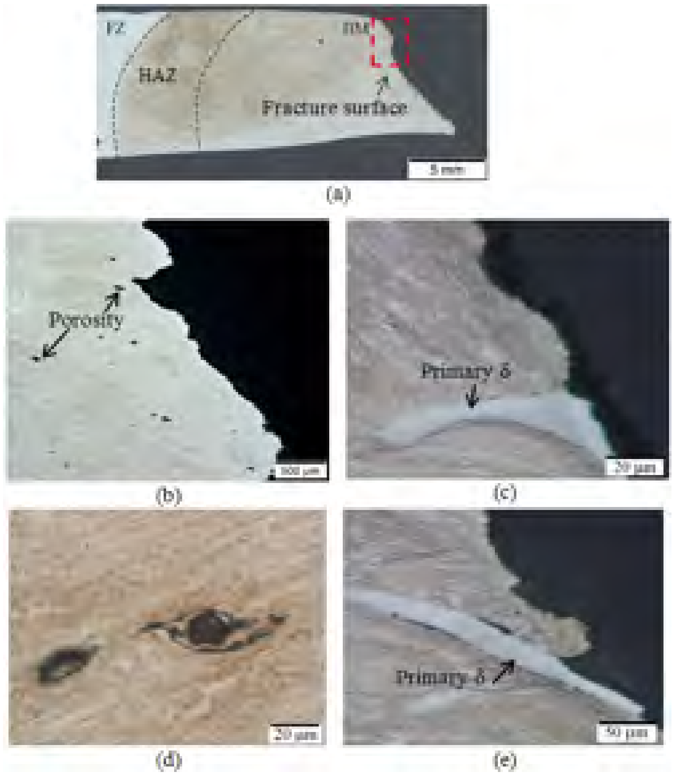

Figure 2-12 Microstructure near the tensile fracture surface of the weld assembled at a welding speed of 1.0 m/min with failure occurring exclusively in the BM

Moreover, the ultimate tensile strength values obtained in this present study lie within the reported range of 796 MPa and 1018 MPa that varies depending on the carbon content and tempering temperature for CA6NM in the normalized and tempered condition [32].

Specifically, for the weld assembled at a welding speed of 1.0 m/min, observation of the transverse cross-section of the fractured tensile specimen (Figure 2-12) revealed the presence of small voids elongated near the fracture location along the tensile loading direction. The amount of voids was measured to be 0.60%, which is significantly higher than the porosity in the original BM (0.15%). The higher percentage of the voids close to the tensile fracture surface can be due to a combination of (1) growth of pre-existing porosity in the cast structure of the BM and (2) the formation of new voids during tensile loading.

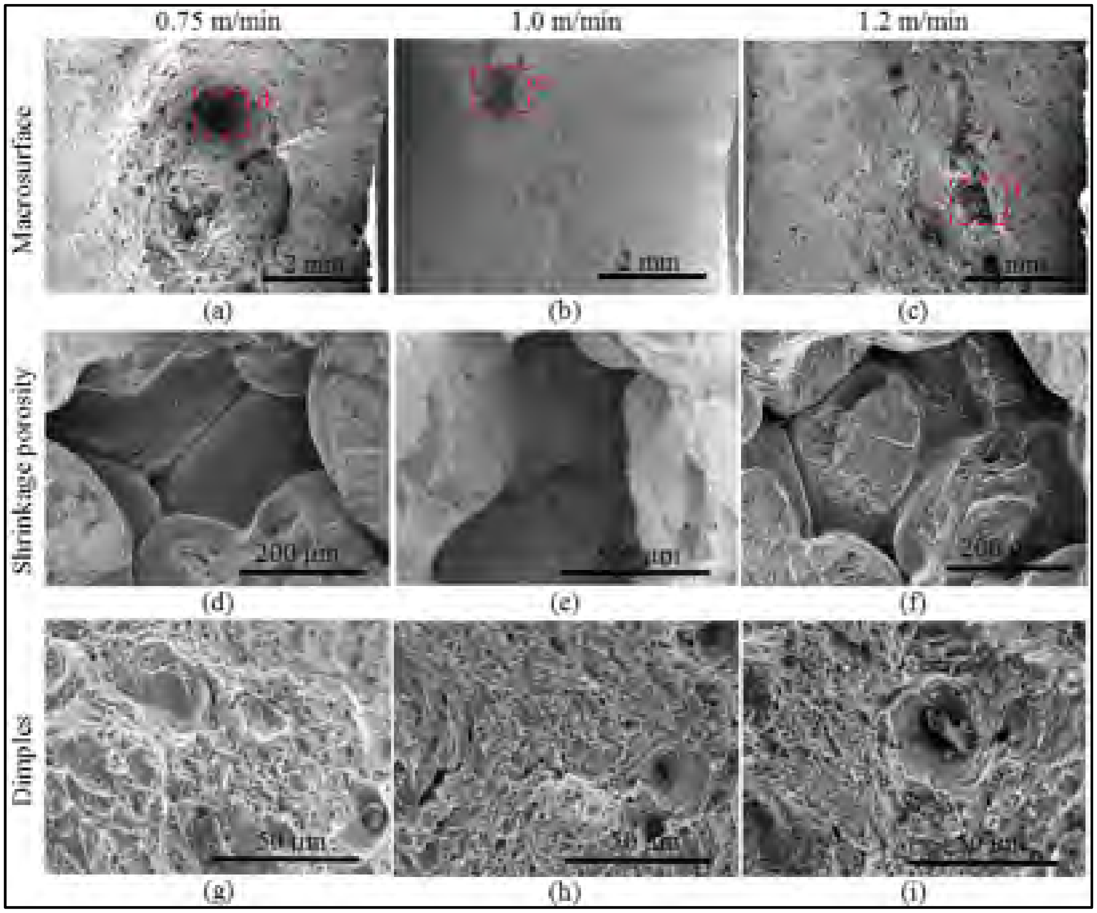
0.75 m/min
1.0 m/min
1.2 m/min
Macrosurface
Shrinkage porosity
Dimples
d
e
f
2 mm
2 mm
2 mm
(a)
(b)
(c)
200 μm
200
(d)
(e)
(f)
50 μm
50 μm
50 μm
(g)
(h)
(i)

Figure 2-13 Tensile fracture surfaces of the welds assembled at different welding speeds

For instance, typical pre-existing gas and shrinkage porosity in the BM from the casting process are visible in the HAZ of the weld assembled at 0.75 m/min (Figure 2-13a).

Moreover, shrinkage porosity with an average length of ~1 mm was also observed on the tensile fracture surfaces, as illustrated in Figure 2-13d-f. The presence of such gas and shrinkage porosity defects in the BM can further induce premature failure in the BM rather than in the weldment. In particular, despite a 10% reduction in hardness in HAZ5 relative to the BM, strain localization and failure remained confined exclusively to the BM. This indicates that the casting defects in the CA6NM microstructure had a predominant influence on the failure characteristics due to the local reduction in the load-bearing cross-sectional area in the BM. It is noteworthy that the high integrity of the weldment and the local strengthening in the FZ and HAZ2-4 also limited strain accumulation in these areas.

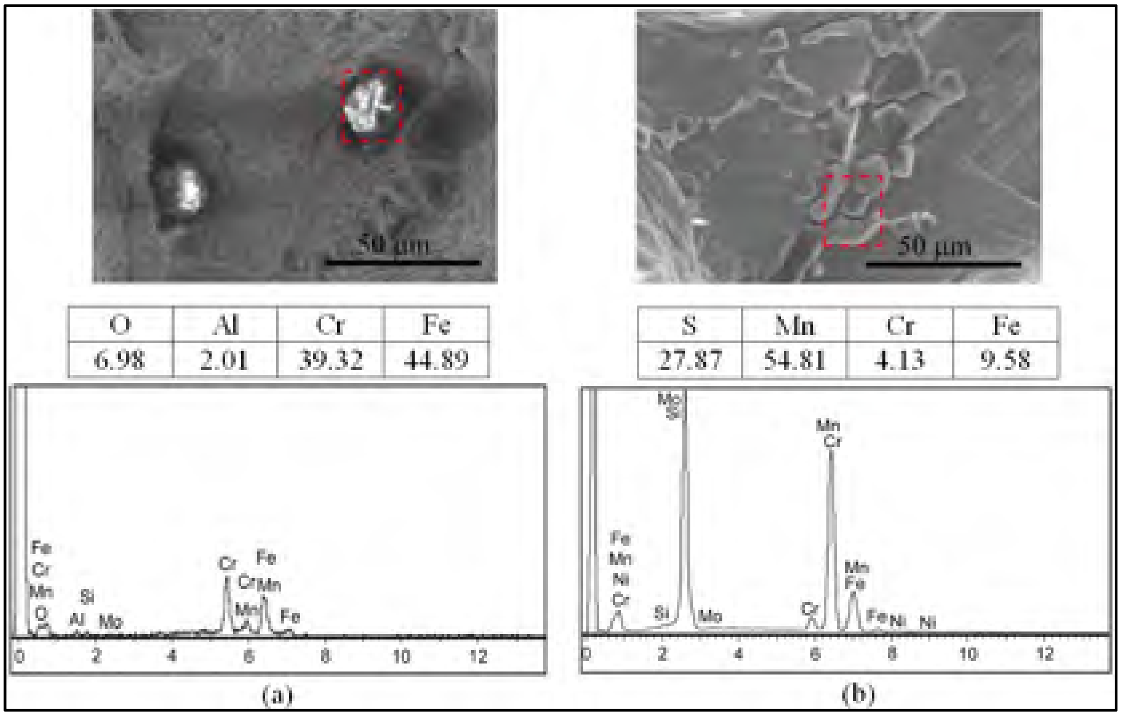

O	Al	Cr	Fe
6.98	2.01	39.32	44.89

S	Mn	Cr	Fe
27.87	54.81	4.13	9.58

Figure 2-14 SEM-EDS analyses of the tensile fracture surfaces of the weld Manufactured at a welding speed of 1.0 m/min

By contrast, newly-formed microvoids during tensile loading can also grow and coalesce into cracks. As shown in Figure 2-12, the cracks appearing during tensile loading can form and propagate mainly along the primary delta ferrite/martensite interfaces (Figure 2-12e) and within the martensite matrix (Figure 2-12d). The third possible crack path is across the primary delta ferrite, as shown in Figure 2-12c. Decohesion at the delta ferrite/martensite interfaces (Figure 2-12e) may be attributed to the weak bonding characteristics between these phases and/or local stress concentration effects due to their different physical properties and stress-strain response [33]. In the necked region of the tensile sample, cracking through the martensite matrix was apparent (Figure 2-12d) and is likely associated with void formation, growth and coalescence within the martensite interfaces, as reported previously for dual phase martensitic/ferritic steels [33]. These voids can be typically observed as dimples on the fracture surfaces, as illustrated in Figure 2-13g-i. In addition, the occurrence of cracks around inclusions was visible on the tensile fracture surface, as shown in Figure 2-14a-b. In particular, two types of inclusions were identified in the CA6NM BM, namely oxides (e.g. chromium oxide) and sulfides (e.g. MnS), as supported by the SEM-EDS results given in Figure 2-14a- b. Hence, during tensile loading, decohesion between these inclusions and the martensitic matrix occurs, which then leads to void formation and growth along the particle/matrix interfaces [34].

2.3.4.3 Charpy impact properties

The Charpy V-notch impact energies for the welds tested at 255ºK (-18°C), as listed in Table 2-3 (each value is the average of two measurements with the notches inside the FZ), increased from ~20.5 J to ~28.5 J with increasing welding speed from 0.75 m/min to 1.2 m/min. In the as-welded condition, the impact energy values for the hybrid laser-arc welds were lower than the current minimum requirement specified by Alstom for hydroelectric turbine manufacturing [35]. However, for the weld assembled at higher welding speed of 1.2 m/min, the impact energy value (in the as-welded condition) met the minimum requirement of 27 J according to ASME Section VIII, Div.1, which is of interest for heavy manufacturing industry in term of increased productivity and mechanical property at higher welding speed (1.2 m/min). As post-weld heat treatment is typically applied to welded CA6NM, these impact energy results for the hybrid laser-arc welds in the as-welded condition are quite promising for hydroelectric turbine manufacturing. Moreover, the properties in the as-welded condition may be sufficient for other applications of CA6NM (e.g. pressure vessels), which may allow elimination of post-weld tempering and important energy savings. With increasing welding speed, the observed increase in the impact energy may be related to a reduction in the prior-austenite grain size [36], which is possible due to the higher cooling rate (stemming from the lower heat input).

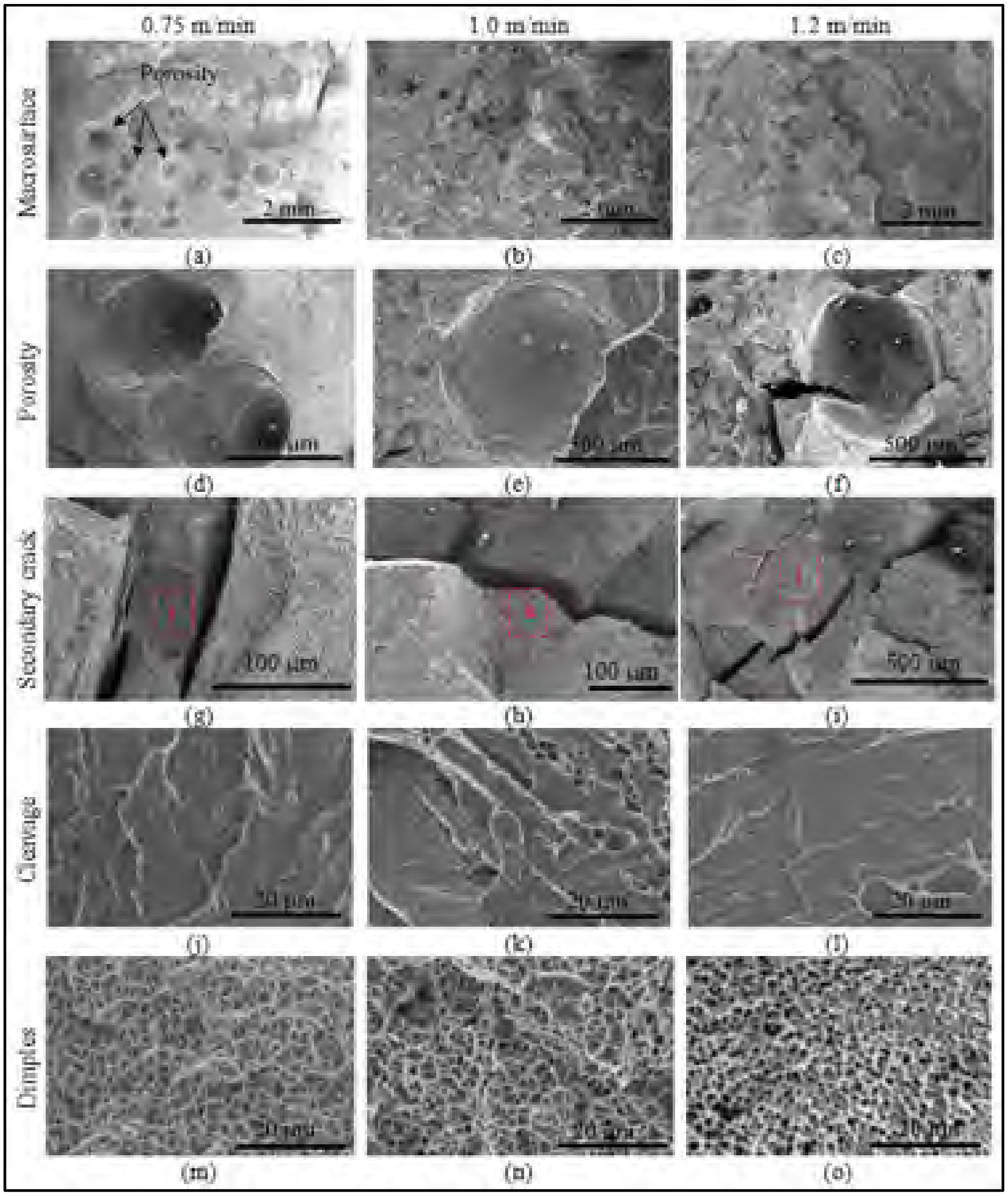
0.75 m/min
1.0 m/min
1.2 m/min
Macrosurface
Porosity
Secondary crack
Cleavage
Dimples
Porosity
2 mm
2 mm
2 mm
(a)
(b)
(c)
500 µm
500 µm
500 µm
(d)
(e)
(f)
100 µm
100 µm
500 µm
(g)
(h)
(i)
20 µm
20 µm
20 µm
(j)
(k)
(l)
20 µm
20 µm
20 µm
(m)
(n)
(o)

Figure 2-15 Fracture surfaces of Charpy impact tested samples of the welds assembled at different welding speeds

Also, the impact energy may be influenced by the porosity in the welds as observed from fractographic analysis of the fracture surface of the Charpy impact specimens that all failed in the FZ (Figure 2-15). For instance, the fracture surface for the weld assembled at 0.75 m/min exhibited a greater amount of porosity, relative to the higher welding speeds (1.0-1.2 m/min), which is consistent with the findings for the FZ from the metallographic observations and analysis (Figure 2-4b). Fractographic analysis of the Charpy impact tested welds also indicated the presence of some secondary cracks on the fracture surface that typically followed a cleavage fracture path, as displayed in Figure 2-15g-i. More specifically, these cracks appeared to propagate along the primary delta ferrite/martensite interface (Figure 2-15g) as well as between martensite packet grain boundaries (Figure 2-15h-i). These observations corroborate well with previous findings of secondary crack propagation within the martensite matrix and delta ferrite/martensite interface for Charpy impact tested welds in a similar low carbon supermartensitic stainless steel [21].

At higher resolution, the Charpy impact fracture surface featured a mixture of brittle and ductile characteristics, as evidenced by the cleavage facets with river patterns (Figure 2-15j-i) and fine equiaxed dimples (Figure 2-15m-o), respectively. The dimples were relatively shallow for the weld assembled at 0.75 m/min (Figure 2-15m) and increasingly became deeper in the welds assembled at higher welding speeds (i.e. Figure 2-15n and Figure 2-15o). Dimples present on ductile fracture surfaces are a result of microvoid formation and coalescence; finer and deeper dimples are indicative of high energy absorption that occurs in ductile materials [37]. Hence, the deeper dimples on the Charpy impact fracture surface of the welds assembled at higher welding speeds is indicative of a finer microstructure and higher energy absorption which corroborates well with the higher Charpy impact energy results obtained.

2.4 Conclusions

Hybrid laser-arc welding (HLAW) of cast low carbon 13%Cr-4%Ni martensitic stainless steel CA6NM, using ER410NiMo filler metal, was carried out at different welding speeds. The following conclusions can be drawn in terms of the macroscopic aspects (weld geometries and defects), metallurgical phenomena (microstructures in fusion and heat affected zones) and mechanical properties (hardness, ultimate tensile strength and Charpy impact energy) in the as-welded condition.

1. The area and width of the fusion zone in the CA6NM hybrid laser-arc welds decreased by 17.8% and 13.0%, respectively, as the welding speed increased from 0.75 m/min to 1.2 m/min. The comparison of the laser and arc welding processes at a welding speed of 0.75 m/min showed that the maximum bead-on-plate penetration depth for the fiber laser (5.2 kW power) is twice that of the MIG (7.9 kW power); this ascribes well the predominant contributions of the two processes in HLAW – laser for deep penetration and arc for gap tolerance.
2. The most common welding defects observed in the fusion zone were root humping, porosity, underfill and excessive penetration. Root humping was observed only at a welding speed of 0.5 m/min and was associated with severe porosity and underfill. Increasing the welding speed resolved the root humping defect and gave integral welds with a low amount of porosity. Both underfill and excessive penetration decreased with increasing welding speed. At welding speeds of 0.75 m/min and above, the maximum amount of underfill and excessive penetration met the acceptance criterion for the highest requirement (Class B) on a finished weld in ISO 12932.
3. The fusion zone of the CA6NM hybrid laser-arc welds in the as-welded condition consisted of lath martensite and some residual delta ferrite remaining mainly at the prior-austenite grain boundaries.
4. The single pass hybrid laser-arc welds exhibited four, easily identifiable and different HAZs that were interpreted according to the Fe-Cr-Ni phase diagram based on metallographic observations. The room temperature microstructure of HAZ2 consisted predominately of coarse untempered martensite, while HAZ3 exhibited a refined microstructure of untempered martensite and residual delta ferrite. In HAZ4, the microstructure was also predominately untempered martensite, but it was reasoned to be hardened from the complete or partial dissolution of chromium carbides. HAZ5 showed a mixture of both tempered and untempered martensite.

5. The average hardness in the fusion zone increased slightly with welding speed – from 345 HV at 0.5 m/min to 355 HV at 1.2 m/min – probably due to the refined and hardened martensitic microstructure. The maximum hardness occurred in HAZ4, close to the HAZ3/HAZ4 boundary. Based on a 2D hardness color contour map, HAZ4 could be subcategorised into three different areas – HAZ4a, HAZ4b and HAZ4c – according to the extent of chromium carbide dissolution, namely full, partial and none. Specifically, the highest hardness in HAZ4a was attributed to complete dissolution of the carbides that would increase the carbon content and the hardness of the martensitic matrix. The minimum hardness was found in HAZ5. The local softening in HAZ5 was related to further tempering of the CA6NM alloy that resulted in the formation of reversed austenite and softened tempered martensite in this zone.
6. In the as-welded condition, the hybrid laser-arc welds failed in the base metal during tensile loading. The ultimate tensile strength values for the integral welds in the as-welded condition were much higher than the minimum requirement of 755 MPa for CA6NM in the annealed and tempered condition, according to the ASTM A743 specification. Microstructural analysis near the fracture surface showed that the cracks during tensile loading can propagate in the CA6NM base metal along three different paths: (1) primary delta ferrite/ martensite interface by a decohesion-induced cracking mechanism, (2) the interfaces between the martensite laths and (3) within the primary delta ferrite. Fractographic analysis of the tensile fracture surfaces indicated the presence of dimples, as well as gas porosities, shrinkage porosities and inclusions (oxides and manganese sulfide); these latter were remnant defects in the cast structure of the CA6NM base metal that led to the tensile failure.
7. Charpy V-notch impact testing showed a slight increase in the impact energy for the weld assembled at the highest welding speed (1.2 m/min), which was attributed to the microstructural refinement. Fractographic analysis of the fracture surfaces after Charpy impact testing of the welds indicated the presence of microcracks and a crack path through both the martensite packet grain boundaries and delta ferrite/martensite interfaces. A mixed dimple-cleavage fracture mode was observed for all specimens

but deeper dimples were observed on the fracture surface of the weld assembled at higher welding speeds, which corroborates well with the higher measured Charpy impact energy values.

8. As post-weld tempering is typically applied to CA6NM, achievement of the good tensile strength and impact energy values in the as-welded condition indicates that hybrid laser-arc welding has good potential for hydroelectric turbine manufacturing.

Acknowledgements

The authors would like to thank Alstom Canada, Hydro-Québec and the National Science and Engineering Research Council of Canada (NSERC) for their financial support. The technical assistance of E. Poirier and X. Pelletier of NRC Aerospace during the welding experiments and metallographic preparation is gratefully acknowledged. Thanks are also due to Alstom for the funding the tensile and Charpy impact testing at Mequaltech (Montreal, QC).

References

1) X. Cao, P. Wanjara, J. Huang, C. Munro and A. Nolting: Mater. Design, 2011, vol. 32, pp. 3399-413.
2) C. Bagger, F.O. Olsen, J Laser Appl, 2005, 17, pp. 2-14.
3) F. Mirakhorli, X. Cao, X.T. Pham, P. Wanjara and J-L. Fihey: MS&T 2014 Conf. Pittsburgh, PA, USA, 2014, pp. 1891-900.
4) P. Bilmes, C. Llorente and M. Solari: 20th ASM Heat Treating Society Conf., St. Louis MO, USA, 2000, pp. 556-65.
5) A.K. De, D.C. Murdock, M.C. Mataya, J.G. Speer and D.K. Matlock: Scripta Mater., vol. 50, 2004, pp. 1445-49.
6) ASME Pressure Vessel code, Sec. IX: Welding and Brazing Qualifications, 2009.
7) ASME Pressure Vessel code. Sec. VIII., Div. 1, Rules for Construction of Pressure Vessels, 2009.
8) T. Ilar, I. Eriksson, J. Powell, A. Kaplan, Physics Procedia, 2012, vol. pp. 27-32.
9) ISO 12932: Laser-Arc Hybrid Welding of Steels, Nickel and Nickel Alloys — Quality Levels for Imperfections, 2013.

10) Kabir, X. Cao, M. Medraj, P. Wanjara, J. Cuddy and A. Birur: MS&T 2010 Conf., Houston, TX, USA, 2010, pp. 2787-97.

11) Casalino G, Mortello M, Leo P, Benyounis KY, Olabi AG: Mater. Design, 2014; vol. 61, pp. 191-8.

12) X. Cao, W. Wallace, J.-P. Immarigeon and C. Poon: Mater. Manuf. Processes., 2003, vol. 18, pp. 23-49.

13) N. Seto, S. Katayama and A. Matsunawa: Weld. Int., 2002, vol. 16, pp. 451-60.

14) D. Abbott and C. Albright, J. Laser Appl., 2012, vol. 6, pp. 69-80.

15) E. Folkhard, G. Rabensteiner and E. Perteneder: Welding metallurgy of stainless steels, Springer-Verlag Vienna, 1988, pp. 9-125.

16) D. Carrouge: PhD thesis, University of Cambridge, 2003.

17) J. Enerhaug and U. Steinsmo: Sci. Technol. Weld. Joining, 2001, vol. 6, pp. 330-38.

18) D. Thibault, P. Bocher and M. Thomas: J. Mater. Process. Technol., 2009, vol. 209, pp. 2195-202.

19) S. Sarafan, P. Wanjara, H. Champliaud and D. Thibault: Int. J. Adv. Manuf. Technol., vol. 78, 2015, pp. 1-13.

20) H. Kitahara, R. Ueji, N. Tsuji and Y. Minamino: Acta Mater, 2006, vol. 54, pp. 1279-88.

21) D. Carrouge, H. Bhadeshia and P. Woollin: Sci. Technol. Weld. Joining, 2004, vol. 9, pp. 377-89.

22) Y.-K. Lee, H.-C. Shin, D.-S. Leem, J.-Y. Choi, W. Jin and C.-S. Choi: Mater. Sci. Technol., 2003, vol. 19, pp. 393-98.

23) O. Akselsen, G. Rorvik, P. Kvaale and C. Van der Eijk: Weld. J., 2004, vol. 83, pp. 160-67.

24) S. Mrowec and S. Marcinkiewicz: Defects and diffusion in solids: an introduction, Elsevier Amsterdam, 1980, pp.174-300.

25) C. Garcia de Andres, G. Caruana and L. Alvarez: Mater. Sci. Eng. A.,1998, vol. 241, pp. 211-15.

26) D. Zou, Y. Han, W. Zhang and X. Fang: J. Iron Steel Res. Int., 2010, vol. 17, pp. 50-54.

27) J.C. Lippold and D.J. Kotecki: Welding metallurgy and weldability of stainless steels, Wiley-VCH, 2005, pp. 59-86.

28) Trudel, M. Sabourin and M. Brochu: Int. J. Fatigue, 2014, vol. 66, pp. 39-46.

29) K.Y. Benyounis, A.G. Olabi and M.S.J. Hashmi: J. Mater. Process. Technol., 2005 vol. 164, pp. 978-85.

30) Y. Song, X. Li, L. Rong, D. Ping, F. Yin, Y. Li, Materials Letters, 2010, vol. 64 pp. 1411-14.

31) ASTM A 743/A 743M – 03, Standard Specification for Castings, Iron-Chromium, Iron-Chromium-Nickel, Corrosion Resistant, for General Application, 2003.

32) E.B. A. Akhiate, D. Thibault, and M. Brochu: COM 2014, Vancouver, BC, Canada, 2014.

33) G. Avramovic-Cingara, C.A. Saleh, M. Jain and D. Wilkinson: Metall. Mater. Trans. A, 2009, vol. 40, pp. 3117-27.

34) M. Azuma, X. Huang and G. Winther: PhD thesis, Technical University of Denmark, 2013.

35) L. Mathieu, ALSTOM Company, Sorel-Tracy, Quebec, private communication, 2014.

36) G.E. Dieter and D. Bacon: Mechanical metallurgy, McGraw-Hill New York, 1986, pp. 471-500.

37) M. McDonald and D. Ludwigson: J. Test. Eval., 1983, vol. 11, pp. 165-73.

CHAPTER 3

POST-WELD TEMPERED MICROSTRUCTURE AND MECHANICAL PROPERTIES OF HYBRID LASER-ARC WELDED CAST MARTENSITIC STAINLESS STEEL CA6NM

F. Mirakhorli[1,2], X. Cao[1,2], X-T. Pham[1], P. Wanjara[2] and J. L. Fihey[1]

[1]École de technologie supérieure, Montréal, Québec, Canada, H3C 1K3
[2]National Research Council Canada – Aerospace, Montréal, Québec, Canada, H3T 2B2

- This paper is published in Metallurgical and Materials Transactions B, in press, 2016.

Keywords: Hybrid laser-arc welding (HLAW); Cast stainless steel; Post-weld heat treatment; Microstructure; Mechanical properties.

Abstract

Manufacturing of hydroelectric turbine components involves the assembly of thick-walled stainless steels using conventional multi-pass arc welding processes. By contrast, hybrid laser-arc welding may be an attractive process for assembly of such materials to realize deeper penetration depths, higher production rates, narrower fusion and heat-affected zones, and lower distortion. In the present work, single-pass hybrid laser-arc welding of 10-mm thick CA6NM, a low carbon martensitic stainless steel, was carried out in butt joint configuration using a continuous wave fiber laser at its maximum power of 5.2 kW over welding speeds ranging from 0.75 m/min to 1.2 m/min. The microstructures across the weldment were characterized after post-weld tempering at 873 K (600 °C) for 1 hour. From microscopic examinations, the fusion zone was observed to mainly consist of tempered lath martensite and some residual delta ferrite. The mechanical properties were evaluated in the post-weld tempered condition and correlated to the microstructures and defects. The ultimate tensile strength and Charpy impact energy values of the fully penetrated welds in the tempered condition were acceptable according to ASTM, ASME and industrial specifications, which bodes well for the introduction of hybrid laser-arc welding technology for the manufacturing of next generation hydroelectric turbine components.

NOMENCLATURE

Ac_1	Temperature at which austenite begins to form during heating
BM	Base metal
EBW	Electron beam welding
FCAW	Flux core arc welding
FZ	Fusion zone
GMAW	Gas metal arc welding
GTAW	Gas tungsten arc welding
HAZ	Heat-affected zone
HLAW	Hybrid laser-arc welding
M_f	Martensite finish temperature
M_s	Martensite start temperature
OM	Optical microscopy
PMZ	Partially melted zone
PWHT	Post-weld heat treatment
SEM	Scanning electron microscopy

3.1 Introduction

Hydropower is one of the most widely used renewable sources of energy for electricity generation. Considering the long-service life of hydropower systems that can operate for more than five decades, proper design and manufacturing are critical for achieving high performance with low operational and maintenance costs. The most important part of any hydraulic power system is the turbine that is an assembly of various sub-components, e.g., runner blades, crowns and bands. These components are fabricated commonly from thick-walled stainless steel materials, such as CA6NM, which is a low carbon martensitic grade that is manufactured in cast form and has high strength, good toughness and corrosion resistance [1]. However, assembly of large hydroelectric turbine components is a great challenge from the perspective of the highly complex blade geometry and sizeable overall dimensions. Thus, the manufacturing quality and cost of the turbine are highly dependent on the ability to join such low carbon cast martensitic stainless steel components using methods that can provide high productivity, low material consumption and good joint integrity with any imperfections and distortion remaining within acceptable levels. To date, due to the relatively low investment costs of manual and semi-automatic arc welding systems, such as GTAW, GMAW and FCAW, arc welding with filler material has been widely used in industry to assemble the turbine. However, joints welded using arc-based manual welding processes exhibit a relatively large HAZ, high residual stresses, and distortion due to the considerable heat input and large thermal gradients from the multiple passes required for assembly. Also, compared to more advanced processes, the operational cost for assembly is high for arc welding due to its relatively slow speed (low production rate), high labor intensity and cost of skilled welders, and considerable consumable costs; this latter is related to the small penetration depth that requires extensive grooving of the thick joint seam followed by multiple welds deposited with filler metal addition under shielding gas protection. In the present context, where the capital expenditure for advanced manufacturing systems has decreased considerably, the high operating expenditure of arc welding processes may override their manufacturing sustainability. Hence investment in the development and introduction of alternative advanced welding and/or repair technologies that can improve the weld quality and performance, whilst reducing the overall fabrication costs, is necessary for turbine manufacturers to be sustainable and cost-efficient in a global market.

For hydroelectric turbine assembly, the HLAW process has the potential to offer a highly competitive solution to improve the overall performance by combining the high energy density of the laser technology for deep penetration at a high production rate with the feeding ability of an arc process for good gap bridging [2]. Hence, the synergistic interactions of the laser and arc heating sources in HLAW enable full penetration in thick gage sections using a single pass or fewer passes – depending on the laser power – that, in turn, reduce the heat input, size of the FZ and HAZ, thermal cycling, residual stresses and distortion in the assembly, relative to conventional arc welding alone. Also, though the initial capital investment required for HLAW is higher, sufficient leveraging is achievable through the associated reductions in operational costs (consumables, labor, machining preparations) and the increased production rate, to warrant a profitable return on investment.

Consequently, in the present work, a single-pass HLAW process was developed to join 10-mm thick CA6NM martensitic stainless steel plates at three different welding speeds, namely 0.75, 1.0 and 1.2 m/min. Post-weld tempering at 873 K (600 °C) for 1 hour was applied according to the recommended guidelines in ASME sec. IX for welding and brazing qualifications under the boiler and pressure vessel regulations. The microstructure of the welds in the tempered condition was characterised using OM and SEM. The mechanical performance of the tempered welds was evaluated through measurement of the microindentation hardness, ultimate tensile strength and Charpy impact energy, which were then correlated to the microstructural evolution. The failure mechanisms during tensile deformation and Charpy impact loading were examined by scanning electron microscopy, fractography and optical metallographic analysis near the fracture origin.

3.2 Experimental

Cast ASTM A743 grade CA6NM was received in plate form with a chemical composition as listed in Table 3-1. The 10-mm thick as-received plates were extracted from a newly cast CA6NM turbine runner blade and were heat treated as follows: (1) normalizing by first heating at a rate of 60 K/hr (60 °C/hr) to 1073 K (800 °C) and holding for 8 hrs followed by heating at a rate of 25 K/hr (25 °C/hr) to 1303 K (1030 °C) and holding for 27 hrs, (2) air cooling to a temperature below the martensite finish temperature (Mf ≈ 363 K (90 °C)), and (3) tempering by heating at a rate of 36 K/hr (36 °C/hr) to 913 K (640 °C) and holding for 27 hrs followed by cooling at a rate of of 25 K/hr (25 °C/hr). The CA6NM plates were then machined into coupons of 150 mm × 75 mm × 10 mm for the HLAW trials.

The laser equipment consisted of an IPG photonics 5.2 kW continuous wave solid-state Yb-fiber laser attached to an ABB robotic mounting arm. A collimating lens of 200 mm, a focal lens of 300 mm and a fiber diameter of 0.20 mm were employed to produce a nominal focusing spot diameter of 0.30 mm. The defocusing distance was 2.5 mm under the workpiece top surface and the laser head was inclined 5° from the vertical position during welding. A Fronius Trans Pulse Synergic 4000 CMT (Cold Metal Transfer) GMAW power supply was used in tandem with this laser system. The top surface of the workpiece was shielded using a mixture of 96% argon and 4% oxygen at a flow rate of 23.6 l/min that was fed through a GMAW nozzle, while the bottom surface was shielded using 100% argon at a flow rate of 9.5 l/min.

A single-pass HLAW process was developed to obtain full penetration in 10-mm thick CA6NM plates with a Y-groove shape butt joint having a bevel angle of 30º. The root size was 5 mm with a gap size of about 0.2 mm. The chemical composition of the AWS ER410NiMo filler wire (ϕ 1.14 mm) that was used is given in Table 3-1. As indicated in Table 3-2, HLAW was conducted at different welding speeds and the highest accessible laser power in "laser leading" mode. In accordance with recommended guidelines, post-weld tempering was performed on the welded assemblies according to ASME Section IX at a holding temperature of 873 K (600 °C) for 1 hr at heating and cooling rates of 50 K/hr (50 °C/hr).

Table 3-1 Chemical composition of cast CA6NM stainless steel and ER410NiMo filler metal

Elements	**C**	**Si**	**Mn**	**P**	**S**	**Cr**	**Ni**	**Mo**	**Cu**	**Others**
CA6NM	0.041	0.454	0.756	0.032	0.008	13.28	4.31	0.520	0.071	0.11
410NiMo	0.02	0.37	0.34	0.017	0.0009	12.18	4.57	0.42	0.12	-

After HLAW, the top and bottom surfaces of the welds were slightly machined prior to extracting metallographic, transverse tensile and Charpy impact specimens to remove the underfill on the crown and reinforcement at the root, which reduced the joint thickness to 9 mm. The two transverse metallographic specimens extracted from each weld were ground with successively finer SiC papers from 220 to 1200 grit, polished using 3 and 1 μm diamond suspensions, and finally etched electrolytically in 10% oxalic acid solution to observe the general macrostructure or chemically in Beraha's reagent (1 g K2S2O5 + 20 ml HCl + 80 ml H2O) to reveal the martensite and delta ferrite microstructures. The delta ferrite was also revealed by electro-etching in a 20% aqueous solution of NaOH at room temperature. The microstructure of the welds was examined using an inverted optical microscope (Olympus GX71) and a Hitachi 3600N scanning electron microscope. Microhardness profiles across the welds were measured using a Vickers micro-indentation machine (Struers Duramin A300) at a load of 200 g, a dwell period of 15 s and an interval of 0.15 mm between each indentation.

Table 3-2 Experimental design for HLAW

Sample #	**Laser power (kW)**	**Welding speed (m/min)**	**Wire feed rate (m/min)**	**Arc voltage (V)**	**Arc current (I)**	**Arc power (kW)**
1	5.2	0.75	12	28	283	7.9
2	5.2	1.0	16	30	352	10.6
3	5.2	1.2	19	30	349	10.5

Tensile and Charpy impact tests were conducted according to ASME Section IX and VIII, respectively. The flat rectangular transverse tensile specimens had a gage length of 20 mm, a width of 13 mm and a thickness of 9 mm (Figure 3-1a). It is noteworthy that the FZ and entire HAZ of the hybrid laser-arc welds could be located within the 20 mm gage length of the tensile specimen. The tensile tests were conducted at room temperature using a 300 kN Tinius Olsen frame.

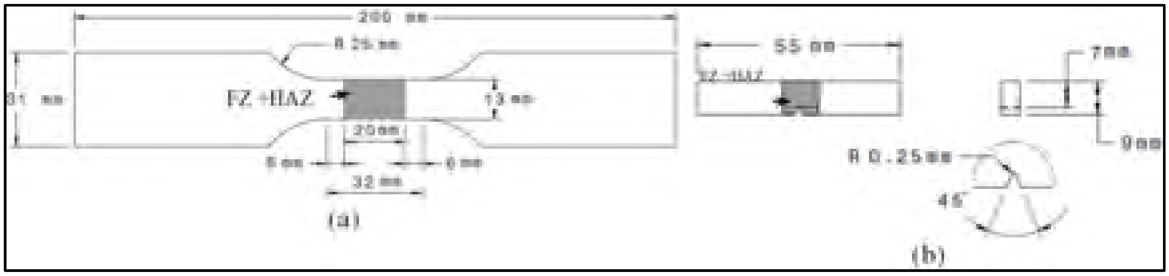

Figure 3-1 Specimen geometries for (a) transverse tensile (where the FZ is centered within the demarcated shaded region) and (b) Charpy impact tests

The Charpy impact specimen size was 55 mm × 9 mm × 10 mm with a 2-mm deep V-notch located in the weld metal through the thickness (Figure 3-1b). The Charpy impact tests were conducted at 255 K (-18 °C) using a weighted pendulum hammer on a SATEC SI-1C3 system. The fracture surfaces of both the tensile and impact specimens were examined by SEM. In addition, the microstructure near the fracture origin was also observed by OM after the tensile tests.

3.3 Results and discussion

3.3.1 Macrostructure

Figure 3-2 shows a typical transverse section of a fully-penetrated weld produced at a welding speed of 1.0 m/min.

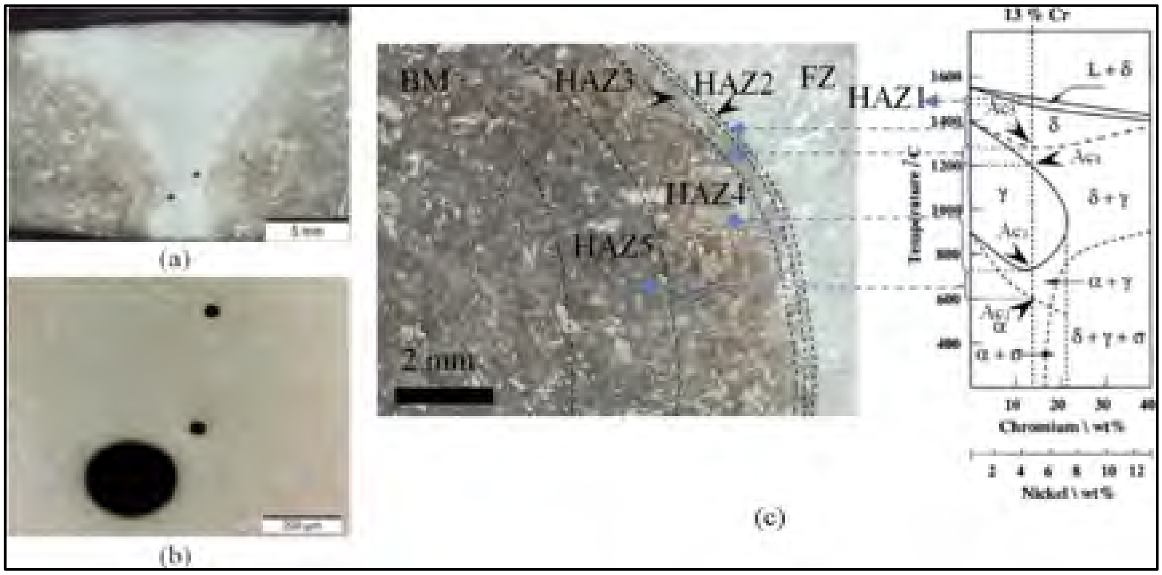
5 mm
(a)
200 μm
(b)
BM
HAZ3
HAZ2
FZ
HAZ1
HAZ4
HAZ5
2 mm
(c)
13 % Cr
L + δ
δ
γ
δ + γ
α + γ
δ + γ + σ
α + σ
α
Temperature / °C
1600
1400
1200
1000
800
600
400
Chromium \ wt %
10
20
30
40
Nickel \ wt %
2
4
6
8
10
12

Figure 3-2 Macrostructure showing the FZ and HAZ located within the gage length of a transverse tensile specimen (at a welding speed of 1.0 m/min), (b) typical porosity in the FZ, and (c) macrostructure from the FZ to the BM according to a Fe-Cr-Ni ternary diagram

Some porosity was observed in the FZ near the root (Figure 3-2b), probably due to the precipitation of dissolved gas at solid/liquid interface during solidification and/or the collapse of unstable keyholes [3]. The macrostructure of the different HAZs near the fusion boundary after post-weld tempering that is illustrated in Figure 3-2c was constructed from the equilibrium ternary phase diagram of Fe-Cr-Ni at 13% Cr and 4% Ni [4]. Based on this phase diagram, five different HAZs in the as-welded state can be predicted. Located adjacent to the fusion boundary, HAZ1 involves heating into the L + δ region and is often referred to as the PMZ. In the hybrid laser-arc welds, HAZ1 was not distinguishable as noted by its absence in Figure 3-2c. This finding is similar to that reported previously for FCAW [5], GTAW [6] and EBW of martensitic stainless steels [7]. In HAZ2, termed as the coarse grain HAZ, complete transformation of the BM microstructure to the delta ferrite (δ) occurs during heating into the high temperature single phase δ region. HAZ3 develops from heating into the high temperature two-phase δ + γ region where partial transformation of the austenite (γ) matrix to delta ferrite happens during heating. HAZ4 is from the single-phase γ region where the BM has completely transformed to austenite during heating. HAZ5 is the low temperature dual-phase α' + γ region that is characterized by partial transformation of tempered martensite (α') to austenite during heating. It is noteworthy that differentiation of the different HAZs in the post-weld tempered microstructure was difficult and thus the various regions were identified in Figure 3-2c by inferring from their position through superposition with the as-welded condition that was reported in our earlier work [3].

3.3.2 Microstructure

The BM microstructure was investigated using OM and SEM, as shown in Figure 3-3. Since all the joints were tempered after welding, the BM itself was double-tempered. However, the BM microstructures in the post-weld tempered and as-received conditions were quite similar, consisting of tempered lath martensite with some coarse primary delta ferrite (pri- δ) that formed during casting. Specifically, each martensite grain was noted to consist of several packets within which parallel blocks of narrow ruler shaped laths were apparent, as reported previously [8]. According to literature, some retained austenite may also be present as a finely dispersed phase between the martensite laths [1]. This BM microstructure, as observed in this study, is consistent with that reported previously for a similar BM composition [7, 5].

The FZ microstructures after post-weld tempering (Figure 3-4) consisted of tempered lath martensite. The use of Beraha’s reagent as an etchant produced some color contrast between the grains of the tempered lath martensite under OM. The coloration is mainly due to the varying thickness of the oxide or sulfide films deposited on the specimen surface after reaction with the reagent and to the different crystallographic orientations of the grains [9].

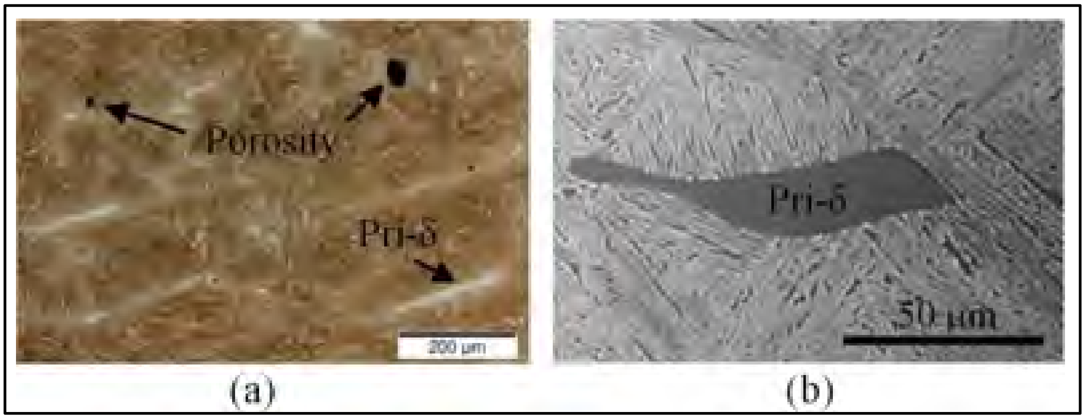

Figure 3-3 BM microstructures by (a) OM and (b) SEM

The pri-δ, present originally in the BM (that was a remnant from the casting process), was not apparent in the FZ and its dissolution is consistent with heating above the liquidus of the alloy. However, delta ferrite was observed at prior austenite grain and sub-grain boundaries, as shown in Figure 3-4b after electro-etching in 20%NaOH. The tempered lath martensite and delta ferrite were observed at higher resolution under SEM, as shown in Figure 3-4c. Compared to the as-welded condition [3], no visible variations in the delta ferrite morphology were observed in the FZ after post-weld tempering due to the low tempering temperature (873 K (600 °C)) used. Though not resolved in this work, there is also a strong likelihood that reversed austenite is present in the tempered martensitic FZ microstructure. Specifically, Song et al. [10] observed that the tempering of lath martensite can be accompanied by the formation of reversed austenite along the martensite lath boundaries, since the decomposition of martensite into austenite starts at a temperature around 873 K (600 °C), depending on the C, Mn and Ni contents [11, 12].

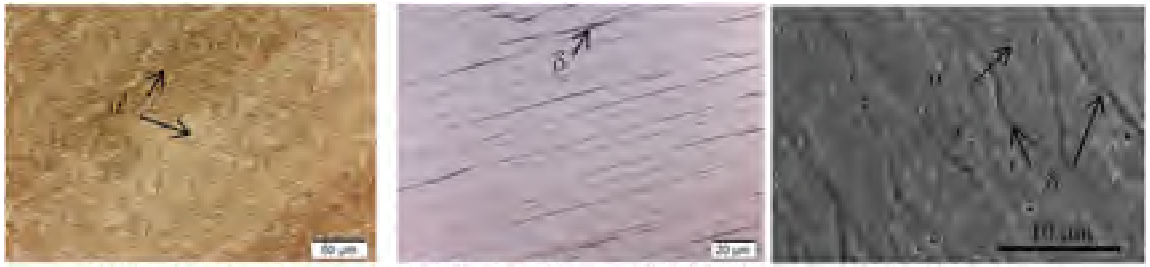

(a) Beraha's reagent (b) Electro-etching in 20%NaOH (c) Beraha's reagent

Figure 3-4 FZ microstructure in the weld assembled at 1.0 m/min by (a,b) OM and (c) SEM

For example, Akhiate et al. [11] measured the Ac_1 temperature in the range of 835 K – 880 K (562 °C – 607 °C) for different CA6NM plates with 0.033-0.067% C and found that during post-weld tempering at 873 K (600 °C) for 1 hr, the untempered hard martensite in the FZ can partially transform to austenite. Song et al. [13] found that the formation of reversed austenite during tempering from 843 K – 953 K (570 °C to 680 °C) is mainly controlled by a diffusional process and, in the presence of rich solute elements (Ni, Cr and Mn), the reversed austenite formed can remain stable even at room temperature. Also, Bilmes et al. [1] remarked that a high density dislocation is a structural barrier to the transformation of shear-controlled martensite that then stabilizes austenite. Song et al. [13, 14] examined with transmission electron microscopy the precipitation of Cr-rich carbides ($M_{23}C_6$) during tempering and proposed that these precipitates deplete Cr from adjacent areas, whilst enriching Ni (an austenite stabilizer) because the Cr carbides have little Ni solubility. As such, Song et al. [10, 14] remarked that this could provide suitable sites for austenite nucleation near the carbides. These various reported findings then lend convincing assurance to the strong probability of forming and retaining austenite in the FZ of the CA6NM hybrid laser-arc welds in the tempered condition.

The post-weld tempered microstructures of the different HAZs are shown in Figure 3-5. As mentioned, HAZ1 (or the PMZ) could not be distinguished from the FZ probably due to its (i) very narrow size that stems from the very narrow solidification temperature range of ~ 30 K (30 °C) [4] and/or (ii) microstructural similarity with that of the FZ.

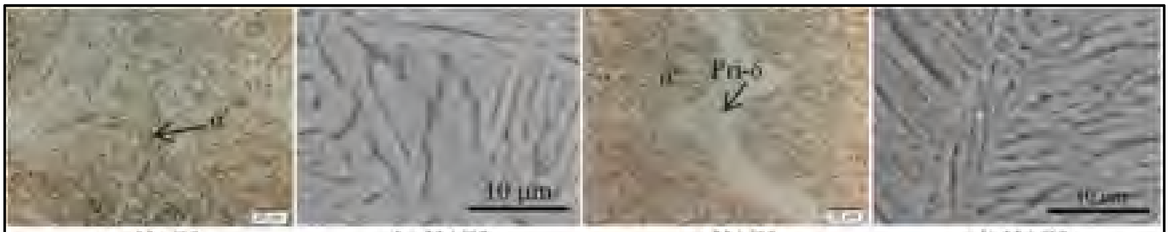

(a) HAZ2 (b) HAZ2 (c) HAZ3 (d) HAZ3

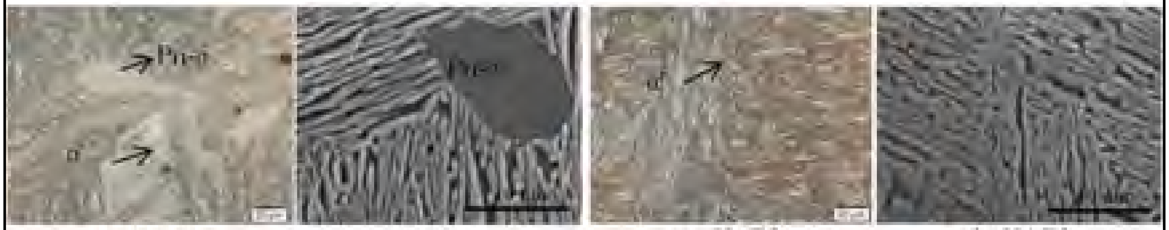

(e) HAZ4 (f) HAZ4 (g) HAZ5 (h) HAZ5

Figure 3-5 Microstructural evolution in the various HAZs of the weld assembled at 1.0 m/min

In both HAZ2 (Figure 3-5a-b) and HAZ3 (Figure 3-5c-d), a tempered martensitic microstructure was observed, with the exception that the grain structure in HAZ2 was coarser than that in HAZ3. The occurrence of these microstructures in HAZ2 and HAZ3 can be explained from the heating cycle during welding that exposes these regions to a temperature range where single phase δ and dual phase δ + γ regions are respectively present, as illustrated in Figure 3-2c. However, considerable grain growth occurs when heating to the single phase δ region, and, as such, the grain structure in HAZ2 coarsens [5]. On cooling, the high temperature phases (δ and γ) undergo transformations and eventually reverse to martensite that is untempered. After tempering at 873 K (600 °C), the tempered lath martensite remains coarser in HAZ2 than in HAZ3. In HAZ4 (Figure 3-5e-f) and HAZ5 (Figure 3-5g-h), the martensitic microstructures after tempering appeared remarkably similar. However, noticeable hardness differences between the microstructures in HAZ4 and HAZ5 for the tempered hybrid laser-arc welds are present, as will be discussed in the next section. Here we can contemplate the phase transformation occurring on heating during welding into the single phase γ region (HAZ4) or low temperature dual phase (α' + γ) region (HAZ5) using again the phase diagram given in Figure 3-2c. For instance, the gradual increase in the temperature across HAZ5 on heating during welding will increasingly transform the tempered martensite structure of the BM to austenite. However, considering the short time at the low temperature, complete transformation of the tempered martensite to austenite is unlikely in HAZ5 but should occur within HAZ4. On cooling, the austenite formed should reverse to martensite, which is untempered. Hence, in HAZ4, the microstructure at room temperature after welding is predominantly untempered martensite, whereas in HAZ5 both tempered and untempered martensite would be present and, depending on the location, in different relative fractions. Also, especially in HAZ5, some retained austenite may form due to the tempering thermal cycle applied to CA6NM. Tempering of this mixed microstructure in HAZ5 after welding would then lead to some changes in the untempered martensite, remnant tempered martensite and retained austenite. It is noteworthy to understand that the untempered martensite, whether in the FZ or HAZs, is unstable before tempering due to (i) the inherent supersaturated structure with carbon, which is formed by diffusionless martensite transformation, and (ii) the high dislocation density within martensite, which is related to the transformation of austenite to martensite that results in a slight increase in volume (~ 4%) and lattice invariant deformation [15, 16].

During tempering, the instability of the untempered martensite can act as a driving force and cause various changes in the matrix, e.g. rearrangement of carbon atoms and formation of carbides ($M_{23}C_6$), as well as a decrease in dislocation densities. Also, during tempering the high angle inter-lath boundaries are progressively replaced by low angle inter-lath boundaries, which render greater stability of the tempered martensite microstructure compared to the untempered martensite [15, 17]. Hence, during tempering the untempered martensite in HAZ5 and HAZ4 of the hybrid laser-arc welds will change to a tempered structure, as corroborated by Sarafan et al. [7] for post-weld tempered electron beam welds. In the case of the remnant tempered martensite in HAZ5, the second tempering (i.e. double tempering) can further reduce dislocation densities and cause stress release, leading to a more softened microstructure. Relative to the BM, the softening in HAZ5 is likely to be greater because of the additional exposure to the tempering temperature conditions during welding. Finally, reversed austenite can also form in HAZ5 during post-weld tempering. This austenite can nucleate adjacent to the carbides [14] or pre-existing retained austenite [18]. The austenite retained after welding may grow during tempering and become less stable after growth. In addition, it has been reported that the precipitation of $M_{23}C_6$ during tempering around 873 K (600 °C) can deplete Cr and C from both the martensite and retained austenite phases, which renders the latter less stable and prone to martensitic transformation during cooling after tempering [19, 20]. Moreover, the reversed austenite formed during tempering is more enriched in C and Ni compared to the retained austenite formed during the welding process, which renders greater stability [4, 21].

The effect of welding speed (0.75-1.2 m/min) on the tempered microstructures in the FZ and different HAZs was studied. However, no significant differences in the microstructure were observed for the range of welding speeds used, as corroborated from the microhardness measurements as discussed next.

3.3.3 Microindentation hardness

The hardness profiles across the FZ, HAZs and BM for the tempered welds, measured along the mid-thickness of a transverse section, are shown in Figure 3-6a-c. Similar trends were observed for the three welding speeds. Specifically, the microhardness appears to increase by about 7% from HAZ2 to HAZ4, where a maximum value occurs and then drop by about 9% in HAZ5, where a minimum value typically occurs (Table 3-3). For instance, examining the 1.0 m/min welding condition, the hardness evolves from a value of 289 ± 5 HV in HAZ2 to 294 ± 5 HV in HAZ3 and to a maximum of 310 HV in HAZ4. It is noteworthy that the narrow breadth of both HAZ2 and HAZ3 (~0.4-0.6 mm in width) limits the number of hardness measurements to 1–3 data points. Beyond the hardness maximum in HAZ4, the hardness decreased progressively and a minimum average value of 276 ± 6 HV was recorded in HAZ5. Compared to the as-welded condition, these microhardness values in HAZ2, HAZ3 and HAZ4 were lower by 55 ± 5 HV after post-weld tempering. The decrease in microhardness in HAZ2-HAZ4 after tempering may be due to (i) the formation of reversed austenite and tempered martensite, (ii) the release of residual stresses and (iii) a decrease in the dislocation density [22]. The occurrence of a hardness maximum in HAZ4 after post-weld tempering is related to the maximum temperature experienced during welding, which is close to the Ac_4 temperature in the single phase γ region, where partial or complete dissolution of the Cr-rich carbides ($M_{23}C_6$) can happen and lead to increased carbon supersaturation and lattice distortion of the martensitic matrix, and consequently higher hardness in the final microstructure [23]. Alternatively, the decrease in microhardness from HAZ4 to HAZ5, until reaching the minimum average value in HAZ5 is related to further tempering of the microstructure.

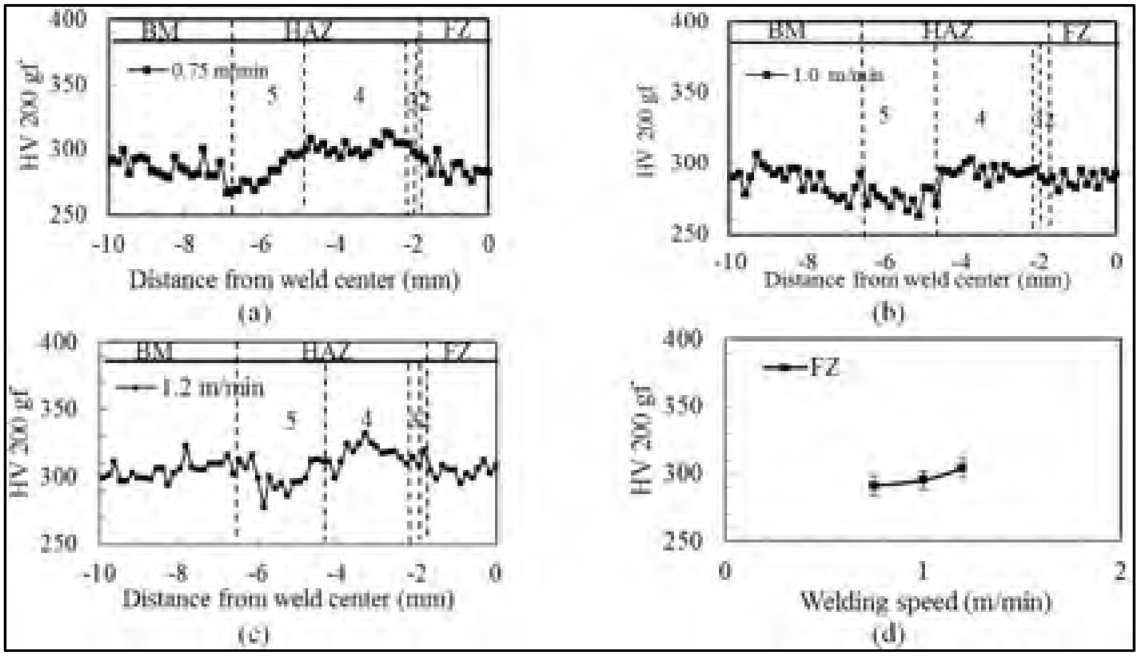

Figure 3-6 Hardness profiles of the tempered welds assembled at welding speeds of (a) 0.75 m/min, (b) 1.0 m/min, and (c) 1.2 m/min; (d) effect of welding speed on the FZ hardness (tempered condition).

As discussed above, the tempered and untempered martensite in HAZ5 would undergo tempering with the possible formation of new Cr-rich carbides ($M_{23}C_6$) and reversed austenite [24], which would cause softening relative to BM. Hence, the microhardness in HAZ5 is slightly lower than the value of the BM (294 ± 5 HV) after post-weld tempering, which was comparable to that reported for the as-received (i.e. normalized and tempered) BM (297 ± 12 HV). The softening phenomenon in the HAZ5 of tempered CA6NM hybrid laser-arc welds is in agreement with previous reported work on EBW [7] and FCAW [25] of CA6NM. Figure 3-6d shows the effect of the welding speed on the hardness values in the FZ (including HAZ1). The average FZ hardness (Table 3-3) tends to increase progressively from 291 ± 7 HV to 304 ± 7 HV with increasing welding speed from 0.75 m/min to 1.2 m/min due to increasing refinement of the prior-austenite grains [24] that, in turn, decreases the packet and block size of the lath martensite structure.

Table 3-3 Microhardness of the FZ and HAZs in the tempered welds
assembled at different welding speeds

Welding speed (m/min)	**Microindentation hardness**					
	FZ (Avg.)	**HAZ2 (Avg.)**	**HAZ3 (Avg.)**	**HAZ4 (Max.)**	**HAZ5 (Avg.)**	**HAZ5 (Min.)**
0.75	291	295	301	313	280	268
1.0	295	289	294	310	276	265
1.2	304	300	305	328	294	277

Also Hanamura et al. [26] found that the grain boundary density, especially the high angle grain boundary density, increases with decreasing austenite grain size (or higher welding speed). Moreover, the amount of lattice defects such as dislocations increases with increasing cooling rate (i.e. higher welding speed). Hence with increasing welding speed, the increased grain refinement and higher dislocation density can result in slightly harder martensite. Previously, using FCAW, Trudel et al. (2014) reported an average hardness of 320 HV in the tempered FZ of CA6NM and Thibault et al. (2009) reported 316 HV for the tempered FZ in 415 stainless steel. In comparison, these values are slightly higher than the highest value of 304 HV obtained in this study for the tempered hybrid laser-arc welds assembled at 1.2 m/min. Also, the hardness of the FZ in the tempered CA6NM hybrid laser-arc welds (Table 3-3) was determined to be considerably lower than the values of 330-340 HV reported for the FZ center in autogenous electron beam welds of CA6NM [7]; this is probably due to the low carbon filler metal (0.02% C) that was used, which, when added to the BM molten pool (0.041% C) during HLAW, would lower the C content of the FZ (estimated to be approximately 0.034%) and thereby form softer martensite.

3.3.4 Tensile strength

The ultimate tensile strength of the welds obtained at the different welding speeds after post-weld tempering are listed in Table 3-4. The average ultimate tensile strength value for all the welds was 859 MPa. Considering that the minimum ultimate tensile strength requirement in ASTM A743 standard is 755 MPa for CA6NM, the hybrid laser-arc welds in post-weld tempering condition met quite sufficiently the specification.

Table 3-4 Tensile strength and impact energy of the tempered CA6NM welds assembled at different welding speeds

	UTS (MPa)	**Failure location during tensile testing**	**Charpy impact energy (J)**
Specification values	≥ 755[I]	N/A	≥ 27[II]; ≥ 34[III]
Welding speed 0.75 m/min	843.0	BM	40.0
Welding speed 1.0 m/min	838.5	BM	41.0
Welding speed 1.2 m/min	896.5	BM	45.5

[I] ASTM A743 standard in annealed and tempered condition; [II] ASME Sect. VIII Div.1; [III] ALSTOM industrial specification.

It is also noteworthy that compared to our previously reported value for the ultimate tensile strength in the as-welded condition [3], post-weld tempering resulted in a decrease of about 100 MPa due to the reduced internal stress between the martensite laths as well as the lower dislocation density [22]. Moreover, the ultimate tensile strength of the welds in the post-weld tempering condition lies into the range of 796 - 1018 MPa (depending on the carbon content, tempering temperature and time) for a CA6NM alloy in the normalized and tempered condition [11]. To better understand the tensile deformation, longitudinal sections along the tensile load direction near the failure location were examined for the three welding speeds, as shown in Figure 7. All the tensile specimens failed in the BM but near HAZ5, as observed in Figure 3-7a-c.

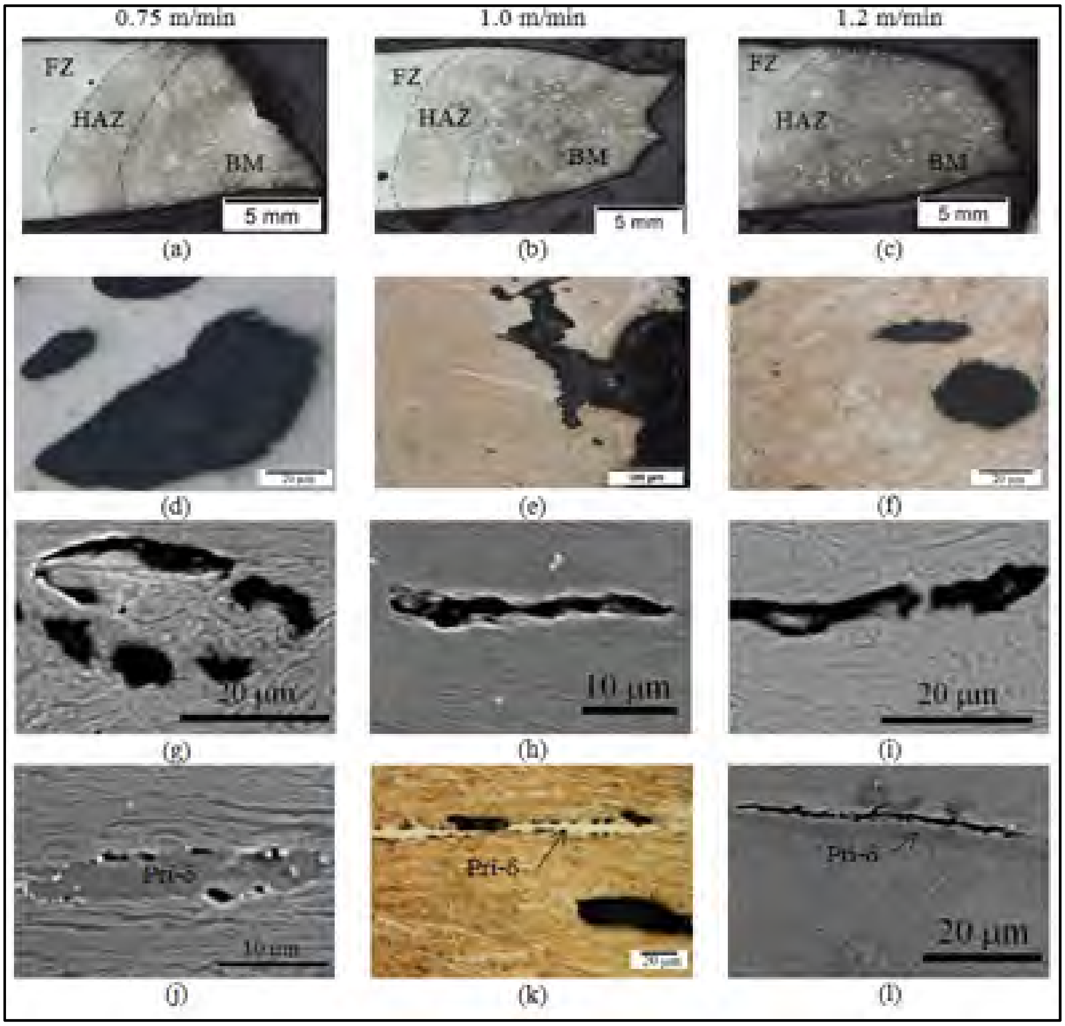
0.75 m/min
1.0 m/min
1.2 m/min
FZ
HAZ
BM
5 mm
(a)
FZ
HAZ
BM
5 mm
(b)
FZ
HAZ
BM
5 mm
(c)
(d)
(e)
(f)
20 μm
(g)
10 μm
(h)
20 μm
(i)
Pri-δ
10 μm
(j)
Pri-δ
(k)
Pri-δ
20 μm
(l)

Figure 3-7 Microstructure along the tensile load direction near the tensile fracture surface of the welds assembled at welding speeds of 0.75 m/min (a,d,g,j), 1.0 m/min (b,e,h,k) and 1.2 m/min (c,f,i,l)

A close-up observation in Figure 3-7d-f demonstrates the presence of some pores near the failure locations which are deformed and/or elongated along the tensile loading direction. The porosity area fractions measured using an image analysis method on the original cast BM and the BM of the weld near the fracture location conducted at a welding speed of 1.0 m/min are, respectively, 0.12 ± 0.04% and 0.73 ± 0.3%, which indicates a noticeable increase in both porosity area and size during the tensile deformation. The observation of larger porosities in a greater number after the tensile failure can be due to (i) the growth of some pre-existing pores in the original cast BM and (ii) formation of new pores during the tensile deformation.

The existing pores in the original BM can be gas bubbles and/or shrinkage porosity as shown in Figure 3-3a and Figure 3-8, the tensile fracture surface morphologies. Specifically, in Figure 3-8e, dendrite tips are clearly observed indicating the possible presence of shrinkage porosity in the BM. Clearly, the pre-existing porosity defects in the original cast BM can initiate tensile cracking, accelerate crack propagation, or even change the fracture path. Generally it was observed that the tensile cracks formed within the martensite matrix, i.e. between the martensite laths (Figure 3-7g-i) or at the primary delta ferrite/martensite interfaces (Figure 3-7j-l). In particular, it was found that at an early stage, multi-cracks form within the martensite matrix (Figure 3-7g-i) or at the delta ferrite/martensite interfaces (Figure 3-7j-k) and propagate, coalesce and link together into longer cracks, as shown in Figure 3-7h,i,l. The cracking mechanism within the martensite matrix is consistent with the formation of microvoids during tensile loading.

The martensite matrix displays dimple features, as shown in Figure 3-8g-i. The necking appearing near the fracture locations in Figure 3-7a-c is an indicative of the ductile failure mode, which may involve initiation, growth and coalescence of microvoids during tensile deformation. The same crack generation process has been observed for ferritic-martensitic steels [27, 28]. The differences in the localized deformation between the martensite particles or laths during tensile deformation may lead to separation of the bulk martensite or the martensite laths [29]. As for the cracks propagating at the primary delta ferrite/martensite interfaces, the poor bonding between the two phases may be responsible for the cracking. In addition, incompatibility of the plastic deformation between the primary delta ferrite and martensite phases may induce local stress concentration, that can further aid interfacial decohesion between the two phases with the crack being aligned along the tensile loading direction. Due to limited quantity of primary delta ferrite particles available, microvoid formation and growth inside the bulk martensite was predominately observed.

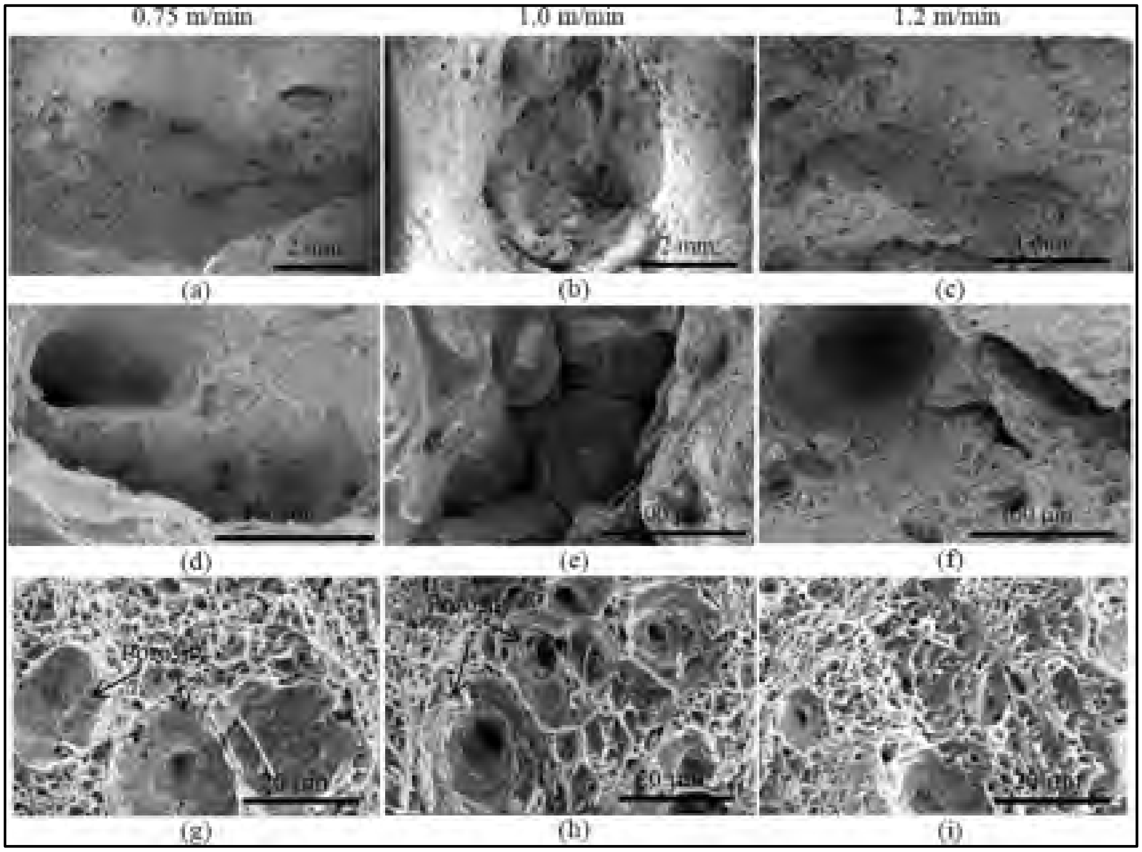

Figure 3-8 Secondary electron images of the tensile fracture surfaces for the welds assembled at welding speeds of 0.75 m/min (a,d,g), 1.0 m/min (b,e,h) and 1.2 m/min (c,f,i)

In addition, some martensite softening is possible after tempering, which leads to a more homogeneous carbon content between the two phases (primary delta ferrite and martensite). In particular, Lee et al. [30] proved through wavelength-dispersive spectroscopy that during tempering diffusion of carbon from martensite to ferrite occurs, which can increase the strength of the primary delta ferrite and the interfacial strength between the two phases. Hence the cracks formed at the primary delta ferrite/martensite interfaces propagate into the martensite matrix, rather than in the delta ferrite, as evidenced in Figure 3-7j-l.

3.3.5 Charpy impact property

The Charpy V-notch impact energies in the FZ of the welds assembled at the three different welding speeds are listed in Table 3-4 . The impact energy values increased slightly with increasing welding speed from 40.0 J at 0.75 m/min to 45.5 J at 1.2 m/min. The minimum requirement according to ASME Sect. VIII, Div.1 and industrial hydraulic turbine manufacturing specification for Charpy impact tests is 27 J and 34 J, respectively. Therefore, all welds have higher Charpy impact energies than the minimum requirement at 255 K (-18 °C). These results indicate that the recommended tempering conditions selected from ASME sec. IX are suitable for sufficiently reducing the dislocation density and internal stresses in the hybrid laser-arc welds through the tempering of martensite and formation of probably some reversed austenite. As mentioned previously, three possible phases are present in the FZ of the tempered hybrid laser-arc welds in CA6NM, namely tempered martensite, reversed austenite and delta ferrite, each of which can influence the impact energy. For instance, Iwabuchi [31] reasoned that the austenite in the vicinity of the fracture tip undergoes martensitic transformation and acts as a shock energy absorber during the impact testing. Hence, the transformation of austenite to martensite during plastic deformation (transformed induced plasticity mechanism) absorbs additional energy, thereby improving the toughness [1]. On the other hand, the presence of delta ferrite in a 13%Cr–4%Ni low carbon martensitic stainless steel can deteriorate the impact properties by decreasing the crack initiation and propagation energy and promote decohesion at delta ferrite/martensite interfaces during fracture [32].

Figure 3-9 shows the general overviews of the Charpy impact fracture surfaces for the welds assembled at the different welding speeds. The fracture surface topography of the weld assembled at 0.75 m/min exhibits a high amount of porosities in the FZ, especially close to the root (Figure 3-9a), probably due to the collapse of the unstable keyhole at this low welding speed. At the higher welding speeds (1.0-1.2 m/min), the observed porosity was lower, although some secondary cracks appeared to initiate from the porosity (Figure 3-9b,c,e,f). The fractographs indicate that the fracture mechanism seems to be a mixture of quasi-cleavage and dimple mode. For instance, the quasi-cleavage facets, as revealed in

Figure 3-9g-i, are associated with tear ridges and suggest that plastic deformation is limited during impact loading of each welding speed condition

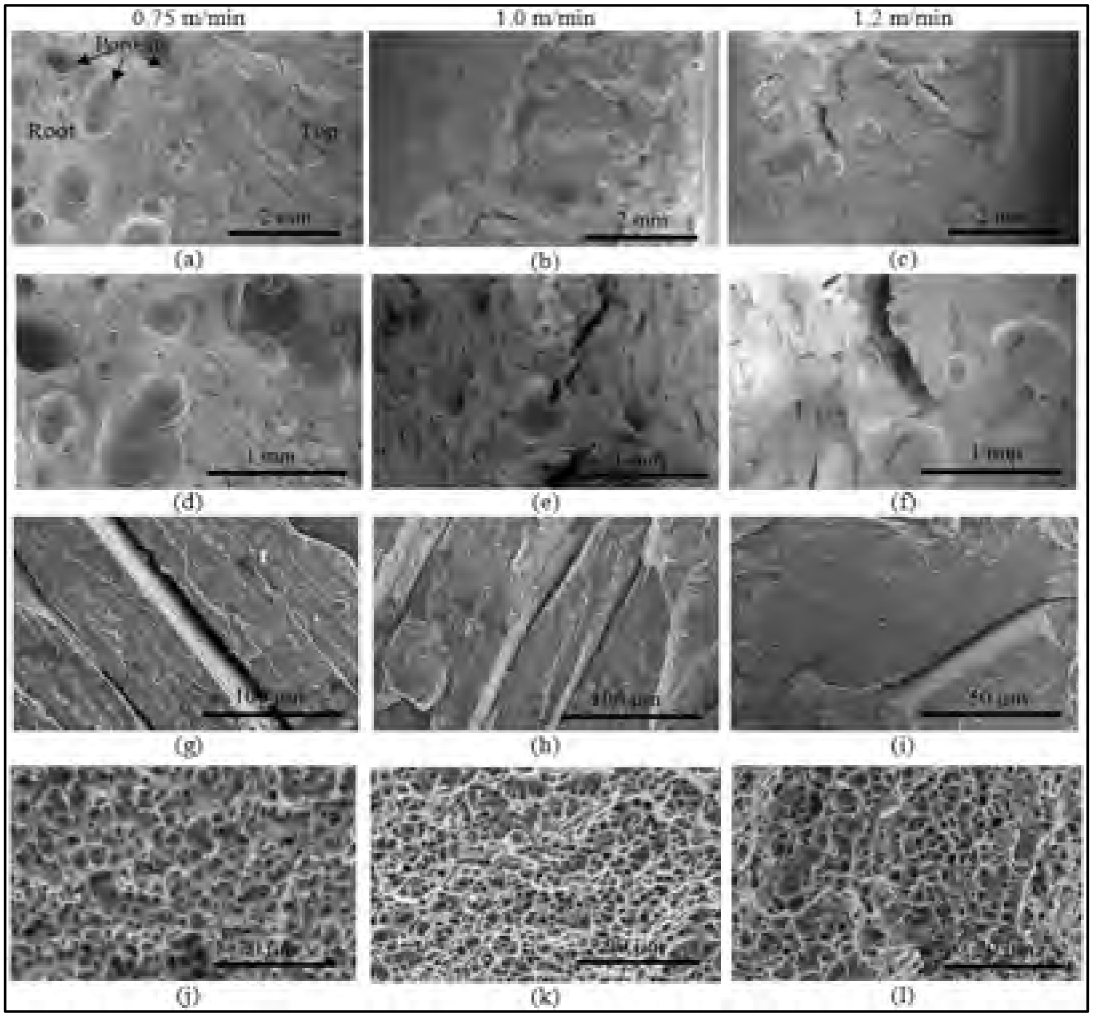
0.75 m/min
1.0 m/min
1.2 m/min
Porosity
Root
Top
2 mm
2 mm
2 mm
(a)
(b)
(c)
1 mm
1 mm
1 mm
(d)
(e)
(f)
100 μm
100 μm
50 μm
(g)
(h)
(i)
(j)
(k)
(l)

Figure 3-9 Secondary electron imaging of the Charpy impact fracture surfaces for the welds assembled at welding speeds of 0.75 m/min (a,d,g,j), 1.0 m/min (b,e,h,k) and 1.2 m/min (c,f,I,l)

In the regions associated with the prior-austenite grains, the quasi-cleavage facets were separated by secondary cracks that exhibited parallel morphologies, which have a similar spacing distance to those observed between two adjacent delta ferrite stringers in the FZ (Figure 3-4b).This observation suggests that the secondary cracks most likely propagate along the delta ferrite stringer/martensite lath interfaces during Charpy impact loading, leading to the formation of quasi-cleavage facets in the FZ. Carrouge et al. [6] also observed secondary intragranular cracks propagating along the delta ferrite/lath martensite interfaces during Charpy impact loading of low carbon supermartensitic stainless steel and indicated that, when the dispersed delta ferrite in the matrix possesses a spheroidised morphology (more analogous to the primary delta ferrite in the BM), the initiated crack could not link up and propagate as easily. It is noteworthy that the easy crack propagation along the delta ferrite/martensite interface is consistent with that appearing along primary delta ferrite plate/martensite interface in the BM during tensile loading of the hybrid laser-arc welds in this study.

By contrast, on the fractographs of each weld, the presence of equiaxed dimples, resulting from the formation and coalescence of microvoids in the matrix, are shown in Figure 3-9j-l. The fracture surfaces reveal shallower dimple morphologies for the weld assembled at 0.75 m/min as compared to the deeper dimples for the welding speed condition of 1.2 m/min. The deeper dimple morphology represents greater plastic deformation and consequently a higher absorbed energy. As Dieter et al. [33] indicated that the energy absorbed during impact loading increases with decreasing prior-austenite grain size, this can explain the slightly higher impact energy value obtained in the present study at the higher welding speed; in particular, a higher welding speed gives a faster cooling rate that can lead to a finer prior-austenite grain size and consequently finer lath martensite.

3.4 Conclusions

Hybrid laser-arc welding (HLAW) of low carbon 13% Cr-4% Ni martensitic cast stainless steel CA6NM was performed at different welding speeds in butt joint configuration. The microstructures and mechanical properties were characterized after post-weld tempering at 873 K (600 °C) for 1 hour.

1. The fusion zone in the welded CA6NM alloy in the post-weld tempered condition mainly consisted of a tempered lath martensite matrix with residual delta ferrite formed at the prior-austenite grain and sub-grain boundaries.
2. Four different heat affected zones (HAZs) were distinguishable, each exhibiting a tempered martensite microstructure after post-weld tempering. Coarse tempered lath martensite was observed in HAZ2 as compared to HAZ3, due to the higher temperatures experienced in HAZ2 (i.e. into the single phase delta ferrite region) on heating during welding. The tempered martensite in HAZ4 and HAZ5 were similar in appearance to that in the base metal under optical and scanning electron microscopy. Reversed austenite and chromium carbides also possibly formed in the HAZ during the post-weld tempering process, though not resolved using optical and scanning electron microscopy in this work.
3. The average hardness in the tempered fusion zone increased slightly with increasing welding speed from 291 ± 7 HV at 0.75 m/min to 304 ± 7 HV at 1.2 m/min, due to the refinement of the prior-austenite grains and increased dislocation density. A hardness maximum appeared in HAZ4 near the HAZ3/HAZ4 boundary while a hardness minimum was observed in HAZ5. Hardening in HAZ4 was attributed to the high temperatures experienced during welding that would lead to carbide dissolution and, in turn, carbon supersaturation of the untempered martensite; this pre-condition would result in a harder martensite on tempering. Maximum softening in HAZ5 after post-weld tempering was due to the transformation of untempered martensite to tempered martensite, the formation of reversed austenite, and the double tempering effect of the tempered martensite already existing in HAZ5.
4. The ultimate tensile strength of all the welds in the tempered condition ranged between 843 MPa and 896.5 MPa, which sufficiently meets the minimum requirement of 755 MPa according to the ASTM A743 specification. The microstructure near the tensile fracture surface and from fractography indicated dimple mode ductile features and the presence of two types of tensile cracks: (i) within the martensite matrix, i.e. between the martensite laths and (ii) at delta ferrite/martensite interfaces. The predominant cracking mechanism within the

martensite matrix is consistent with the formation, growth and coalescence of microvoids during tensile fracture in the base metal of the welds. By contrast, the delta ferrite/martensite decohesion is probably due to their poor bonding, although interfacial separation may be further aided by the local stress concentration caused by the differing plastic deformability between the delta ferrite and martensite phases.

5. The Charpy notch impact energy values of the tempered welds increased slightly from 40.5 J to 45.5 J with increasing welding speed from 0.75 m/min to 1.2 m/min; these values are well above the current minimum requirements in ASME and turbine manufacturing industrial specifications. The slightly higher impact energy at higher welding speed was attributed to the refined prior-austenite grains. Mixed dimple-quasi cleavage fracture modes were observed with secondary cracks being present along the delta ferrite/martensite interface in the fusion zone. With increasing welding speed, the dimples on the fracture surface were observed to be deeper, thereby corroborating the higher impact energy values.

Acknowledgments

The authors are grateful to Alstom, Hydro-Québec and National Science and Engineering Research Council of Canada (NSERC) for the financial supports. The authors also wish to thank E. Poirier and X. Pelletier of NRC Aerospace for their technical assistance during welding and metallographic preparation.

References

1) P. Bilmes, M. Solari., and C. Llorente: Mater. Charact., 2001, vol. 46(4), pp. 285-96.
2) Mahrle and E. Beyer: J Laser App.l, 2006, vol. 18, pp.169-80
3) F. Mirakhorli, X. Cao, X.T. Pham, P. Wanjara and J-L. Fihey: MS&T 2014 Conf., Pittsburgh, PA, USA, 2014, pp. 1891-900.
4) E. Folkhard, G. Rabensteiner and E. Perteneder: Welding metallurgy of stainless steels, Springer-Verlag Vienna, 1988, pp. 9-125.
5) D. Thibault, P. Bocher and M. Thomas: J. Mater. Process. Technol., 2009, vol. 209, pp. 2195-202.

6) D. Carrouge, H. Bhadeshia and P. Woollin: Sci. Technol. Weld. Joining., 2004, vol. 9, pp. 377-89.

7) S. Sarafan, P. Wanjara, H. Champliaud and D. Thibault: Int. J. Adv. Manuf. Technol., 2015, vol. 78, pp. 1-13.

8) S. Morito, X. Huang, T. Furuhara, T. Maki, and N. Hansen: Acta Mater., 2006, vol. 54(19), pp. 5323-31.

9) V. Vander, and F. George., Metallography, Principles and Practice, New York: ASM International, 1984, pp. 170-180.

10) Y. Song, X. Li, L. Rong, D. Ping, F. Yin, Y. Li: Mater. Lett., 2010, vol. 64(13), pp. 1411-14.

11) E.B. A. Akhiate, D. Thibault, and M. Brochu: COM 2014, Vancouver, BC, Canada, 2014.

12) M. Santella, R. Swindeman, R. Reed, and J. Tanzosh: EPRI Conference on 9Cr Materials Fabrication and Joining Technologies, 2001.

13) Y. Song, X. Li, L. Rong, Y. Li: Mater. Sci. Eng., A., 2011, vol. 528, pp. 4075-79.

14) Y. Song, D. Ping, F. Yin, X. Li, Y. Li: Mater. Sci. Eng. A., 2010, vol. 527, pp. 614-18

15) G. Krauss: Phase Transformations in Steels, Woodhead Publishing, 2012, vol. 2, pp. 126-50.

16) D.A. Porter, K.E. Easterling: Phase Transformations in Metals and Alloys, (Revised Reprint), CRC press, 1992, pp. 385-415.

17) R. Caron, G. Krauss: Metall. Trans., 1972, vol. 3, pp. 2381-89.

18) S. Kimmins, D. Gooch: Metal science, 1983, vol. 17, pp. 519-32.

19) M. De Sanctis, R. Valentini, G. Lovicu, A. Dimatteo, R. Ishak, U. Migliaccio, R. Montanari, E. Pietrangeli: Mater. Sci. Forum., 2013, vol 762, pp. 176-82.

20) B. Qin, Z. Wang, Q. Sun: Mater. Charact., 2008, vol. 59, pp. 1096-100.

21) S. Zappa, H. Svoboda, N.R. De Rissone, E. Surian, L. De Vedia: Welding Journal, 2012, vol. 91(3), pp. 83s.

22) M. Al Dawood, I. El Mahallawi, M. Abd El Azim, M. El Koussy: J. Mater. Sci. Technol., 2004, vol. 20, pp. 363-69.

23) Candelaria, C. Pinedo: J. Mater. Sci. Lett., 2003, vol. 22, pp. 1151-53.

24) J.C. Lippold and D.J. Kotecki: Welding metallurgy and weldability of stainless steels, Wiley-VCH, 2005, pp. 59-86.

25) Trudel, M. Sabourin and M. Brochu: Int. J. Fatigue, 2014, vol. 66, pp. 39-46.

26) T. Hanamura, S. Torizuka, S. Tamura, S. Enokida, H. Takechi: ISIJ international, 2013, vol. 53, pp. 2218-25.

27) G. Avramovic-Cingara, C.A. Saleh, M. Jain and D. Wilkinson: Metall. Mater. Trans. A, 2009, vol. 40, pp. 3117-27.

28) J. Kadkhodapour, A. Butz, S. Ziaei-Rad, S. Schmauder: Int. J. Plast., 2011, vol. 27, pp. 1103-25.

29) D.L. Steinbrunner, D. Matlock, G. Krauss: Metall. Trans. A, 1988, vol. 19, pp. 579-89.

30) H.S. Lee, B. Hwang, S. Lee, C.G. Lee, S.-J. Kim: Metall. Mater. Trans. A, 2004, vol. 35, pp. 2371-82.

31) Y. Iwabuchi: JSME International Journal, 2003, vol. A 46, pp. 441-46.

32) P. Wang, S. Lu, N. Xiao, D. Li, Y. Li: Mater. Sci. Eng. A, 2010, vol. 527, pp. 3210-16.

33) G.E. Dieter and D. Bacon: Mechanical metallurgy, McGraw-Hill New York, 1986, pp. 471-500.

CHAPTER 4

PHASE STRUCTURES AND MORPHOLOGIES OF TEMPERED CA6NM STAINLESS STEEL WELDED BY HYBRID LASER-ARC PROCESS

F. Mirakhorli[1,2], X. Cao[2] , X-T. Pham[1], P. Wanjara[2] and J. L. Fihey[1]

[1]École de technologie supérieure, Montréal, Québec, Canada, H3C 1K3
[2]National Research Council Canada – Aerospace, Montréal, Québec, Canada, H3T 2B2

This article is submitted to Materials Characterisation journal.

Keywords: Martensitic stainless steel; Welding; Post-weld heat treatment; Tempering; Microstructure; EBSD.

Abstract

The post-weld tempered microstructure of hybrid laser-arc welded CA6NM, a cast low carbon martensitic stainless steel, was investigated. The microstructural evolutions from the fusion zone to the base metal were characterized in detail using optical microscopy, scanning electron microscopy (SEM), electron backscatter diffraction (EBSD), X-ray diffraction (XRD) and microhardness techniques. The fusion zone, in its post-weld tempered condition, consisted of tempered lath martensite, residual delta ferrite with various morphologies, reversed austenite and chromium carbides. The reversed austenite, which can be detected through both EBSD and XRD techniques, was found to be finely dispersed along the martensite lath boundaries, particularly at triple junctions. Based on the EBSD analysis, the orientation relationship between the reversed austenite and the adjacent martensite laths seemed to follow the Kurdjumov-Sachs (K-S) model. The results also revealed the presence of the reversed austenite in the different regions of the heat affected zone after post-weld tempering. The microindentation hardness distribution was measured, and correlated to the evolution of the corresponding microstructure across the welds.

NOMENCLATURE

δ	Delta ferrite
γ	Austenite
α'	Martensite
Ac_1	Temperature at which austenite begins to form during heating
Ac_3	Temperature at which transformation of ferrite to austenite is completed during heating
Ac_4	Temperature at which austenite transforms to delta ferrite during heating
Ac_5	Temperature at which transformation of austenite to delta ferrite is completed during heating
bcc	Body centered cubic
BM	Base metal
EBSD	Electron backscatter diffraction
fcc	Face centered cubic
FE-SEM	Field emission-scanning electron microscope
FZ	Fusion zone
GMAW	Gas metal arc welding
HAZ	Heat-affected zone
HLAW	Hybrid laser-arc welding
IPF	Inverse pole figure
IQ	Image quality
K-S	Kurdjumov–Sachs
MUD	Maximal multiple of uniform distribution
ND	Normal direction
OM	Optical microscopy
OR	Orientation relationship
PAGB	Prior-γ grain boundary
PF	Pole Figure
SEM	Scanning electron microscope

SS	Stainless steel
TEM	Transmission electron microscopy
TD	Transverse direction
WD	Welding direction
XRD	X-ray diffraction

4.1 Introduction

Cast CA6NM is a low carbon 13%Cr-4%Ni martensitic stainless steel (SS), which is widely used in hydroelectric turbine runners, pump castings and ship propellers. This alloy displays several important characteristics, including improved weldability, strength and corrosion resistance compared to typical martensitic SS, such as 410 SS. The mechanical properties, such as tensile strength, elongation and impact energy values, are all strongly dependent on the low carbon lath martensite (α′) microstructure and the presence of other phases such as delta ferrite (δ), austenite (γ) and chromium carbides [1, 2]. A three-level hierarchical organization of the lath α′ structure has been proposed [3-5]. At the top of this hierarchy, the original γ grains are divided into a few packets, constituting of an aggregation of blocks that are, in turn, composed of α′ laths, as depicted in Figure 4-1.

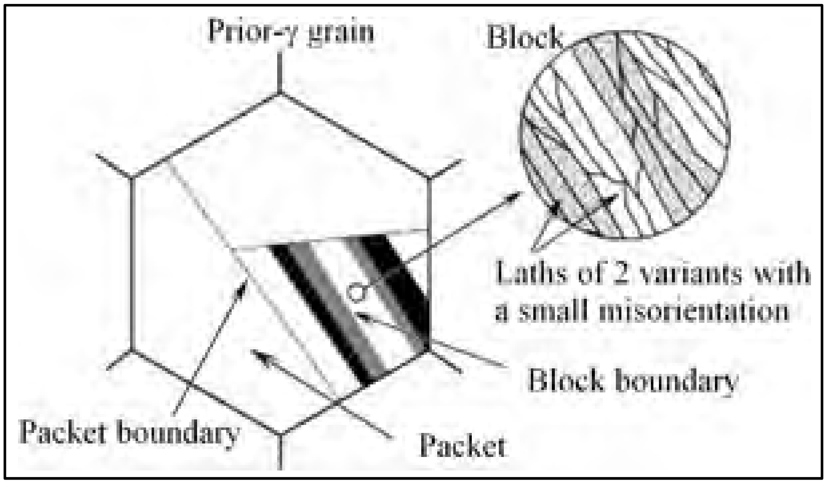

Figure 4-1 Schematic illustration showing lath α′ structure in low carbon steels [5]

When a conventional multi-pass arc welding process is used for the assembly of thick components in CA6NM, both a large fusion zone (FZ) and heat-affected zone (HAZ) are usually generated. By contrast, the hybrid laser-arc welding (HLAW) process combines the high energy density laser source with the gas metal arc welding (GMAW) process that leads to a significant reduction in the size of the FZ and HAZ. Moreover, this combination of heating sources decreases the total heat input, while maintaining high productivity [6]. Several studies have been conducted to investigate the as-welded microstructure in both the FZ and HAZ of similar materials assembled using fusion welding processes. For example, Carrouge [7] and Enerhaug et al. [8] identified four different HAZs in the weldments of super martensitic SS using arc welding process. The same nomenclatures have also been used to describe the various HAZs in low carbon martensitic SS welds assembled with GMAW [9], and recently electron beam welding [10]. The effect of the HLAW process on the microstructure and the associated mechanical properties were also investigated for 10-mm-thick CA6NM plates welded with 410NiMo filler metal [11]. In these reported work, the evolution in the microstructural constituents in the FZ and HAZ have been postulated based on the Fe-Cr-Ni equilibrium phase diagram and characterized through Optical microscopy (OM) and X-ray diffraction (XRD) analysis; but the nature of the phases was not discerned in detail, inevitably due to their inherently small size. In particular, conventional OM possesses restricted resolution and magnification, and phase detection/identification using XRD can be limited for very low volume fractions [12], depending on the incoming beam intensity and scanning speed, especially for textured polycrystalline samples. By contrast, electron backscatter diffraction (EBSD) with a Field emission-scanning electron microscope (FE-SEM) can provide quantitative microstructural information about the grain boundary orientation and characteristics, texture, crystallographic structure and phase identification using Kikuchi-pattern diffraction [13, 14]. Furthermore, the combination of EBSD and FE-SEM enable the study of large areas (as compared to transmission electron microscopy (TEM)) with high accuracy and rapid speed.

Recently, Amrei et al. [15] used the EBSD method to characterize the complex microstructure and crystallographic textures in a multi-pass CA6NM weld manufactured using flux core arc welding. For hybrid laser-arc welded CA6NM, however, the main phases, morphologies, and crystallographic textures have not been reported, although these can influence the mechanical performance of the assembly [16]. In the present work, 10-mm-thick CA6NM plates were welded using a single-pass HLAW process. The microstructural evolution in both the FZ and HAZ was investigated in the post-weld tempered condition. Phase analyses were systematically performed using OM, XRD and EBSD-SEM techniques. The morphologies and crystallography of the different phases were studied in detail and correlated to the microindentation hardness profiles.

4.2 Material and experimental procedures

The CA6NM base metal (BM) plates used in this study were 10 mm thick, 150 mm long and 75 mm wide. The chemical composition is listed in Table 4-1. The plates were sectioned from a cast turbine runner blade that had been heat-treated according to the following procedures: (1) normalizing by first heating at a rate of 60°C/hr to 800°C and holding for 8 hrs, followed by heating at a rate of 25°C/hr to 1030°C and holding for 27 hrs, (2) air cooling below the α′ finish temperature (Mf) of 90°C, and (3) tempering by heating at a rate of 36°C/hr to 640°C and holding for 27 hrs, followed by cooling at a rate of 25°C/hr to room temperature. It is worth mentioning that the tempering temperature exceeded the maximum temperature of 620°C specified by ASTM743 for CA6NM and that according to Thibault et al. [17] a tempering temperature above 630°C would result in the transformation of some of the reversed γ into untempered α′ upon cooling.

Table 4-1 Chemical composition of the CA6NM martensitic SS and ER410NiMo filler metal

Elements (Wt. %)	**Fe**	**C**	**Si**	**Mn**	**P**	**S**	**Cr**	**Ni**	**Mo**	**Cu**	**Others**
CA6NM	Bal.	0.041	0.45	0.75	0.032	0.008	13.28	4.31	0.520	0.071	0.11
410NiMo	Bal.	0.02	0.37	0.34	0.017	0.0009	12.18	4.57	0.42	0.12	-

The laser welding equipment consisted of an IPG Photonics 5.2 kW continuous wave solid-state Yb-fiber laser attached to an ABB robotic mounting arm. A collimation lens of 200 mm, a focal lens of 300 mm and a fiber diameter of 0.2 mm were employed to produce a nominal focusing spot diameter of ~0.30 mm. The defocusing distance was 2.5 mm beneath the top surface of the workpiece and the laser head was inclined 5° from the vertical position during welding. A Fronius Trans Pulse Synergic 4000 CMT (Cold Metal Transfer) GMAW power supply was used in combination with this laser system. The top surface of the workpiece was shielded using a mixture of 96% argon and 4% oxygen at a flow rate of 23.6 L/min that was fed through a GMAW nozzle, while the bottom surface was shielded using 100% argon at a flow rate of 9.5 l/min.

A single-pass HLAW process was developed to obtain full penetration for the 10-mm thick CA6NM plate using a Y-groove joint configuration. The bevel angle was ~30º. The root size was 5 mm with a gap size of ~0.2 mm. The chemical composition of the ER410NiMo filler wire (ϕ 1.14 mm) used in this process is provided in Table 1. HLAW trials were conducted at a laser power of 5.2 kW in "laser leading" mode with a welding speed of 1.0 m/min and a wire feed rate of 16 m/min. The arc current and voltage were 352 A and 30 V, respectively. Post-weld tempering was performed at a holding temperature of 600°C for 1 hr with heating and cooling rates of 50°C/hr.

After HLAW, metallographic specimens were extracted from the steady state region of the weld. Preparation for metallographic examination using Optical microscopy (OM) and XRD involved (1) hot mounting of the specimens, (2) grinding with successively finer SiC papers from 240 to 1200 grit and (3) polishing with 3, 1 and 0.5 μm diamond suspensions. For EBSD analysis, the specimen extracted from the weld was machined to have two parallel surfaces prior to metallographic preparation, as described above. Subsequently, the EBSD specimen was vibrometry-polished for 20 hrs using a 0.05 μm colloidal silica suspension, followed by electro-polishing in a solution of 65 ml $HClO_4$, 550 mL ethanol, 70 mL butyl-cellosolve, and 70 mL H_2O at 25 °C and 25 V for 15 s.

For OM imaging, the specimens were etched chemically in Beraha's reagent (1 g K2S2O5 + 20 ml HCl + 80 ml H2O) to reveal the α′ and δ in the microstructure. Alternatively, electro-etching in a 20% aqueous solution of NaOH at room temperature was used to reveal only the δ phase. The microstructures across the FZ, HAZ and BM were observed with an inverted

OM (Olympus GX71) and a Hitachi SU-70 FE-SEM. Designed to perform ultra-high resolution imaging, this FE-SEM was equipped with EBSD capability and Channel 5 software. The EBSD studies were performed at an accelerating voltage of 20 kV with the specimen tilted at 70° relative to normal incidence of the electron beam in order to generate diffraction Kikuchi patterns of sufficient intensity. Two different increments of either 1 μm or 0.02 μm were used for EBSD scanning and a noise reduction algorithm was also applied for all the images to remove indexing errors and uncertainty coming from artifacts or pitting (due to electropolishing). The γ phase in the FZ and BM was identified by means of a Panalytical XRD with a Cu-Kα radiation (wavelength of 0.15418 nm) at 40 mA and 45 kV via microdiffraction. The diffraction angle (2θ), at which the X-rays impinged the specimen, varied from 30° to 130° by increments of 0.017° with a pause of 100 seconds in each step. Quantification of the γ fraction was performed using a direct method, as described in [18]. The Vickers microhardness was measured using a Struers DuraScan machine equipped with a motorized X-Y stage and a fully automated testing cycle (i.e. stage movement, loading, focusing and measurement). Vickers microhardness mapping across the entire transverse section of the weld was carried out using the ecos WorkflowTM software module with uniformly distributed test points at a line interval of 0.5 mm (for mapping), a load of 200 g, an indentation spacing of 0.2 mm and a dwell time of 15 seconds. Two-dimensional image mapping of the hardness distribution on the surface of the weld was then generated using the areaMASTER function in the ecos WorkflowTM software module.

4.3 Results and discussion

The transverse section of a fully penetrated joint assembled at a laser power of 5.2 kW and a welding speed of 1.0 m/min is shown in Figure 4-2a. The macrostructures of the different HAZs near the fusion boundary are shown in Figure 4-2b in correlation with the cooling path for a 13% Cr and 4% Ni pseudo-binary section of the Fe-Cr-Ni equilibrium ternary phase diagram [19], which is very similar to the chemistry of the CA6NM alloy. Based on this phase diagram, five different HAZs can be predicted in the as-welded condition, although the first high temperature HAZ (HAZ1) is usually undistinguishable from the fusion boundary. The other four HAZs (HAZs 2-5), after post-weld tempering treatment, can be identified according to their microhardness profile [11, 20]. The microstructural evolutions in these HAZs and the FZ are the central topic of the present work, as discussed below.

4.3.1 Base metal

The microstructure of the BM after the post-weld tempering treatment is illustrated in Figure 4-3a. The BM in the double-tempered condition consisted of fully tempered lath α′ with plate-like primary δ dispersed in the α′ matrix, which were apparent under OM, and reversed γ that was quantifiable using XRD

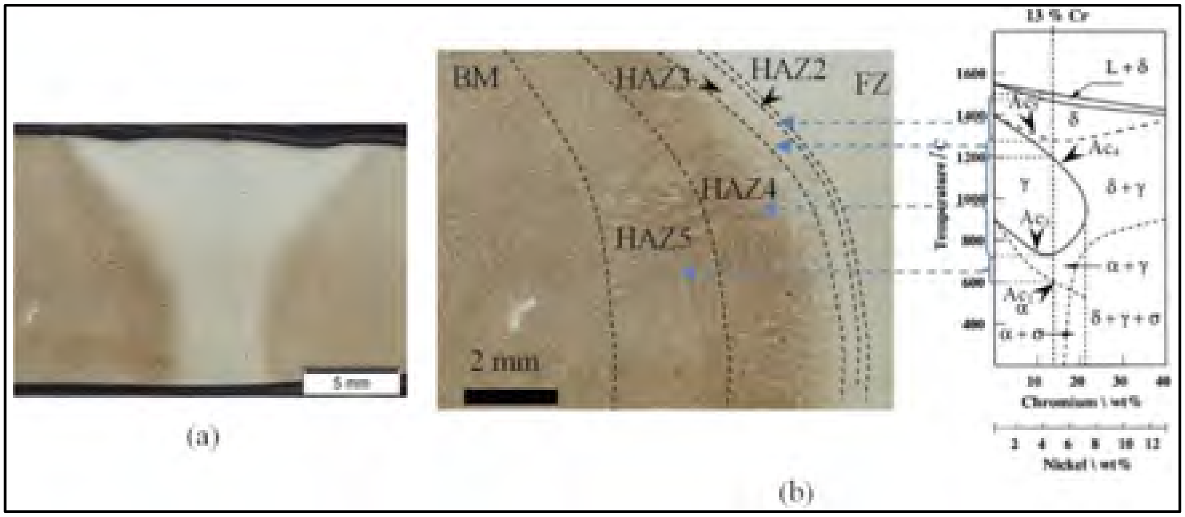
5 mm
(a)
BM
HAZ3
HAZ2
FZ
HAZ4
HAZ5
2 mm
13 % Cr
L + δ
Ac₄
δ
Ac₅
γ
δ + γ
Ac₃
α + γ
Ac₁
α
δ + γ + σ
α + σ
Temperature / °C
1600
1400
1200
1000
800
600
400
10
20
30
40
Chromium \ wt%
2
4
6
8
10
12
Nickel \ wt%
(b)

Figure 4-2 (a) Transverse section of a welded joint obtained at a welding speed of 1.0 m/min, and (b) macrostructure from the FZ to the BM according to the 4% Ni pseudobinary section of the Fe-Cr-Ni ternary phase diagram [19]

For each of the α′ and γ phases, five and four different peak intensities were detected, respectively (Figure 4-3b), and the reversed γ fraction in the BM was measured to be approximately 15%.

4.3.2 Fusion zone

The FZ microstructure in the post-weld tempered condition under the OM is shown in Figure 4-4a. It consisted of predominately tempered lath α′. Two different locations (positions I and

II in Figure 4-4a), one (I) near the FZ center and the other (II) close to the FZ boundary, were examined using the EBSD method. Their respective image quality (IQ) maps are presented in Figure 4-4b and Figure 4-4c. The IQ map reflects the quality of the Kikuchi lines for each location. Achieving a clear Kikuchi-line diffraction in the lath α′ structure is difficult, due to the high density of the lattice defects, such as dislocations. The IQ maps of the present EBSD analysis indicate reasonably good quality. Figure 4-4a also shows the scan position with respect to the weldment where ND, TD and WD refer to the normal, transverse and longitudinal welding directions, respectively. Figure 4-4d and Figure 4-4e display the inverse pole figure (IPF) orientation maps relative to the ND obtained from the FE-SEM/EBSD measurements respectively in the center and at the boundary of the FZ and the relationship between the IPF colors and the crystallographic orientations is displayed in a stereographic triangle. The black boundaries in the IPF orientation maps (Figure 4-4d-e) delimit misorientation of the adjacent points greater than 15° at their interfaces, and are attributed predominantly to the prior-γ grain boundaries (PAGBs) and packet boundaries. However, due to the high density of the boundaries at this low magnification, it was difficult to precisely differentiate the PAGBs and packet boundaries from each other in the IPF orientation maps (Figure 4-4d-e), especially since this is even more difficult when the lath α′ structure in the FZ is examined.

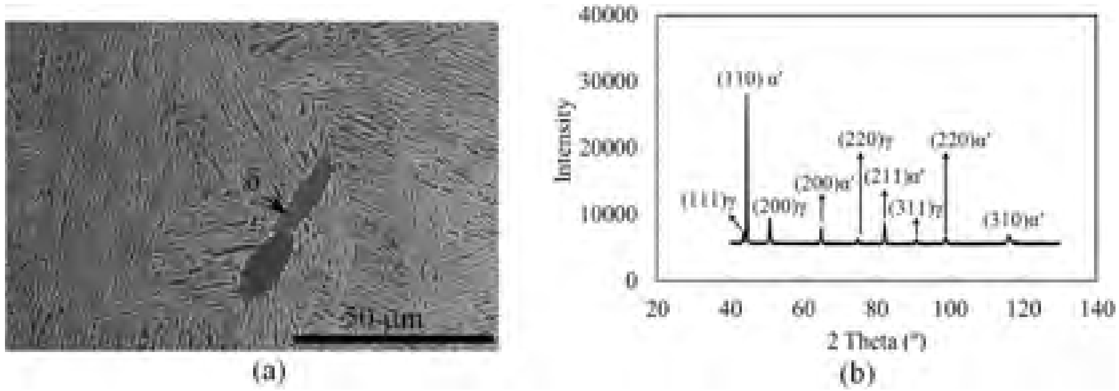

(a)

(b)

Figure 4-3 BM characteristics (a) SEM image and (b) XRD spectrum

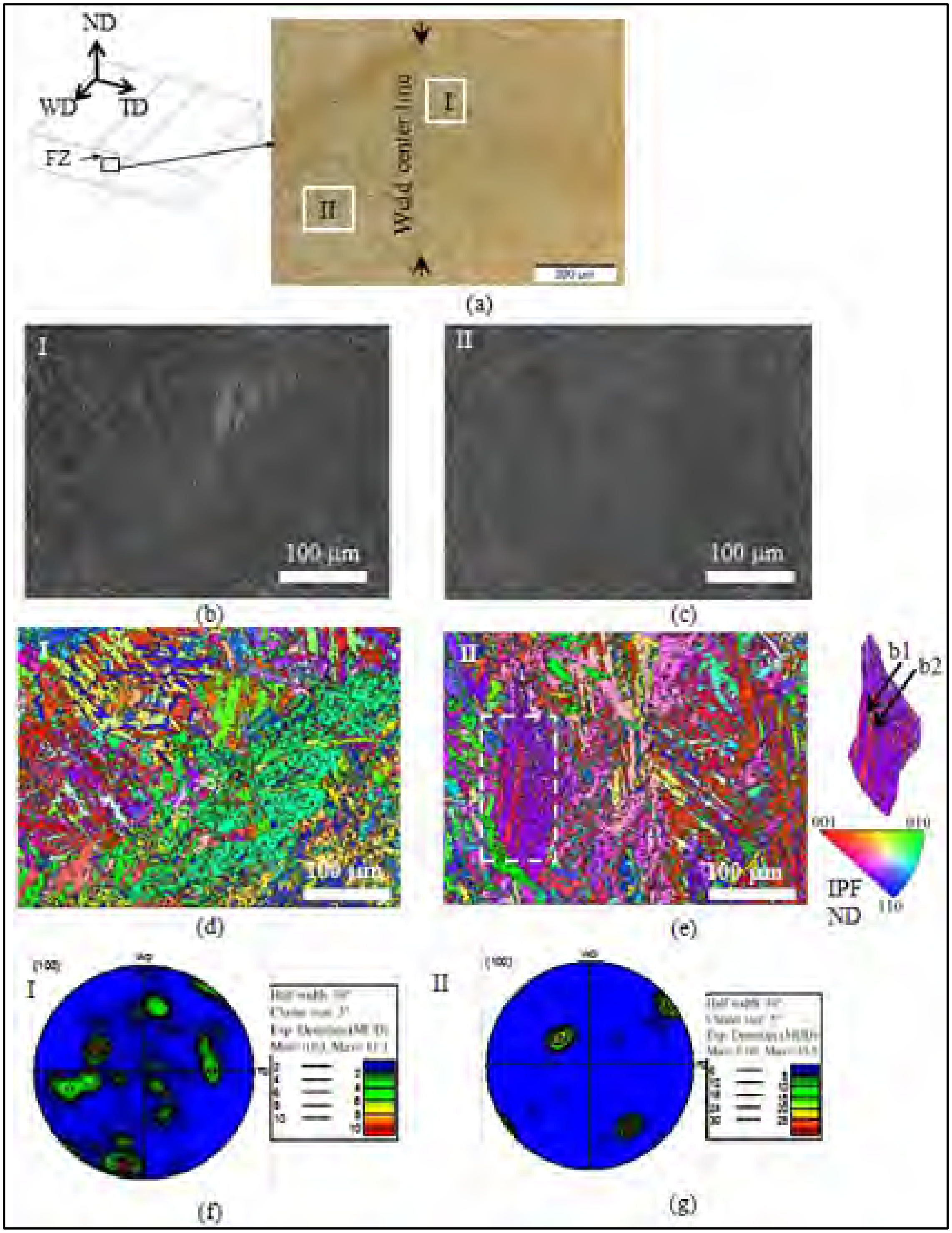
ND
WD
TD
FZ
Weld center line
I
II
200 µm
(a)
I
100 µm
(b)
II
100 µm
(c)
I
100 µm
(d)
II
100 µm
(e)
b1
b2
001
010
110
IPF
ND
I
(100)
WD
TD
(f)
II
(100)
WD
TD
(g)

Figure 4-4 (a) FZ macrostructure with the weld centerline demarcated by the two arrows, (b,c) EBSD IQ map at positions I and II, (d,e) IPF orientation map at positions I and II (b1 and b2 refer to two diferent blocks), and (f,g) PF at positions I and II

However, the packets containing blocks with alternating dark and light contrast in the IQ images (Figure 4-4b-c) and different orientations in the IPF images (Figure 4-4d-e) were well detected. A packet extracted in Figure 4-4e, and two kinds of blocks with different crystallographic orientations are delineated, as indicated by arrows b1 and b2. The packets and blocks within the PAGBs varied significantly in size, shape and orientation. The orientation distributions of the lath α′ structure in a small area (~412 μm × 320 μm) map close to the FZ center (Figure 4-4d, related to location I in Figure 4-4a) and boundary (Figure 4-4e, related to location II in Figure 4-4a) are shown in the pole figures (PFs) of Figure 4-4f and Figure 4-4g, respectively.

The PFs present the orientation relationship of the (001)-plane in the lath α′ structure relative to WD and TD axes. The (001)-PF pattern in the center of the FZ revealed that the lath α′ structure in the FZ center (Figure 4-4g) has less crystallographic texture compared to the FZ boundary (Figure 4-4f), since the maximal multiple of uniform distribution (MUD) factor near the FZ boundary of 32.5 is approximately three times higher than that near the FZ center of 11.1. To observe and distinguish the PAGBs, the packets and blocks boundaries, as well as the misorientation angles between them in the FZ, an EBSD analysis was performed at higher magnification in Figure 4-5a and in a smaller area of 105 μm × 80 μm.

The IPF orientation color and misorientation maps corresponding to Figure 4-5a are displayed in Figure 4-5b and Figure 4-5c, respectively. The solid and dashed lines in Figure 4-5b indicate the PAGBs and packet boundaries, respectively. The misorientation angles between the PAGBs, packets and blocks, were revealed and quantified in Figure 4-5c and Figure 4-5d, respectively. The green lines in Figure 4-5c indicate a misorientation smaller than 10° but greater than 2°, which is mostly related to the block boundaries. The black lines show misorientations greater than 10°, which corresponds to PAGBs and packet boundaries. The majority of prior-γ and packet boundary misorientation angles lie within the range of 60° to 85° according to the misorientation intensity graphs in Figure 4-5d. Some 60°-twinning misorientations were also observed, as indicated by the red lines in Figure 4-5c. It is worth noting that the yield strength of lath α′ has an inverse relationship with the packet and block size, and that, in addition, the high angle boundaries between the blocks and packets can act as a barrier to dislocation movement during deformation of the lath α′, thus increasing the yield strength of the material [16].

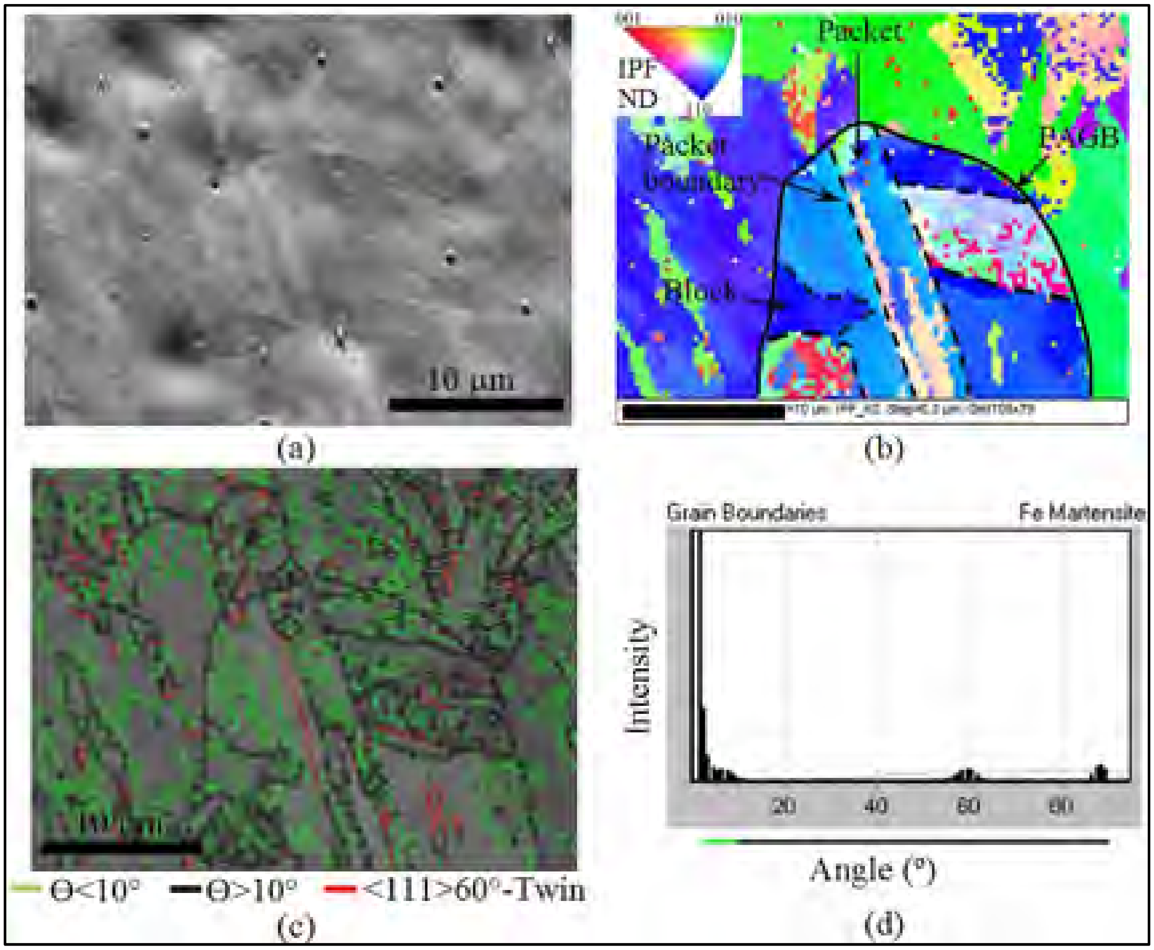
10 µm
(a)
001
101
IPF
ND
111
Packet
PAGB
Packet boundary
Block
(b)
Θ<10°
Θ>10°
<111>60°-Twin
(c)
Grain Boundaries
Fe Martensite
Intensity
20
40
60
80
Angle (°)
(d)

Figure 4-5 (a) High magnification SEM image in FZ, (b) IPF orientation map, (c-d) misorientation map and angles between the adjacent points and their distribution, related to (a)

In addition to the tempered lath α′, δ was also observed in the FZ (Figure 4-6). This phase partially remained in the FZ microstructure after the cooling cycle of the welding process. The low magnification OM images of the FZ, taken from transverse (Figure 4-6a) and horizontal (top view) (Figure 4-6f) cross-sections, displayed stringers of δ dispersed throughout the FZ with different morphologies. In particular, four different δ morphologies or patterns were predominately observed in the FZ at higher magnifications, both at transverse (Figure 4-6b-e) and horizontal (Figure 4-6g-j) sections, and will be discussed here after in more detail. Three of these morphologies, observed both in transverse (Figure 4-6b,c,d) and horizontal (Figure 4-6g,h,i) sections, revealed a repetitive pattern, and each of them seems to follow a common crystallographic orientation direction. These morphologies (Figure 4-6b-d and Figure 4-6g-i) are created by the incomplete growth of the Widmanstätten γ grains during the solid-state δ → γ phase transformation, leaving at their boundaries (prior-Widmanstätten γ grain boundaries) the remaining δ stringers delineating the growth front, which resembles the original orientation of the former Widmanstätten γ in the final microstructure. Thus, the specific residual δ morphology, detected in Figure 4-6b-d (transverse section) and Figure 4-6g-i (horizontal section), can be explained by the fact that the Widmanstätten γ plates tend to align parallel to themselves and form along a specific direction [21]. Several studies have been performed on the crystallographic orientation direction between prior-γ and δ in duplex [22] and austenitic SS [23], which revealed the orientation relationship close to Kurdjumov–Sachs (K-S) between δ and γ for both austenitic and duplex SS. However the δ/γ crystallographic orientation in martensitic SS has not been reported, to best as far as knowledge of the authors have known.

Upon further cooling, the γ transforms to α′ but some δ remains in the final microstructure, as shown in Figure 4-6. During post-weld tempering (~600°C), the δ in the FZ does not undergo noticeable changes. The evidence of a former Widmanstätten γ structure and residual δ within the PAGBs was also observed previously by Carrouge [7] and Thibault et al. [9] in the FZ of super martensitic and low carbon martensitic SS welds, respectively. The parallel and continuous networks of residual δ between prior-Widmanstätten γ plates, observed in Figure 4-6b and Figure 4-6g, indicate that the Widmanstätten plates have maintained a planar interface within the δ as solid state transformation proceeds. In Figure 4-6c-d and Figure 4-6h-i, it is observed that the parallel lines are broken in such a way that the repetitive pattern of the morphology is preserved. This instability at the Widmanstätten γ interface during the δ to γ transformation was also reported by Leone et al. [21] in Fe-Cr-Ni SS, and it was explained by the fact that the initial planar interface becomes unstable as the δ→γ transformation proceeds.

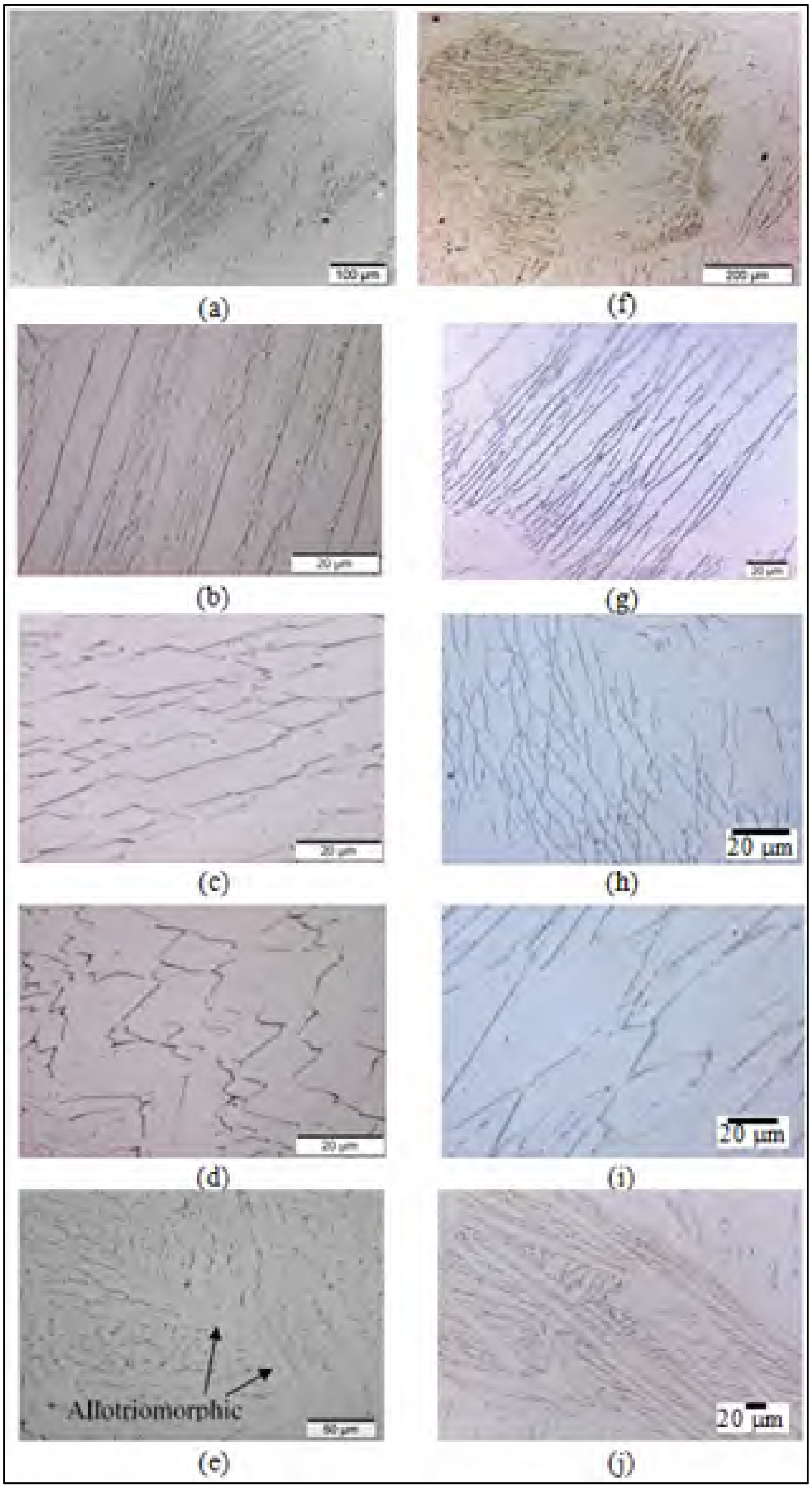
100 µm
200 µm
20 µm
20 µm
20 µm
20 µm
20 µm
20 µm
Allotriomorphic
50 µm
20 µm

(a) (f) (b) (g) (c) (h) (d) (i) (e) (j)

Figure 4-6 Different δ morphologies in the horizontal (top) view (a-e) and transverse sections (e-i)

Owing to the diffusional nature of this transformation, the γ/δ interface tends to break down to accelerate the interface growth rate. Another δ morphology observed in the FZ of CA6NM, shown in Figure 4-6e and Figure 4-6j, is analogous to the former allotriomorphic γ microstructure. This morphology is inherited from the incomplete growth of allotriomorphic γ grains in which δ remains along the prior-allotriomorphic γ grain boundaries. In general, the γ formed at high temperatures predominately with Widmanstätten and allotriomorphic morphologies during HLAW of CA6NM, thus the residual δ along PAGBs shows Widmanstätten and allotriomorphic morphologies.

Reversed γ was another phase observed in the FZ in its post-weld tempered condition (Fig. 7). The high magnification scanning electron microscope (SEM) micrographs in Figure 4-7a-b show that the reversed γ was formed along the α′ lath and interlath boundaries, preferentially at triple junctions of lathes (as demarcated in Figure 4-7a-b), due to higher interfacial free energy. The reversed γ fraction in the FZ, estimated to be approximately 7.5%, was quantifiable through XRD, as illustrated by the spectrum in Figure 4-7c.

In addition to XRD analysis, a color coded EBSD phase map was also generated in the FZ (Figure 4-8) to identify the different phases. It is noteworthy that phase detection in EBSD is based on the crystallographic structure of the phases, in such a way that the crystallographic information obtained from the diffraction patterns is compared with the patterns of the predictable phases in the material, and thus the most corresponding phases are identified.

Figure 4-8b shows an EBSD phase map in which the red colored matrix corresponds to lath α′, the blue color indicates reversed γ and the green and yellow colors are related to chromium carbide (i.e. M_7C_3) in ortho-rhombic and hexagonal crystallographic structures, respectively. The reversed γ was detected mainly at triple junctions of the lathes, as well as along and within the α′ laths, which is consistent with the results presented in Figure 4-7a-b. The formation of reversed γ along and inside the α′ laths was reported previously in tempered low carbon martensitic SS using the TEM method [24]. Beside α′ and reversed γ, chromium carbides in the form of M_7C_3 were also detected (Figure 4-8b). Although, the chromium carbides were not distinguished clearly on the SEM images, they could be detected by the

EBSD phase analysis, since the EBSD scans were undertaken with a 20-nm step size to cover all possible nanometer-size phases.

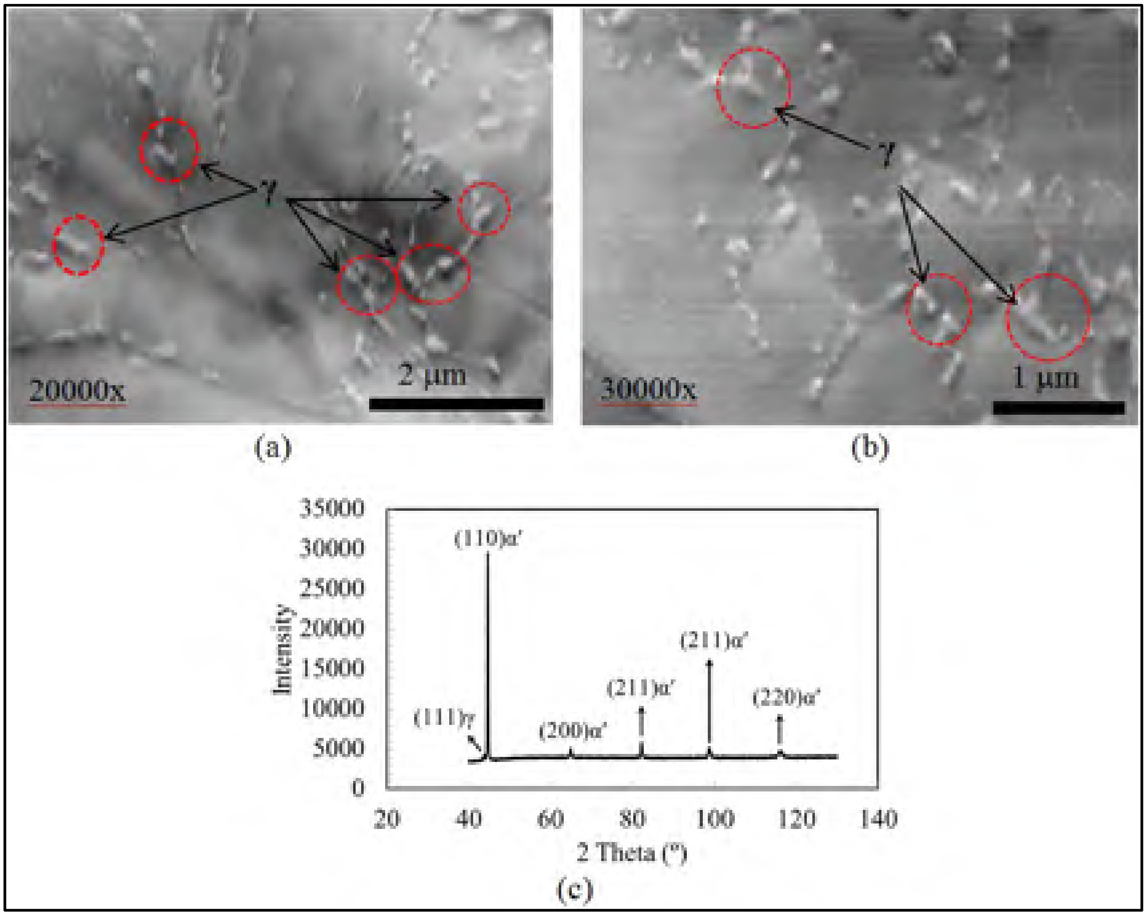

Figure 4-7 (a,b) Reversed austenite in FZ and (c) XRD spectrum

Chromium carbide forming after single-stage tempering of low carbon Fe–13%Cr–4%Ni–Mo martensitic SS has already been reported predominately in the form of $M_{23}C_6$ [1]. The formation of $M_{23}C_6$ during post-weld tempering of the CA6NM is also possible, but could not be identified using the EBSD phase mapping analysis, since phase identification in EBSD is based on crystallographic information and $M_{23}C_6$ has a similar crystallographic structure to the α′. Therefore, the EBSD phase analysis could not differentiate $M_{23}C_6$ carbides from α′. In general, the precipitation of chromium carbides has been reported to occur with the sequence of M_3C, followed by M_7C_3 and then $M_{23}C_6$ in martensitic SS and low carbon martensitic SS, depending on the time and temperature [19]. However, additional microstructural investigation (e.g. TEM) would be needed to identify the entire carbide complex formed in this material during tempering. Figure 4-8c displays the orientation relationship (OR) between the parent fcc γ and product bcc α′ phases – in the same area as shown in Figure 4-8b – in which only the phase boundaries between the reversed γ and the matrix (α′) are displayed.

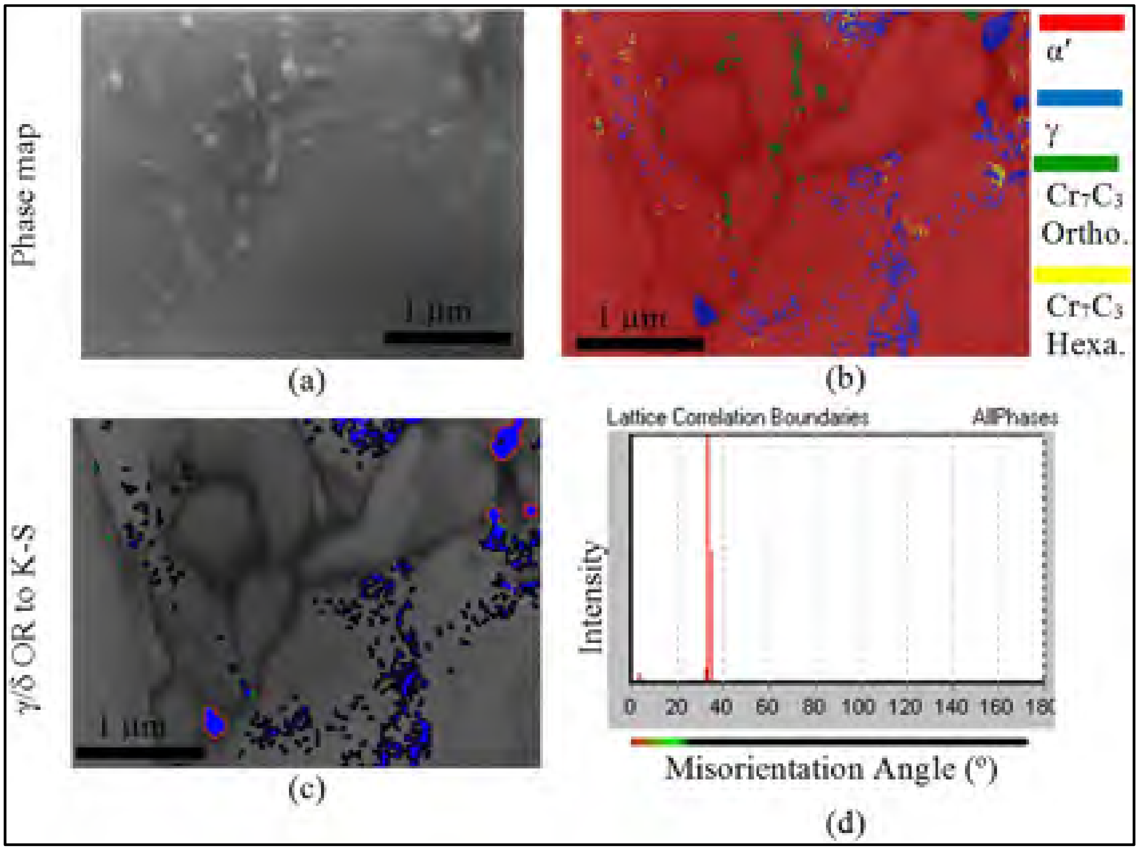

Figure 4-8 SEM image in FZ (a) and its corresponding EBSD phase map (b), (c-d) γ/α′ OR between α′ and reversed γ within the FZ

It is noteworthy that the γ→ α′ phase transformation is characterised by a specific crystallographic orientation relationship, which is based on certain crystallographic planes and directions. It has been found by Kitahara et al. [4] that the OR between lath α′ and γ for different low carbon martensitic steels is close to the K–S OR, which is expressed as $(111)_{\gamma}//(011)_{\alpha'}$, $[\bar{1}01]_{\gamma}//[\bar{1}\bar{1}1]_{\alpha'}$ between γ and α′. In this research it was also assumed that the K-S relationship exists between γ and α′ and the deviation from the ideal K–S relationship was measured between the reversed γ and α′, as displayed in Figure 4-8c-d and is delineated by the red (less than 5°), green (between 5° to 20°) and black (more than 20°) boundaries. From this present analysis, the orientation between reversed γ and α′ was found to be close to the K-S relationship, especially for γ at triple junctions with deviations less than ~5°. For the reversed γ formed within the laths, the relationship exhibited a deviation of ~35° from the K-S relationship.

4.3.3 Heat affected zone microstructure

The microstructures in the different HAZs after post-weld tempering treatment are shown in Figure 4-2. HAZ1 refers to a partially melted zone, which involves heating into the L + δ region during the weld thermal cycle, and could not be distinguished from the FZ in the CA6NM welded by the HLAW process, as mentioned previously by the authors [20]. The remaining four HAZs can be categorized into two main groups of high temperature HAZs (HAZ2 and HAZ3) and low temperature HAZs (HAZ4 and HAZ5). HAZ2 and HAZ3 are respectively referred to as the single phase δ and dual phase δ + γ regions in the phase diagram (Figure 4-2).

After the post-weld tempering treatment, the high temperature HAZs consisted of tempered lath α′ under OM, with the main difference being the coarser grain structure in HAZ2 (Figure 4-9a) relative to HAZ3 (Figure 4-9c). The grain coarsening in HAZ2 is due to the high temperatures experienced, which resulted in complete transformation of the BM microstructure in this region to δ on heating (above Ac_5 in the phase diagram) during welding. At these high temperatures, the δ grains grow rapidly during heating and then, upon cooling, re-transform to γ followed by a coarse α′ structure. Some fine reversed γ, formed after the post-weld tempering treatment, was also observed in HAZ2 (Figure 4-9b) and HAZ3 (Figure 4-9d) under high magnification SEM. The fine reversed γ films were formed predominately along the α′ laths boundaries. The width of the reversed γ films were less than 100 nm in HAZ2 and less than 150 nm in HAZ3.

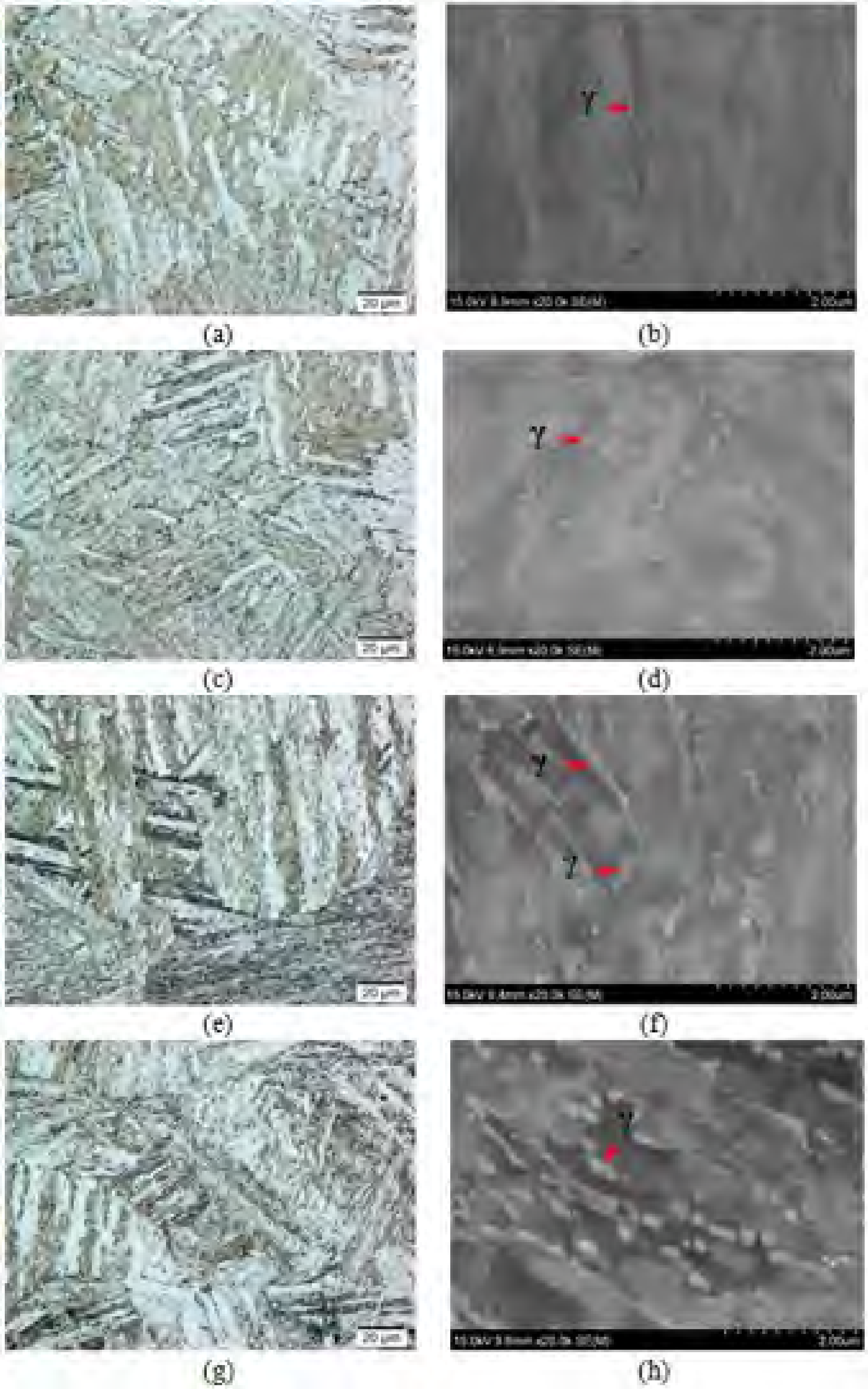
20 μm
γ
2.00μm
(a)
(b)
20 μm
γ
2.00μm
(c)
(d)
20 μm
γ
γ
2.00μm
(e)
(f)
20 μm
γ
2.00μm
(g)
(h)

Figure 4-9 Microstructural evolution in various HAZs. (a-b) HAZ2, (c-d) HAZ3, (e-f) HAZ4, (g-h) HAZ5

Heated to temperatures between Ac_3 and Ac_4 during welding, HAZ4 (Figure 4-9e) – that refers to as the single phase γ region in the phase diagram (Figure 4-2) – was observed under OM to consist of tempered lath α′ after post-weld tempering. Reversed γ was observed along the α′ lath boundaries and at triple junctions as well (Figure 4-9f). The width of the reversed γ films in this region was between ~150 nm and 200 nm. A coarsening of the reversed γ along the α′ laths was observed in HAZ4, relative to HAZ2 and HAZ3.

The low temperature dual phase α' + γ region, termed as HAZ5, refers to as the region that has been heated to temperatures between Ac_1 and Ac_3 (Figure 4-2) during the weld thermal cycle. After post-weld tempering, OM observations of HAZ5 revealed tempered lath α′ (Figure 4-9g), which is similar to that observed in HAZ4. High magnification SEM images presented in Figure 4-9h and Figure 4-10a demonstrate that a higher fraction of reversed γ along lath α′ formed in HAZ5 compared to the other HAZs, especially at triple lath junctions. The widths of the reversed γ film were measured to be in the range of ~150 nm to 250 nm.

EBSD color coded phase mapping was also performed in HAZ5 (Figure 4-10), and M_7C_3 chromium carbides with hexagonal and ortho-rhombic crystallographic structures were detected at the lath boundaries close to the reversed γ and also within the lath α′. The OR between the reversed γ and α' matrix in HAZ5 is shown in Figure 4-10c-d and is more compatible to the K-S relationship with less than 5° misorientation, especially for the reversed γ formed along the lath boundaries or at triple junctions of the lath boundaries (as demarcated by the arrows in Figure 4-10c)

The coarsening of the reversed γ films in HAZ5 compared to HAZ2-4, was due to the fact that this zone experienced partial transformation from α' to γ during the weld heating cycle, which is also comparable to the tempering temperature range for CA6NM. This could lead to the formation of retained γ during the weld cooling cycle. During post-weld tempering, therefore, the retained γ can either act as a nucleation site for reversed γ [25] or grow during the tempering process In general, the untempered α′ microstructure from the FZ to the HAZs, which was a predominant microstructure in the as-welded condition, underwent specific microstructural changes during post-weld tempering. Since untempered α′ is an unstable microstructure, it possesses the inherent supersaturated structure with carbon and a high dislocation density; during tempering, these factors can act as a driving force to initiate transformations in the α′ matrix, including the formation of carbides, rearrangement of carbon atoms, high angle inter-lath boundaries and the formation of reversed γ, which lead to greater stability of the tempered α′ [26].

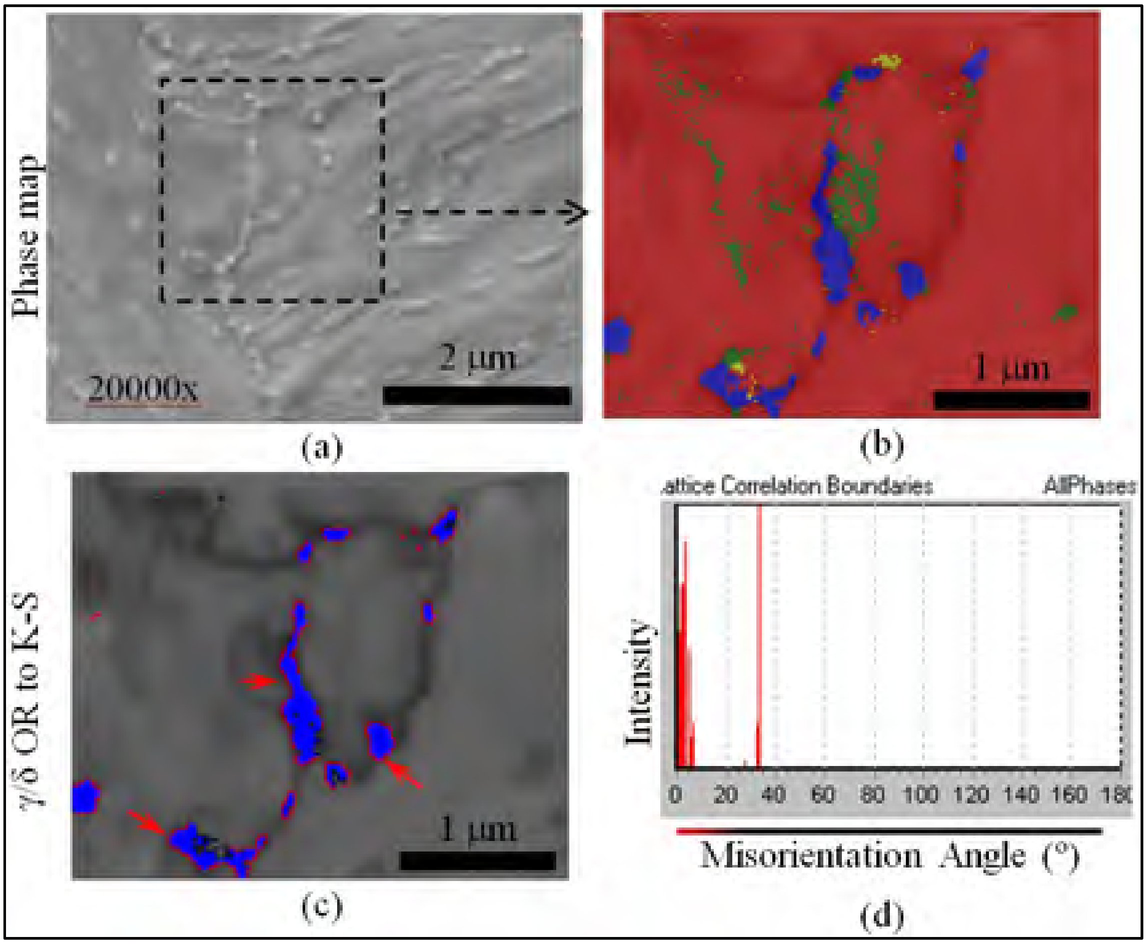
Phase map
20000x
2 μm
(a)
1 μm
(b)
γ/δ OR to K-S
1 μm
(c)
attice Correlation Boundaries
AllPhases
Intensity
0
20
40
60
80
100
120
140
160
18
Misorientation Angle (°)
(d)

Figure 4-10 SEM image in HAZ5 (a) and its corresponding EBSD phase (b), (c-d) γ/α′ OR between α′ and reversed γ in HAZ5

As discussed previously, during the weld thermal cycles, the α′, γ and carbides in the different HAZs experienced various microstructural changes. Primary δ, another phase presented in the as-received BM may also experience specific transformation during the weld heating cycle in the different HAZs. Since δ is not a thermodynamically stable phase in the microstructure, it can dissolve at and above the austenitizing temperature (Ac_3) according to the phase diagram (Figure 4-2).

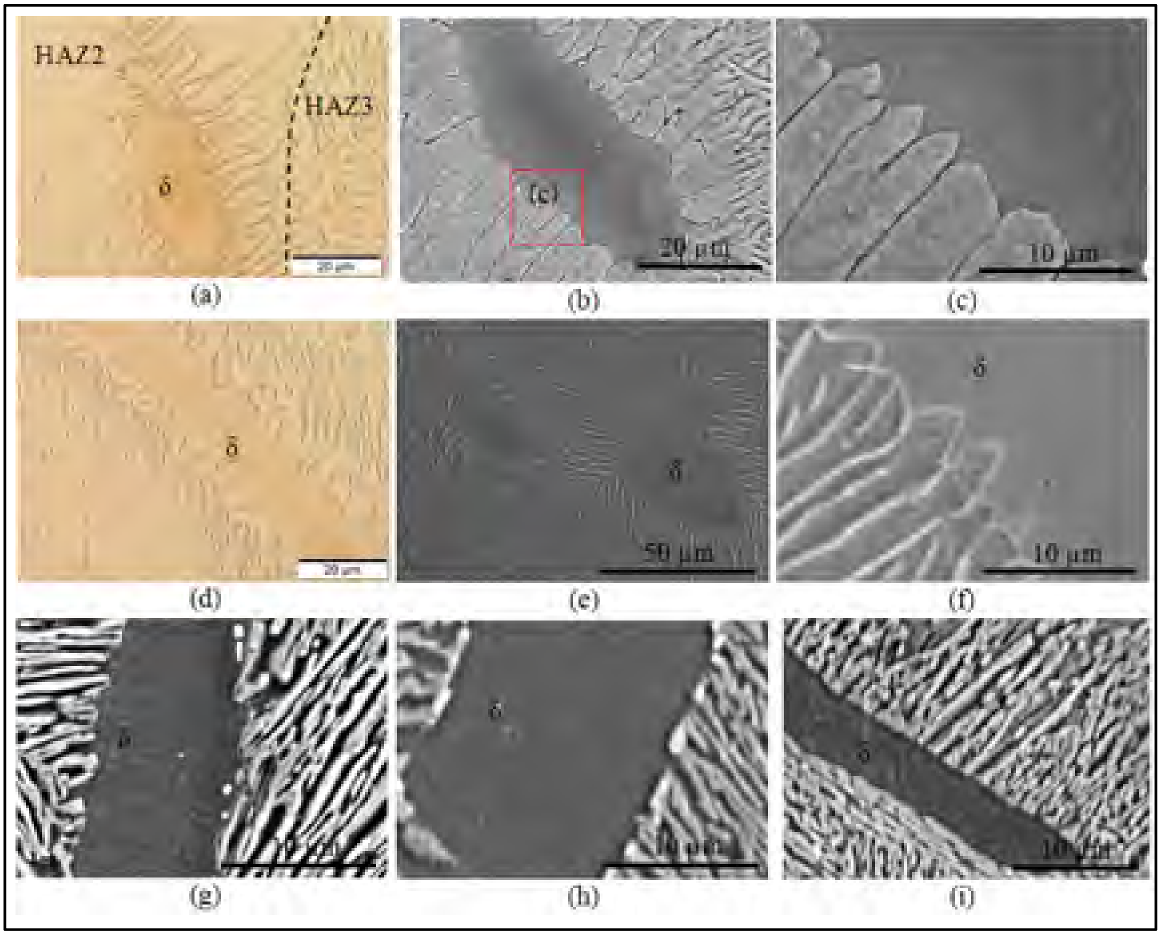
HAZ2
HAZ3
δ
20 μm
(a)
(c)
20 μm
(b)
10 μm
(c)
δ
20 μm
(d)
δ
50 μm
(e)
δ
10 μm
(f)
δ
10 μm
(g)
δ
10 μm
(h)
δ
10 μm
(i)

Figure 4-11 Primary δ in (a-c) HAZ2, (d-f) HAZ3, (g) HAZ4, (h) HAZ5, and (i) BM

However, considerable dissolution of primary δ (already existing in the BM) cannot occur here, owing to the high heating rate and short holding time at high temperature during HLAW. The plate-shaped primary δ in HAZ2, after welding, is shown to still be present in the OM and SEM images illustrated in Figure 4-11a and Figure 4-11b, respectively, which reveals an instability in primary δ/γ interfaces after the heating to the high temperature single phase δ region compared to the primary δ in the BM (Figure 4-11i). The interface shows columnar-shaped morphology. A higher magnification of the primary δ/γ interfaces in Figure 4-11b is shown in Figure 4-11c. The same interface morphology for plate-like primary δ was observed in HAZ3 after welding (Figure 4-11d-f). In HAZ2 and HAZ3, according to the phase diagram (Figure 4-2), the primary δ, which already exists in the BM, is rapidly heated to a high temperature. When the transformation from δ to γ takes place on cooling, the change in interface morphology of primary δ/γ occurs. This morphological change in primary δ/γ interface from a planar front (observed in BM) to columnar – observed in HAZ2 and HAZ3 – occurs during the incomplete dissolution of primary δ due to the short heating time and fast cooling during welding, which leads to a change from a planar to a cellular interface morphology. A similar interface change at primary δ/γ interface has been observed in Fe-Ni alloys and analysed through in-situ observation at high temperatures by Vandyouseffi et al. [27] and Arai et al. [28]; their findings showed that the change in interface morphology of the primary δ/γ is due to the diffusion control solid-state phase transformation from the primary δ to γ, and that the higher diffusion of Ni in δ than in γ results in an instability of the primary δ/γ interface and cellular growth. No significant changes were observed in the δ interface morphology with prior-γ in HAZ4 (Figure 4-11g) and HAZ5 (Figure 4-11h) compared to the BM with a relatively planar interface (Figure 4-11i). In HAZ4 and HAZ5, no γ to δ phase transformation occurs during welding and dissolution of δ into the γ phase is difficult, due to the chemical compositional differences between γ and δ and the very low diffusion velocity of substitutional elements, such as chromium and nickel [2, 29], under the thermal cycling experienced locally in HAZ4 and HAZ5.

4.3.4 Microindentation hardness

The 2D hardness contour map generated throughout the entire surface of the CA6NM weldment after post-weld tempering is shown in Figure 4-12a. The microhardness profile measured along the mid-thickness of a transverse section of CA6NM weldment from BM to FZ is also displayed in Figure 4-12b. Six different microstructural zones – identified as the BM, FZ, HAZ2, HAZ3, HAZ4 and HAZ5 – were categorized and marked. The average hardness in the FZ center was 296 ± 7 HV (two standard deviations), which is significantly lower than that in the as-welded condition (~354 HV), as reported for hybrid laser-arc welded CA6NM, and comparable to the BM hardness (295 ± 10 HV).

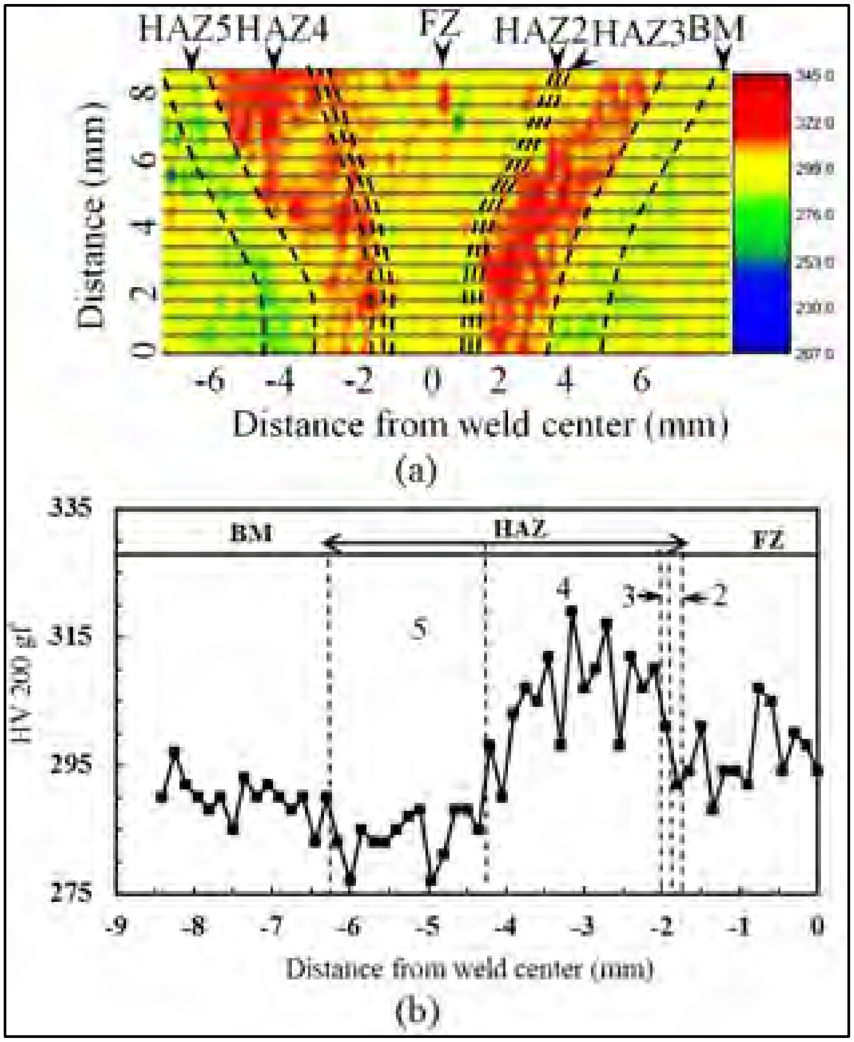

Figure 4-12 Microindentation hardness: (a) distribution map and (b) profile at mid-thickness

This softening after post-weld tempering is mainly due to the formation of tempered α′ and reversed γ. In addition, reduction in the carbon content within the α′ matrix due to the formation of chromium carbides contributes to this softening. The microhardness in the weldment increased from the fusion boundary to HAZ4, i.e. from an average value of 298 ±

5 HV in HAZ2 (high temperature single phase δ region) to 300 ±5 HV in HAZ3 (high temperature dual phase region) and reached a maximum value of 310 ± 7 HV in HAZ4 (single phase γ region) near the HAZ3/HAZ4 boundary. The maximum hardness in HAZ4 corresponded to the high temperature experienced in the single phase γ region during the weld heating cycle which promoted the dissolution of pre-existing chromium carbides in the BM (i.e. $M_{23}C_6$/M_7C_3) and consequently the increase in carbon concentration in the α′ matrix after cooling to room temperature. This causes a high hardness in the final microstructure that after post-weld tempering experiences a comparatively lower degree of softening. Moving from the location of maximum hardness in HAZ4 to the HAZ4/HAZ5 boundary, the hardness decreased and reached a minimum value in HAZ5 (290 ± 8 HV). The softening behaviour in HAZ5 is due to the fact that the thermal cycle experienced by HAZ5 is in the range of the tempering treatment applied. Double tempering can lead to further growth of the existing retained γ and the formation of reversed γ in the HAZ5 region, as clearly apparent from the SEM observations revealed in Figure 4-9h.

The formation and coarsening of the chromium carbides in HAZ5, as proved by the EBSD phase map (Figure 4-10), as well as the formation of reversed γ in HAZ5, can lead to the softening phenomenon in this region relative to the BM.

4.4 Conclusions

CA6NM, a low carbon 13% Cr-4% Ni martensitic cast stainless steel, was assembled using a hybrid laser-arc welding (HLAW) process using a butt joint configuration. The microstructures after post-weld tempering at 600°C for 1 hour were characterized using X-ray diffraction, field emission scanning electron microscopy and electron backscatter diffraction (EBSD) analysis.

1. The fusion zone of the hybrid laser-arc welded CA6NM in the post-weld tempered condition mainly consisted of tempered lath martensite (α′) matrix, reversed austenite (γ), chromium carbides (i.e. M_7C_3 and possibly $M_{23}C_6$), and residual delta ferrite (δ) located at the prior-austenite grain boundaries with various morphologies.

2. The substructure of the lath α′ in the CA6NM weld consisted of packets containing several blocks and a lath structure. The prior-γ and packets misorientation angles were in the range of 60 to 85°. The low angle misorientations ($\Theta<10°$) were related mainly to block boundaries.
3. The reversed γ in the fusion zone after post-weld tempering was formed along the α′ lath boundaries, particularly at triple junctions of the lathes due to a higher interfacial free energy at these locations. The reversed γ nearly maintained a Kurdjumov-Sachs orientation relationship with the martensitic matrix with a certain degree of scattering around the ideal orientations under EBSD investigation.
4. Residual δ was observed with different morphologies in the fusion zone. Depending on the growing morphology of γ from δ at high temperatures, residual δ phases were detected predominately between prior-Widmanstätten γ boundaries with symmetrical and orientational morphology. The change in δ/γ interfaces may happen in order to overcome the diffusional barrier during solid state phase transformation.
5. Four different heat affected zones (HAZs) were distinguishable, each exhibiting a lath tempered α′ microstructure after post-weld tempering. Fine reversed γ films were observed from HAZ2 to HAZ5 predominately along the α′ laths boundaries and lath triple junctions. The widths of the reversed γ films increased slightly from HAZ2 (less than 100 nm) to HAZ5 (150-250 nm). Chromium carbides of the type M_7C_3 were also detected in HAZ5. The formation of $M_{23}C_6$ carbides is also possible during the post-weld tempering process, though they were not resolvable using EBSD analysis in this work.
6. During welding, the pre-existing δ in HAZ2 and HAZ3 showed a morphological change from a planar to columnar interface with prior-γ, which takes place during cooling from the high temperatures through δ/γ transformation.
7. The average hardness in the tempered fusion zone was ~296 HV. A maximum hardness occurred in HAZ4, near the HAZ3/HAZ4 boundary while a minimum hardness was detected in HAZ5. Hardening in HAZ4 was ascribed to the high temperatures experienced during the weld heating cycle that preceded the dissolution of pre-existing chromium carbides in the base metal (i.e. $M_{23}C_6/M_7C_3$) and consequently increased the carbon concentration in the martensitic matrix at room temperature. Maximum softening in

HAZ5 after post-weld tempering was a result of the double-tempering effect in the base metal, with the possibility of further growth of the retained γ, formation of newly reversed γ and coarsening of the chromium carbides.

Acknowledgements

The authors would like to thank Alstom Canada, Hydro-Québec, the National Science and Engineering Research Council of Canada (NSERC) and the Aeronautics for 21st Century Program of the National Research Council of Canada (NRC) for their financial support. The technical assistance of E. Poirier and X. Pelletier at NRC Aerospace during the welding experiments and metallographic preparation is gratefully acknowledged.

References

1) Song, Y. Y., D. H. Ping, F. X. Yin, X. Y. Li, and Y. Y. Li. Microstructural evolution and low temperature impact toughness of a Fe–13% Cr–4% Ni–Mo martensitic stainless steel. Materials Science and Engineering: A, 2010. 527(3): p. 614-618.

2) Wang, P., S. P. Lu, N. M. Xiao, D. Z. Li, and Y. Y. Li. Effect of delta ferrite on impact properties of low carbon 13Cr–4Ni martensitic stainless steel. Materials Science and Engineering: A, 2010. 527(13): p. 3210-3216.

3) Krauss, G., Steels Heat Treatment and Processing Principles ASM International. Materials Park, 1993.

4) Kitahara, H., Ueji, R., Tsuji, N., and Minamino, Y. Crystallographic features of lath martensite in low-carbon steel. Acta materialia, 2006. 54(5): p. 1279-1288.

5) Morito, S., Tanaka, H., Konishi, R., Furuhara, T., and Maki, T. The morphology and crystallography of lath martensite in Fe-C alloys. Acta Materialia, 2003. 51(6): p. 1789-1799.

6) Bagger, C., and Olsen, F. O. Review of laser hybrid welding. Journal of laser applications, 2005. 17: p. 2-14

7) Carrouge, D. Phase transformations in welded supermartensitic stainless steels. PhD thesis, University of Cambridge, 2003.

8) Enerhaug, J. and U. Steinsmo, Factors affecting initiation of pitting corrosion in super martensitic stainless steel weldments. Science and Technology of Welding & Joining, 2001. 6(5): p. 330-338.

9) Thibault, D., P. Bocher, and M. Thomas, Residual stress and microstructure in welds of 13% Cr–4% Ni martensitic stainless steel. Journal of Materials Processing Technology, 2009. 209(4): p. 2195-2202.

10) Sarafan, S., P. Wanjara, H. Champliaud, and D. Thibault. Characteristics of an autogenous single pass electron beam weld in thick gage CA6NM steel. The International Journal of Advanced Manufacturing Technology, 2016: p. 1-13.

11) Mirakhorli, F., Cao, X., Pham, X.T., Wanjara, P. and Fihey, J.L. Post-weld Tempered Microstructure and Mechanical Properties of Hybrid Laser-Arc Welded Cast Martensitic Stainless Steel CA6NM. Metallurgical and Materials Transactions B: p. 1-12.

12) Ünlü, N., Genc, A., Öveçoğlu, M. L., Eruslu, N., and Froes, F. H. Characterization investigations of melt-spun ternary Al-xSi-3.3Fe (x=10, 20 wt.%) alloys. Journal of Alloys and Compounds, 2001. 322(1-2): p. 249-256.

13) Schwartz, A. J., Kumar, M., Adams, B. L., and Field, D. P. (Eds.).Electron backscatter diffraction in materials science. Vol. 2. 2009. New York:Springer.

14) Humphreys, F. J. Review grain and subgrain characterisation by electron backscatter diffraction. Journal of materials science, 2001. 36(16): p. 3833-3854.

15) Amrei, M. M., Monajati, H., Thibault, D., Verreman, Y., Germain, L., and Bocher, P. Microstructure characterization and hardness distribution of 13Cr4Ni multipass weld metal. Materials Characterization, 2016. 111: p. 128-136.

16) Morito, S., Yoshida, H., Maki, T., and Huang, X.Effect of block size on the strength of lath martensite in low carbon steels. Materials Science and Engineering: A, 2006. 438–440: p. 237-240.

17) Thibault, D., Bocher, P., Thomas, M., Lanteigne, J., Hovington, P., and Robichaud, P. Reformed austenite transformation during fatigue crack propagation of 13%Cr–4%Ni stainless steel. Materials Science and Engineering: A, 2011. 528(21): p. 6519-6526.

18) De, A. K., Murdock, D. C., Mataya, M. C., Speer, J. G., and Matlock, D. K. Quantitative measurement of deformation-induced martensite in 304 stainless steel by X-ray diffraction. Scripta materialia, 2004. 50(12): p. 1445-1449.

19) Folkhard, E., G. Rabensteiner, and E. Perteneder, Welding metallurgy of stainless steels. Vol. 98. 1988: Springer-Verlag Vienna.

20) Mirakhorli.F, C.X., Pham. X.T , Wanjara.P and Fihey. J-L Hybrid Fiber Laser–arc Welding of 10-mm Thick CA6NM Stainless Steel, in Materials Science & Technology 2014 2014: Pittsburgh, PA, USA

21) Leone, G. and H. Kerr, The ferrite to austenite transformation in stainless steels. Welding Journal, 1982. 61(1): p. 13S-21S.

22) Ohmori, Y., Nakai, K., Ohtsubo, H., & Isshiki, Y. Mechanism of Widmanstaetten Austenite Formation in a. DELTA./. GAMMA. Duplex Phase Stainless Steel. ISIJ international, 1995. 35(8): p. 969-975.

23) Kokawa, H., T. Kuwana, and Yamamoto, A. Crystallographic characteristics of delta ferrite transformations in a 304L weld metal at elevated temperatures. Weld. J, 1989. 68(3).

24) Song, Y. Y., Li, X. Y., Rong, L. J., Ping, D. H., Yin, F. X., and Li, Y. Y. Formation of the reversed austenite during intercritical tempering in a Fe–13% Cr–4% Ni–Mo martensitic stainless steel. Materials Letters, 2010. 64(13): p. 1411-1414.

25) Liu, L., Z.G. Yang, and C. Zhang, Effect of retained austenite on austenite memory of a 13% Cr–5% Ni martensitic steel. Journal of Alloys and Compounds, 2013. 577: p. S654-S660.

26) Krauss, G., Tempering of martensite in carbon steels, in Phase Transformations in Steels: Diffusionless Transformations, High Strength Steels, Modelling and Advanced Analytical Techniques. Vol. 2. 2012. Woodhead Publishing. p. 126-150

27) Vandyoussefi, M., Kerr, H. W., & Kurz, W. Directional solidification and δ/γ solid state transformation in Fe3% Ni alloy. Acta materialia, 1997. 45(10): p. 4093-4105.

28) Arai, Y., Emi, T., Fredriksson, H., & Shibata, H.In-situ observed dynamics of peritectic solidification and δ/γ transformation of Fe-3 to 5 at. pct Ni alloys. Metallurgical and Materials Transactions A, 2005. 36(11): p. 3065-3074.

29) Li, S., Eliniyaz, Z., Zhang, L., Sun, F., Shen, Y., & Shan, A. Microstructural evolution of delta ferrite in SAVE12 steel under heat treatment and short-term creep. Materials Characterization, 2012. 73: p. 144-152.

CHAPTER 5

TECHNICAL CHALLENGES IN NARROW-GAP ROOT PASS WELDING DURING TANDEM AND HYBRID LASER-ARC WELDING OF A THICK MARTENSITIC STAINLESS STEEL

F. Mirakhorli[1,2], X. Cao[2], X.-T. Pham[1], P. Wanjara[2] and J.-L. Fihey[1]

[1]École de technologie supérieure, Montréal, Québec, Canada, H3C 1K3
[2]National Research Council Canada – Aerospace, Montréal, Québec, Canada, H3T 2B2

This paper was presented in THERMEC 2016 Conference and will be published in Materials Science Forum Journal.

Keywords: Hybrid laser-arc welding; tandem laser-arc welding; martensitic stainless steel; thick plate; narrow-gap groove

Abstract

As part of a collaborative program to develop advanced manufacturing processes for next-generation hydraulic turbines, this study investigated the technological challenges for joining 25-mm thick martensitic stainless steel (MSS) plates using tandem and hybrid laser-arc welding. Although candidate materials for the intended application typically include wrought AISI 415 and cast CA6NM, a martensitic 410 stainless steel (SS) was especially selected in this study due to its greater crack sensitivity. A narrow-gap groove was designed to minimize the amount of 410NiMo filler metal required to fill the groove using a multi-pass single-sided welding technique. All the welding trials were performed using a 5.2 kW fiber laser. The root pass quality was characterized in terms of weld bead geometry, defects and microstructure. The main technical challenges observed for the root pass were lack of penetration, lack of fusion and cracking, as detailed in this work.

5.1 Introduction

Assembly of heavy section components, such as turbines in the hydropower industry, is a great challenge due to the complexity and heavy thickness of the geometry. These components are fabricated from low carbon MSS that possesses high hardness and strength, as well as good corrosion resistance and impact properties. In order to enhance the life span of the turbine, to reduce the long term operating costs and to assure high weld quality, the development of advanced welding technologies, such as laser and coupled laser-arc welding, is ongoing [1]. Using a high energy density laser as a heating source allows deep penetration and fast welding speeds, thus reducing the heat input, size of the heat affected zone (HAZ), and the total number of passes needed to fill a thick butt joint. Gas metal arc welding (GMAW) coupled with the laser enhances gap-bridging ability [2], assures a better control of the chemistry of the weld pool through the selection of an appropriate filler metal, compensates the metal lost by evaporation and reduces the cooling rate. Single pass hybrid laser-arc welding (HLAW) of a 10-mm thick low carbon MSS has been already studied by the authors [3]. In the present work, tandem and/or HLAW processes were applied to weld 25-mm thick AISI 410 SS using a narrow-gap groove design. The objective was to investigate the technological challenges during multi-pass tandem/HLAW of thick MSS sections, specifically for root pass welding. The physical properties and microstructural characteristics of AISI 410 SS are quite similar to AISI 415 SS, but it is more crack sensitive due to its higher carbon content (0.13 w%) [4]. Thus AISI410 SS was selected in this study in order to intensify the manufacturing challenges for research purposes. The welded joints were characterized in terms of the defects and microstructures.

5.2 Experimental

AISI 410 SS was received in the annealed condition with a thickness of 25 mm and a chemical composition as listed in Table 5-1. Workpieces with dimensions of 50 mm (width) by 150 mm (length) were cut from the as-received base metal (BM). Welding was performed along the length direction. The laser equipment consisted of an IPG Photonics 5.2 kW continuous wave solid-state Yb-fibre laser (YLR-5000) mounted on an ABB robot. A collimation lens of 200 mm, a focal lens of 300 mm and a fiber diameter of 200 μm were utilized to produce a nominal focusing spot diameter of 0.3 mm. All experiments were conducted at a defocusing distance of -3 mm and a maximum laser power of 5.2 kW in the "laser-leading" mode. The GMAW power supply was a Fronius Trans Pulse Synergic 4000 CMT. The chemical composition of the ER410NiMo filler wire with a diameter of 1.14 mm (0.045") is also shown in Table 5-1. It should be noted that both the BM and filler metal had a very low sulfur content. The oxygen content of the 410 SS was also low, but that of the filler metal was not quantified. Two different kind of trials were performed, (i) inside the groove and (i) bead-on-plates (BOP). For all the groove joint tests, high purity Ar gas that was fed through the GMAW nozzle at a flow rate of 23.6 l/min was used for shielding and trailing the top surface of the weld. Gas mixtures of Ar-2%O_2 and Ar-4%O_2 were also used for the GMAW BOP trials. The bottom surface was shielded using a mixture of 50% He and 50% Ar at a flow rate of 9.44 l/min (20 cfh). The laser–arc distance (D) was varied between 2 and 10 mm in order to encompass the full spectrum from HLAW at a distance of 2 mm (Figure 5-1a) to tandem laser-arc welding at distances of 6 mm and 10 mm (Figure 5-1b). The angle between the electrode axis and the work-piece surface was 65°. The tandem/HLAW process was developed to specifically achieve root pass welding in the 25-mm thick AISI 410 SS plates using a narrow-gap butt joint configuration with a Y-shaped groove, as illustrated in Figure 5-1c. The full groove angle was ~ 27º with a root size of 5 mm. The root gap varied from 0.1 to 0.2 mm. For all welding passes including BOP trials, the nominal wire feed rate (WFR) and the welding speed were 17.0 m/min and 1.0 m/min, respectively. Table 5-2 lists the other process parameters used.

Table 5-1 Chemical compositions of 410 SS plates and ER410NiMo filler wire (wt. %)

Elements (Wt. %)	**C**	**Si**	**Mn**	**P**	**S**	**Cr**	**Ni**	**Mo**	**Cu**	**N**	**O**
410 SS	0.13	0.41	0.39	0.017	0.001	12.3	0.15	0.021	0.056	0.041	0.006
410NiMo	0.02	0.37	0.34	0.017	0.0009	12.2	4.57	0.42	0.12	-	-

Several K-type thermocouples were spot welded on the workpiece. On the top and bottom surfaces, the thermocouples were positioned, respectively, 12 mm and 3 mm away from the edge of the joint line. With this setup, the preheat temperature was assured to be within the required range (100-120°C) throughout the entire thickness and the thermal cycle in the vicinity of the HAZ was measured using the iNET-240 acquisition system.

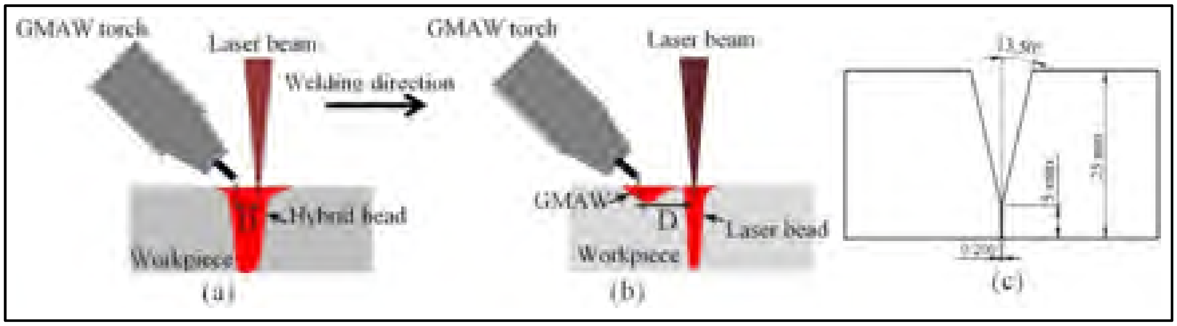
GMAW torch
Laser beam
Welding direction
D
Hybrid bead
Workpiece
(a)
GMAW torch
Laser beam
GMAW
D
Laser bead
Workpiece
(b)
13.50°
5 mm
25 mm
0.200
(c)

Figure 5-1 Schematic of (a) hybrid welding, (b) tandem welding, and (c) groove design

Table 5-2 Process parameters used for the root pass in the narrow groove and BOP tests

Trial #	Pass #	Laser-arc distance D (mm)	Voltage (V)	Current (A)	Preheat (°C)	Shielding gas
1	Root	N/A	-	-	100-120	Pure Ar
2	Root	2	24	191	100-120	Pure Ar
3	Root	6	25	331	100-120	Pure Ar
4	Root	10	24	333	100-120 and 25*	Pure Ar
5	Second on pass #1	2	26	332	100-120	Pure Ar
6	BOP	N/A	24.3	227	25	Pure Ar
7	BOP	N/A	23	285	25	Ar-2%O_2
8	BOP	N/A	26	301	25	Ar-4%O_2

* For measurement of the thermal cycle, a special test was conducted at room temperature

Specimens were extracted from the weld cross-sections for metallographic preparation that involved grinding, polishing and etching in Villella's reagent. An inverted optical microscope (Olympus GX71) was used to examine the microstructure.

5.3 Results and discussion

5.3.1 Thermal cycles

Figure 5-2a-b show the thermal cycles measured in the vicinity of the HAZ for trial #4, which was performed at two different initial temperatures (room temperature and 100°C). It is noteworthy that all other trials were welded using 100°C preheating to (1) help achieving the full penetration and (2) reduce the thermal stress during laser-arc welding to minimize cracking issue in this material. Since the maximum temperature recorded during welding with a 100°C preheat was 762°C, the cooling rates in the 750-500°C range, instead of the usual 800-500°C range, were chosen for comparison purposes. In this temperature range, the cooling rate (156°C/s) in the 100°C preheated weld was slightly reduced compared to that (240°C/s) without preheating. However, as expected, preheating had a greater effect on the cooling rates in the lower temperature range, e.g. between 500-300°C, the rate was ~22°C/s and ~44°C/s with and without preheating at 100°C, respectively. It is noteworthy that without preheating the cooling rate for the 800-500°C range was ~260°C/s.

5.3.2 Weld macrographs and defects

Figure 5-2c-g show the macrographs of the weld cross-sections taken from each joint. Figure 5-2c demonstrates the laser only root pass weld (i.e. without the arc and filler metal addition). Figure 5-2d-f show the weld transverse sections of the root passes at laser-arc distances of 2, 6 and 10 mm, respectively. Figure 5-2g displays the second HLAW pass added to weld #1 (laser only). Laser-arc distance had a great effect on weld bead geometry during laser-arc welding. As shown in Figure 5-2d, at a laser-arc distance of 2 mm, during HLAW, a unique molten pool was produced. By increasing the laser-arc distance to 6 mm, the bottom of the

GMAW bead penetrates the laser weld (Figure 5-2e), but the macrostructures of the two weld beads are distinct. Thus it is reasoned that the two weld pools were separated. However, it is possible that some connection between the two weld pools may have existed at the rear end of the laser pool. At a laser-arc distance of 10 mm (Figure 5-2f), the lack of fusion between the two weld beads indicates that two separated molten pools were formed. In this case, the process is called tandem laser-arc welding (TLAW), as the second weld bead is deposited on the first bead just after its solidification.

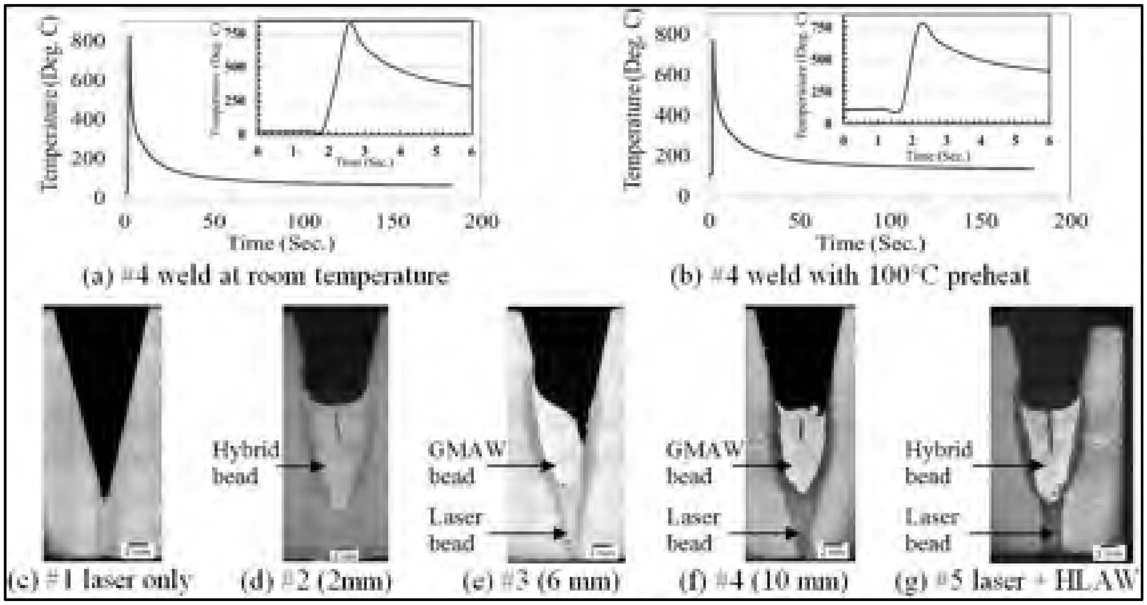

Figure 5-2 Thermal cycles for root pass weld #4 (a, b) and transverse cross-sections of the 5 welds (c-g)

As magnified in Figure 5-3, four main defects, namely incomplete penetration, lack of fusion, cracking and porosity, were observed during root pass laser-arc welding using a narrow-gap groove. Also, Figure 5-3f shows the lack of weld metal on the right side of the GMAW pass; this is related to the visual observation of arc deviation (blow) during welding. The laser weld displayed systematically a lack of penetration at the bottom of the root (Figure 5-3a). This lack of penetration is in the range of 1-2 mm for all the welds except the hybrid weld #2 where it reaches 4.5 mm (Figure 5-2d). It is noteworthy that no remarkable change was observed in root penetration depth using 100 °C preheat compare to condition without preheat. This is due to the fact that during high power laser or laser-arc welding, the penetration depth is predominantly controlled by keyhole formation and full penetration is achieved when the laser power is sufficient to allow the keyhole to extend to the bottom of the work piece. The lack of penetration could have been avoided with a higher laser power. The lack of fusion appeared between the laser and GMAW beads during TLAW at a laser-arc distance of 10 mm, when the process formed two separated molten pools (Figure 5-2f and Figure 5-3b). For this welding condition, it seems that the narrow geometry of the V-groove may limit the penetration as the energy of the arc is transferred to the sides of the groove rather than to the bottom. Specifically, Abe et al. [5] pointed out that in a narrow groove the arc does not reach the bottom of the groove, which may increase the risk of a lack of fusion between the two beads. Chen [6] also simulated the influence of the V-groove angle on fluid flow during the GMAW process and found that a larger angle promotes downward metal flow that helps to increase the penetration depth.

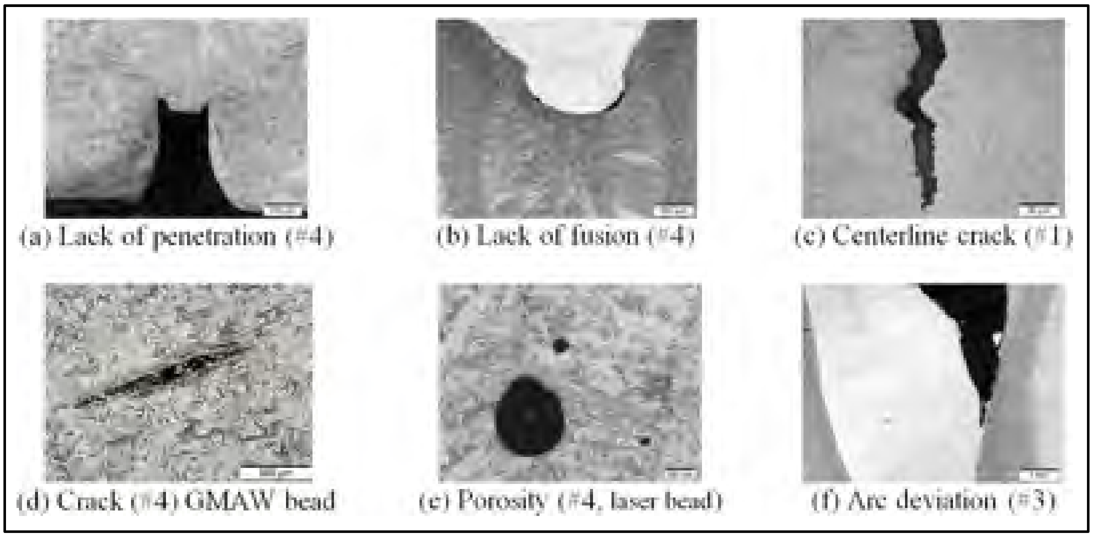

(a) Lack of penetration (#4)
(b) Lack of fusion (#4)
(c) Centerline crack (#1)
(d) Crack (#4) GMAW bead
(e) Porosity (#4, laser bead)
(f) Arc deviation (#3)

Figure 5-3 Defects observed in the weld cross-sections

The lack of fusion between the laser and GMAW beads may also be a consequence of the low sulfur and oxygen contents of both the base and weld metals, which would promote radial outward Marangoni flow at the surface and thus shallow weld beads. In arc welding of stainless steel, it is known that the weld bead shape is sensitive to the amount of surface-active elements, such as oxygen and sulfur. A higher content of these elements can change the temperature coefficient of the surface tension from a negative to a positive value, leading to downward fluid flow and deeper penetration [7, 8].

The effect of oxygen as a surface-active element was studied by depositing three GMAW beads on a 25-mm thick 410 SS plate (that had the same composition as the plates for the groove tests) using three different shielding gases, namely high purity Ar, Ar-2%O_2 and Ar-4%O_2 (#6, #7, #8 in Table 5-2). Figure 5-4 presents the weld cross-sections of these three trials. The weld penetration increased from 0.7 mm for high purity Ar to 2.0 mm for Ar-2%O_2 and 2.7 mm for Ar-4%O_2. It seems that the addition of oxygen to the shielding gas changes the temperature coefficient of the surface tension from negative to positive. Further experimentation is needed to investigate the same effect inside a narrow groove. It is worth mentioning that at high oxygen concentrations, a thick oxide film can cover most of the liquid pool surface and consequently inhibit the Marangoni convection [8].

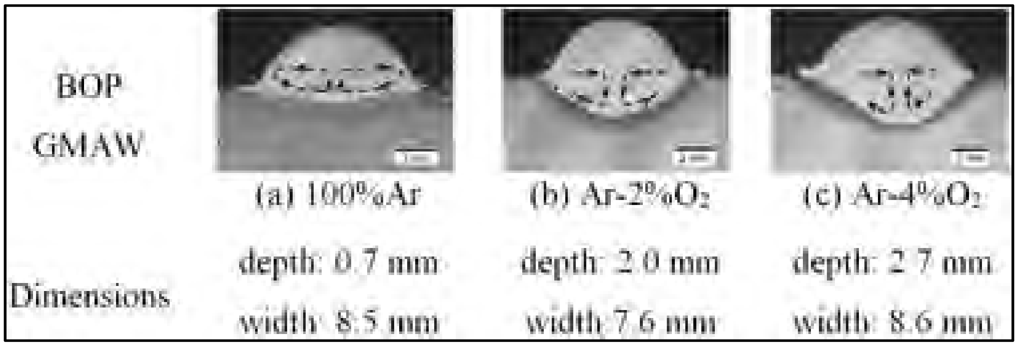

Figure 5-4 BOP GMAW using three different shielding gases

The lack of fusion defect between the laser and GMAW beads appeared resolved for two conditions: (1) TLAW at a laser-arc distance of 6 mm (Figure 5-2e) that may be due to the higher temperature of the laser bead just in front of the GMAW molten pool and (2) laser root pass with HLAW (Figure 5-2g). In both cases, the lack of fusion and top centerline crack in the laser bead was repaired by the subsequent pass on the laser root pass.

Cracks were observed during laser, tandem and hybrid laser-arc root pass welding of 25-mm thick 410 SS with and without preheating. Centerline cracks starting from the concave top surface of the laser bead are observed in Figure 5-2c and Figure 5-3b. Centerline cracks are also observed at the top of the GMAW and hybrid beads (Figure 5-2d, f, g). The rounded edges of the cracks, as shown in Figure 5-3c, point to hot cracking. The main factors responsible for the centerline cracking are: (1) the temperature gradient between the bottom and top surfaces of the root pass, (2) the high restraint of the weld due to the high depth-to-width ratio, (3) the stresses due to solidification shrinkage, (4) the fast cooling rate during laser and laser-arc welding and (5) the concave shape of the bead top surface. A high carbon content can also increase the hot cracking susceptibility of MSS [4]. Although centerline cracking is mostly related to solidification cracking, i.e. the formation of interdendritic low melting liquid films in the last stage of solidification [4]. Castner [9] observed centerline cracking in 410 SS during GMAW in flat and concave weld deposits and suggested that it was not formed during solidification, but over the temperature range of 870-1370°C, in the dual phase delta ferrite (δ) plus austenite (γ) region. The stress concentration in the δ and at the δ/γ grain boundaries may locally initiate fine cracks that can then propagate during further cooling [9]. For example, horizontal cracks in the GMAW beads are shown in Figure 5-3d and Figure 5-5b; the latter also reveals the presence of micro-cracks along the previous δ/γ interface. This observation is in line with the theory of Castner [9]. Although 100 °C preheating was used to reduce the thermal stress and strain during laser-arc welding process and avoid cracking, the centerline hot crack could not be eliminated completely during laser and laser-arc welding process in this study. Reducing the carbon content of the 410 martensitic SS base metal (e.g. using low carbon martensitic SS such as 415 SS) and controlling the weld depth to width ratio can be helpful to avoid centerline cracking in this case.

During laser welding, TLAW and HLAW of 410 SS, porosity was also observed to occur mostly in the fusion zone (FZ) center and close to the fusion boundary. Formation of porosity can be due to the entrapment of shielding gas or to the instability of the keyhole during laser welding [10]. Another defect observed during narrow-gap TLAW or HLAW of root pass was arc deviation or blow (Fig. Figure 5-3f). The narrow-gap groove design concentrates the magnetic field at the root of the weld, which could lead to arc blow [11].

5.3.3 Microstructure

The BM microstructure of the 410 SS in the as-received condition (Figure 5-5a) consisted of martensite and δ. The FZ microstructure in the as-welded condition mainly consisted of lath martensite and networks of δ, as shown in Figure 5-5b-c.

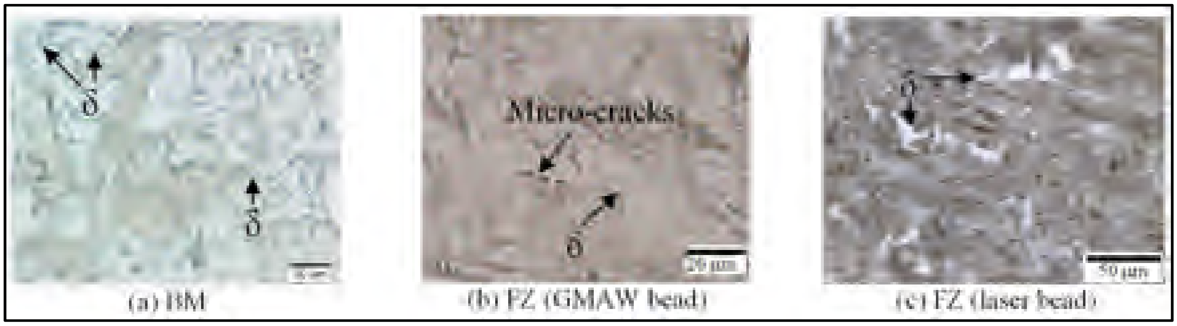

(a) BM (b) FZ (GMAW bead) (c) FZ (laser bead)

Figure 5-5 Microstructure of the BM and FZ (TLAW with 10 mm laser-arc distance, #4)

The network of δ observed in the laser bead (formed by re-melting the 410 SS BM) was coarser than that observed in the GMAW or HLAW beads, which were formed from a mixture of the 410NiMo filler metal and the 410 SS BM (Figure 5-5c). According to the modified Cr equivalent formula for MSS (Cr_{eq}= Cr + 6Si + 4Mo + 8Ti + 12Al + 5Nb + 1.5 W + 11 V − 2Mn − 4Ni − 40C − 30N − 2Cu − Cu) [4], 410 SS has a higher Cr equivalency than the 410NiMo filler metal. Referring to Table 5-1, this is related to the very low amount of Ni in the 410 SS compared to the 410NiMo filler metal. Therefore the amount of δ in the autogenous laser root pass is expected to be higher than in the GMAW or HLAW beads.

5.4 Conclusions

1. The most common welding defects observed during tandem and hybrid laser-arc root pass welding of 25 mm-thick 410 SS, using narrow-gap groove were lack of penetration, lack of fusion, porosity and cracks.

2. The systematic occurrence of the lack of penetration defect in the 5 mm root indicates that the maximum laser power of 5.2 kW was insufficient.
3. The lack of fusion between the laser and GMAW beads occurred at a laser-arc distance of 10 mm during TLAW. The poor penetration of the GMAW pool in the solidified high temperature laser bead may be related to the very low sulfur content of both the base and weld metals, which promotes radial outward Marangoni flow at the surface, and, thus, a shallow and wide weld pool. The narrow groove design may also be a factor if the energy of the arc is transferred to the sides of the groove rather than to the bottom. This defect could be eliminated by reducing the laser-arc distance to 6 mm during TLAW or by applying HLAW on a laser root pass.
4. Centerline hot cracking was systematically observed at the top of the laser, GMAW and HLAW beads. The contributing factors are the high carbon content, high cooling rate, and the high depth-to-width ratio of the beads inside the narrow groove. Decreasing the depth-to-width ratio of the weld and the carbon content should alleviate this problem.

Acknowledgements

The authors are grateful to E. Poirier and X. Pelletier of the National Research Council of Canada (NRC) for their technical assistance. Thanks are also due to Hydro-Québec, Alstom renewable Energy, National Science and Engineering Research Council of Canada (NSERC) and the Aero 21 Program of NRC for their financial support.

References

1) M. Zhang, G. Chen, Y. Zhou, S. Liao, Optimization of deep penetration laser welding of thick stainless steel with a 10kW fiber laser, Mater. Des. 53 (2014) p. 568-576.
2) C. Bagger, F.O. Olsen, Review of laser hybrid welding. J. Laser. Appl . 17 (2005).
3) F. Mirakhorli, X. Cao, X.T. Pham, P. Wanjara, J-L. Fihey, Hybrid Fiber Laser–arc Welding of 10-mm Thick CA6NM Stainless Steel, Materials Science & Technology. (2014) Pittsburgh, PA, USA.

4) J.C. Lippold, D.J. Kotecki, Welding metallurgy and weldability of stainless steels, Wiley-VCH, 2005.

5) N. Abe, M. Hayashi, Trends in laser arc combination welding methods, Weld. Int. 16 (2002). p.94-98.

6) J. Chen, C. Schwenk, C. S. Wu, M. Rethmeier, Predicting the influence of groove angle on heat transfer and fluid flow for new gas metal arc welding processes, Int. Journal. Heat Mass Transfer, 55 (2012), p.102-111.

7) Y. Wang, H.-L. Tsai, Effects of surface active elements on weld pool fluid flow and weld penetration in gas metal arc welding, Metall. Mater. Trans B. 32 (2001), p. 501-515.

8) LU. Shanping, F. Hidetoshi, T. Manabu, N. Kiyoshi, Weld shape variation in Ar-O2 and Ar-CO2 shielded GTA welding, Transactions of JWRI 33, 1 (2004), p 5-9.

9) H. Castner, Cause and prevention of 12% chromium steel fillet weld cracks, Weld. J. Research Supplement, 56, (1977).

10) Matsunawa, Problems and solutions in deep penetration laser welding, Sci. Technol. Weld. Joining, 6 (2001), p. 351-354.

11) Blakeley, P., Magnetic arc blow-causes and remedies. Weld Met Fabr, 59 (1991).

CHAPTER 6

HYBRID/TANDEM LASER-ARC WELDING OF 25-MM THICK 415SS PLATES WITH A NARROW-GAP GROOVE CONFIGURATION

F. Mirakhorli[1,2], X. Cao[2] , X-T. Pham[1], P. Wanjara[2] and J. L. Fihey[1]

[1]École de technologie supérieure, Montréal, Québec, Canada, H3C 1K3
[2]National Research Council Canada – Aerospace, Montréal, Québec, Canada, H3T 2B2

Keywords: Hybrid & tandem laser-arc welding; Narrow groove design; Stainless steel; Mechanical testing.

To be submitted to The International Journal of Advanced Manufacturing Technology

ABSTRACT

Single-side tandem/hybrid laser-arc welding process was investigated to join 25 mm-thick wrought low carbon martensitic stainless steel plates with a narrow-gap groove configuration (10-mm root size with 40° included angle). Parameter optimisation was specifically performed on root pass trials using different laser powers and laser-arc distances. Then the groove was filled with four filling passes. The joint integrity was characterized in terms of weld bead geometries and defects in both root and filling passes. The main imperfections observed were metal loss due to severe evaporation and spatter, keyhole instability in root pass, porosity and crack. The tensile properties for the top and bottom sections of the joint were evaluated. The ultimate tensile and yield strengths at the top and bottom of the weld passed the minimum requirement of ASTM standard. The tensile fracture occurred in the base metal (BM) and the fusion zone (FZ) for top and bottom samples respectively. The latter case was due to the big porosity formed at the bottom of second and third passes. The Charpy impact energy performed in the FZ of the tandem laser-arc root pass at two different preheating temperatures revealed quite high impact energy of 88 J for the root pass at 40 °C preheating. It was observed for the 90 °C preheat Charpy specimen that the fracture path deviated from the narrow root pass FZ to BM.

6.1 Introduction

Root pass hybrid and tandem laser-arc welding of 25-mm-thick martensitic stainless steels using 5.2 kW fiber laser power were performed and analysed in Chapter 5. Some defects such as lack of penetration in the root pass could be attributed to the limited laser power available. Increasing the laser power can help to increase the depth of penetration, adopt a groove with a large root size, and thus reduce the number of passes needed to fill the groove. For example, conventional arc welding of 25 mm-thick HSLA steel was performed using approximately 15 passes for a large V groove design [1]. During application of high laser power on thick plate components, however, some new challenges may appear such as instability of the keyhole, increased metal evaporation and spatter [2, 3], which necessitate solid understanding of the thermo-mechanical phenomena during deep keyhole laser welding. This could be more complicated when combining laser welding with gas metal arc welding to form a single process such as hybrid laser-arc welding (HLAW). However, the potential benefits obtained by coupling the two heat sources are interestingly high for thick sections assembly in heavy manufacturing industries. The laser beam offers high welding speed and deep penetration in a single pass; whereas the arc energy is used to increase the gap-bridging ability and control metallurgical properties through the addition of appropriate filler wire which overall leads to increased productivity. In spite of these benefits, this welding technology has not been widely applied in today's industry. The lack of knowledge on the novel and complex hybrid welding process is the principal limiting factor. Several researches have been performed to better understand and optimize the HLAW process, in bead-on-plate [4, 5] or single pass welds [6, 7]. In term of thick plates, single-pass HLAW process was used to weld 20-25 mm-thick steel using 20 kW fiber laser in I-butt joint and the stability of the root side was controlled using different backing materials. However, few researches have been performed on multi-pass hybrid laser-arc welding of thick plates with a narrow-gap groove configuration, especially for low carbon martensitic stainless steels (SS). Different parameters such as laser-arc distance and laser power can have a great effect on the interaction between the laser beam and arc and on the weld pool shape, especially for the root pass.

In the present study, single side laser-arc welding process was applied to weld 25-mm thick 415 (SS) using narrow-gap groove configuration. The effect on the stability of the welding process of different parameters, such as laser-arc distance and laser power, was investigated, with special attention given to the root of the joint. The weld geometries, defects and interaction between the laser and arc on weld pool formation were analysed. The toughness properties of the joints were also evaluated and correlated to the fracture surface features through fractographic analysis.

6.2 Experimental procedures

415 martensitic stainless steels (SS) plates with dimensions of 150 mm in length × 50 mm in width × 25.4 mm in thickness were used as a base metal (BM) with a chemical composition as given in Table 6-1. It is noteworthy that prior to machining, the as-received 415 SS was heat treated, first normalized at 1000°C and soaked at this temperature for 30 min, air cooled to a temperature below the martensite finish temperature (M_f) of 90°C, and tempered at 600°C for 4 hours.

Two different welding systems were used, one for the root pass and one for the filling passes. The root pass was performed using a Lincoln Power Wave 655 power supply coupled with a IPG photonics 15 kW continuous wave solid-state Yb-fiber laser equipped with a collimating lens of 150 mm, a focal lens of 300 mm and a fiber diameter of 0.4 mm, which produced a nominal focusing spot diameter of ~ 0.8 mm. Then four filling passes were added up to the root pass to fill the narrow groove using a Fronius Trans Pulse Synergic 4000 CMT GMAW power supply coupled with a IPG photonics 5.2 kW continuous wave solid-state Yb-fiber laser with a collimating lens of 200 mm, a focal lens of 300 mm and a fiber diameter of 0.2 mm, which produced a nominal focusing spot diameter of ~ 0.30 mm. The filler metal used for both root and filling passes was ER410NiMo with chemical composition shown in Table 6-1. The angle between the electrode axis and the workpiece surface in the welding direction was 65°.

Table 6-1 Chemical compositions of 410 SS plates and ER410NiMo filler wire (wt. %)

Elements (Wt. %)	C	Si	Mn	P	S	Cr	Ni	Mo	Cu	N	O
415 SS	0.017	0.52	0.87	0.021	0.001	12.3	4.7	0.64	0.2	0.03	0.002
410NiMo	0.02	0.37	0.34	0.017	0.0009	12.1	4.6	0.42	0.1	-	-

To protect the molten weld pool during welding, the top and bottom surfaces of the workpiece were shielded using pure argon, at a flow rate of 23.6 l/min and 9.5 l/min respectively, fed by the gas metal arc welding (GMAW) torch nozzle. The groove design was Y-groove shape with 10-mm root size, 40° included angle and a root opening (gap size) of 0.15-0.2 mm as depicted in Figure 6-1. The 415 SS plates were ground and cleaned with acetone and then fixed within a hydraulic clamping device before welding.

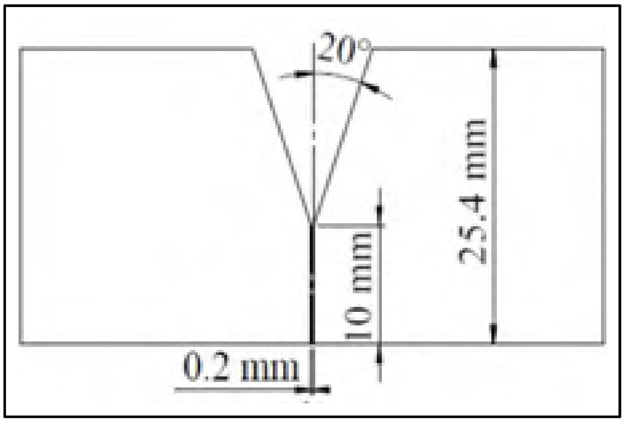

Figure 6-1 Narrow-gap groove design

In the present work, the laser-arc distance for the root pass was varied from 12 mm to 25 mm for different trials. The laser-arc distance for the filling passes at 5.2 kW laser power was fixed at 2 mm. The combined laser-arc welding process was conducted in laser-leading mode for all experiments. Table 6-2 displays the weld process parameters, laser power, welding speed, wire feed rate (WFR), arc voltage and current used in this study. For metallographic examination, 2 or 3 transverse cross-sections were taken from each welded joint. The specimens were then mounted and subsequently ground and polished using automated processes. Specifically, the weld samples were ground using successively fine SiC papers from 220 grit to 1200 grit and then polished using 3 and then 1 µm diamond suspensions with an alcohol-based lubricant on silk polishing cloths.

Table 6-2 Process parameters used in the narrow groove

Trial #	**Power (kW)**	**Laser-arc distance D (mm)**	**WFS (m/min)**	**Voltage (V)**	**Current (A)**	**Preheat (°C)**
1	15	N/A (only laser)	12	-	-	45
2	15	15	12	23	206	25
3	15	19	12	24	191	45
4	15	19	12	18.6	240	90
5	14	25	12	22.1	290	45
6	12	19	12	20.2	231	45
Filling passes	5.2	2	21	26	300	120

Villela's reagent (1 g picric acid, 4 mL HCl, 96 mL ethanol) was used to reveal the general microstructure and Beraha's reagent (1 g K2S2O5 + 20 ml HCl + 80 ml H2O) was used to reveal the martensite and delta ferrite phases in the microstructure. The microstructure was observed with an inverted optical microscope (OM) (Olympus GX71).

Flat tensile specimens with dimensions shown in Figure 6-2a, were extracted transversely to the welding direction. The top and bottom surfaces of the joint were machined to remove reinforcement, underfill and any discontinuity on surface. Two transverse tensile samples from the top and two from the root of the fully-penetrated joint were extracted, with the weld located at the centre of the gauge section, according to ASTM E8 standard. One Charpy impact test specimen was extracted from each of the two welds with only root pass (trials # 3,4) with the notch located in the fusion zone, according to ASME Section VIII [8] standard. The Charpy V-notch impact test specimens, extracted from the weldments at root side, were machined with geometry of 55 mm × 10 mm × 10 mm and a 2-mm deep V-notch in the FZ through the thickness, as depicted in Figure 6-2b. The Charpy impact tests were conducted at -18°C using a weighted pendulum hammer. A Hitachi SU8230 FE-SEM (scanning electron microscope) equipped with an EDS (energy-dispersive X-ray spectroscopy) system was used for analysis of the metallographic specimens as well as for fractographic characterization of the fractured tensile and Charpy specimens.

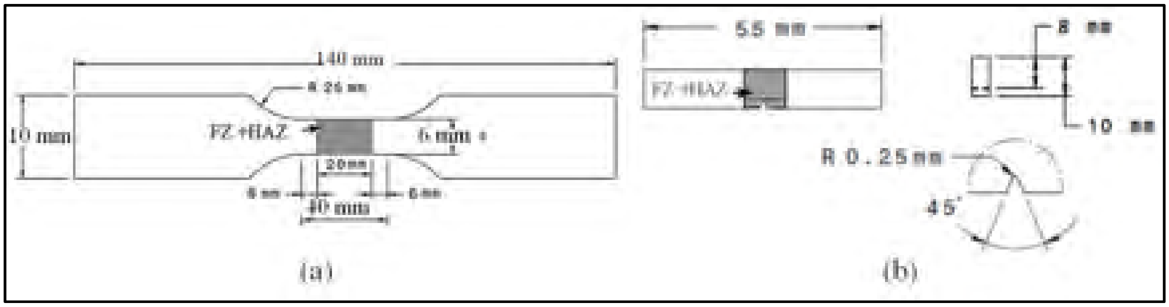

Figure 6-2 Specimen geometries for (a) transverse tensile and (b) Charpy impact tests

6.3 Results and discussion

6.3.1 Thermal cycles

Figure 6-3 shows the thermal cycles measured in the FZ (attached to the root hump) and HAZ (~1.5 mm away from the fusion line) for trial #6 (tandem laser-arc welding at 12 kW laser power). The cooling rate over the 800^{o}C-500°C range was ~40°C/s in the FZ and ~47°C/s in the HAZ with maximum temperatures of 1372°C and 1022°C, respectively. The results show that the maximum temperature experienced during welding can slightly affect the cooling rate (T 8/5), i.e. the higher the maximum temperature experienced, the lower the cooling rate. Comparing this result with that of TLAW at 5.2 kW laser power (Chapter 5), a great reduction in the 800-500°C cooling rate is observed from ~260°C/s at 5.2 kW laser power to ~47°C/s at 12 kW. This noticeable difference in cooling rate is mostly related to the laser power used. Lower cooling rates can be beneficial in reducing thermal gradient and thermal stress and strain gradients during welding, and residual stresses after welding [9].

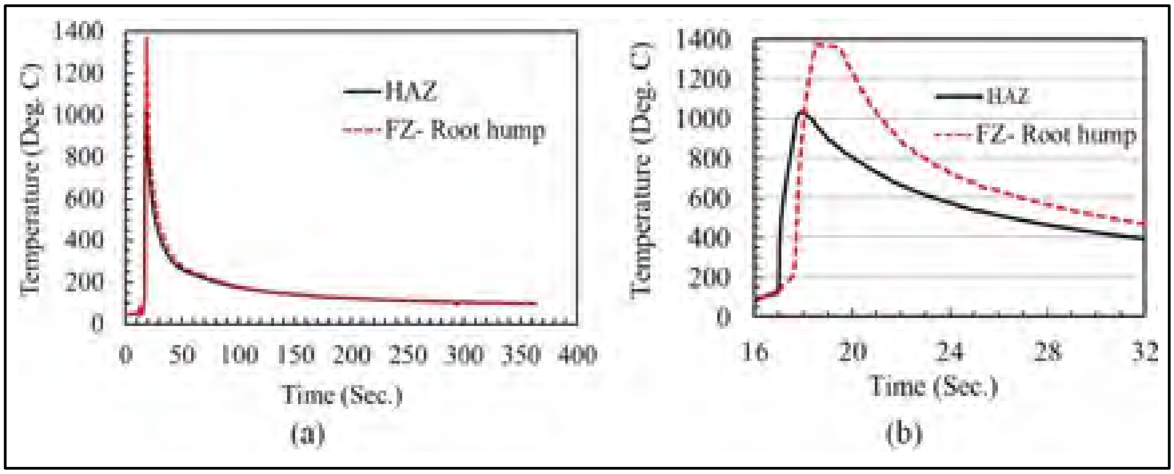

Figure 6-3 Thermal cycles for root pass weld # 6 (a) at different maximum temperature, (b) higher magnification from 16 s to 32 s

6.3.2 Root pass geometry and macrostructure

Figure 6-4 illustrates the top and bottom surfaces of the root passes assembled at different laser-arc distances and laser powers as listed in Table 6-2. Figure 6-4a-b show the top and bottom surfaces of the laser only root pass (without filler metal addition) inside a narrow-gap groove, using 15 kW laser power, which indicates a wavy surface on the top and bottom. Figure 6-4c-d display the top and bottom surfaces related to the coupled laser-arc welding with 15-mm laser-arc distance and 15 kW laser power, which revealed the periodic hump at the root surface. In Figure 6-4e-f, the laser-arc distance is increased to 19 mm which displays more uniform top surface, as compared to trial #2 (at 15-mm laser-arc distance), but a wavy surface with severe underfill at the bottom was observed. In trial #4 (Figure 6-4g-h) the laser-arc distance was kept at 19 mm (similar to trial#3), the preheat temperature was increased to 90 °C and the results show again severe underfill at the bottom. When increasing the laser-arc distance to 25 mm at 14 kW laser power, some blowholes were observed at the top surface with severe underfill at the bottom. Reducing further the laser power to 12 kW and keeping the laser-arc distance of 19 mm (Figure 6-4k-l), promoted a more uniform top surface with less metal loss and underfill at root side. However, the variation in the root stability was observed throughout the weld length, the root humping was observed randomly, and metal droplets were ejected from the back of the root at some locations.

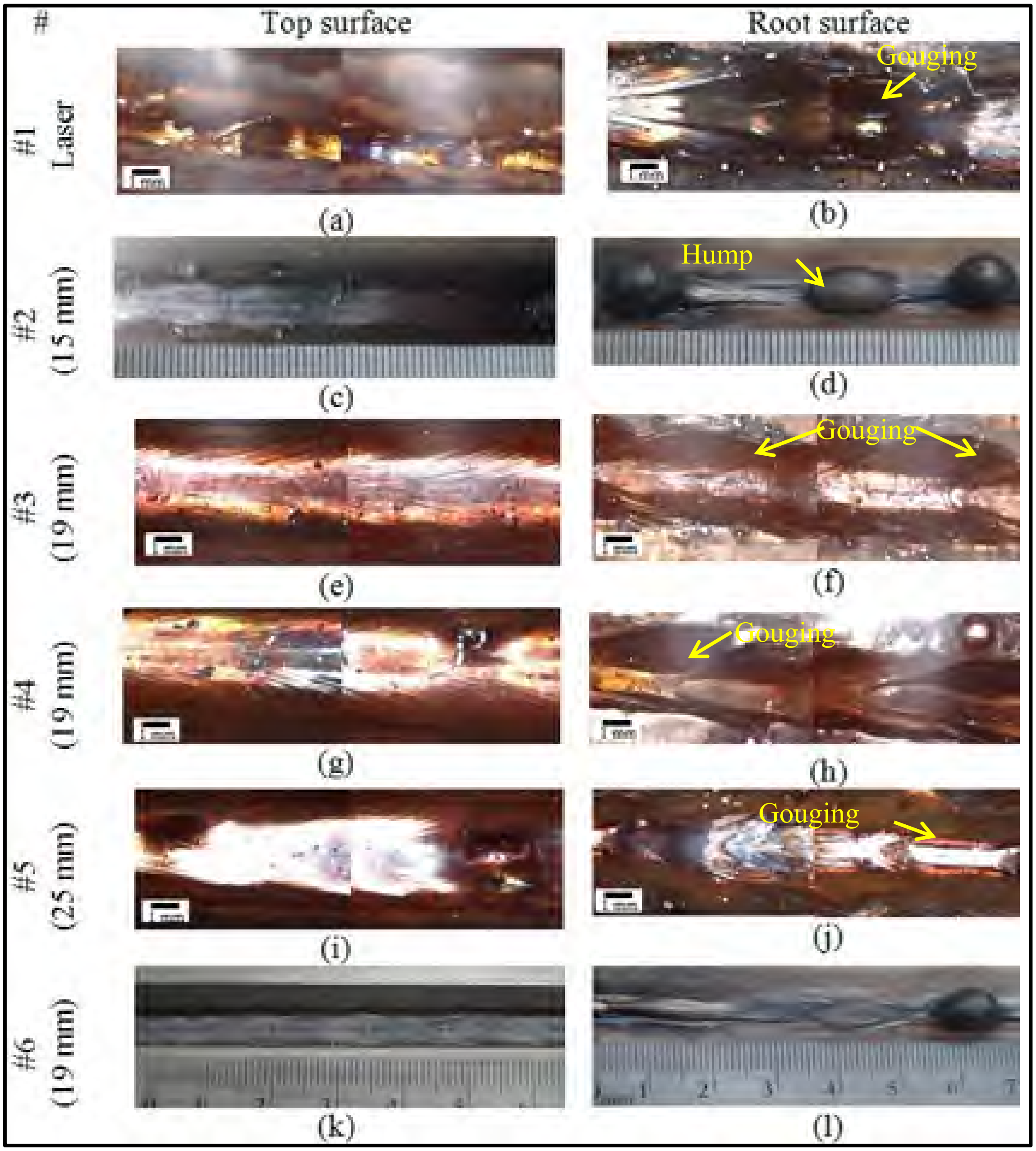
#
Top surface
Root surface
#1 Laser
Gouging
(a)
(b)
#2 (15 mm)
Hump
(c)
(d)
#3 (19 mm)
Gouging
(e)
(f)
#4 (19 mm)
Gouging
(g)
(h)
#5 (25 mm)
Gouging
(i)
(j)
#6 (19 mm)
(k)
(l)

Figure 6-4 Weld root surfaces at different laser powers, and hybrid or tandem laser-arc welding

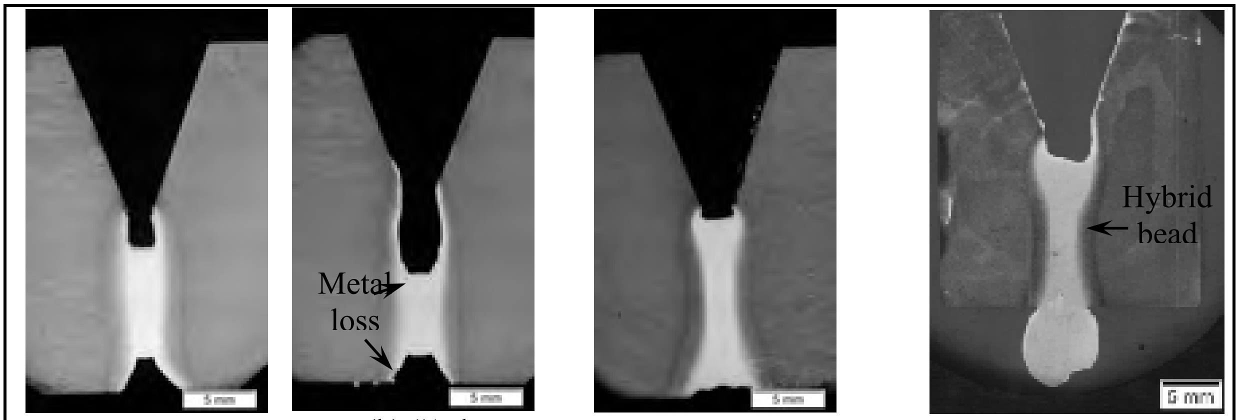
5 mm
Metal
loss
5 mm
5 mm
Hybrid
bead
5 mm

(a) #1 : laser (b) #1: laser (c) #1 : laser (d) #2 : D= 15 mm

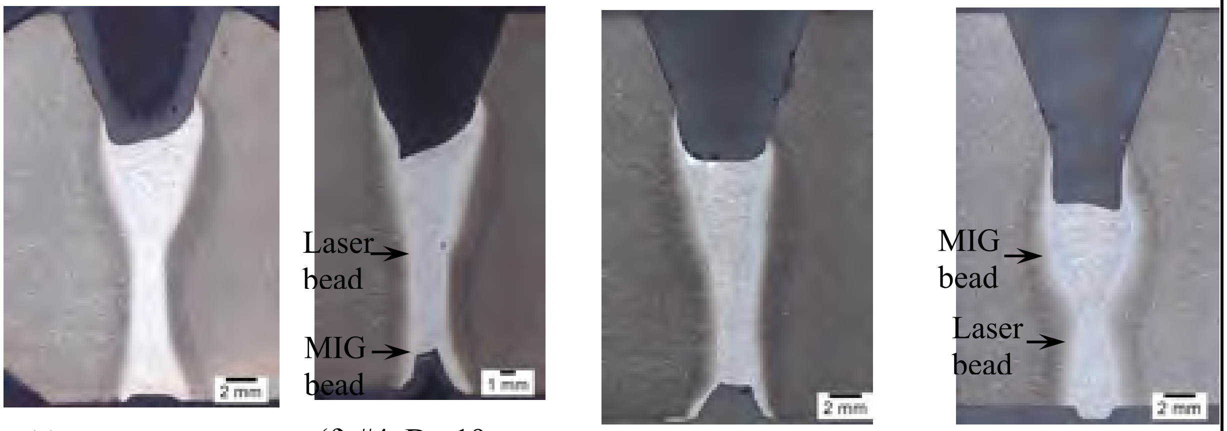
2 mm
Laser
bead
MIG
bead
1 mm
2 mm
MIG
bead
Laser
bead
2 mm

(e) #3, D= 19 mm (f) #4, D= 19 mm (g) #5 D= 25 (h) #6

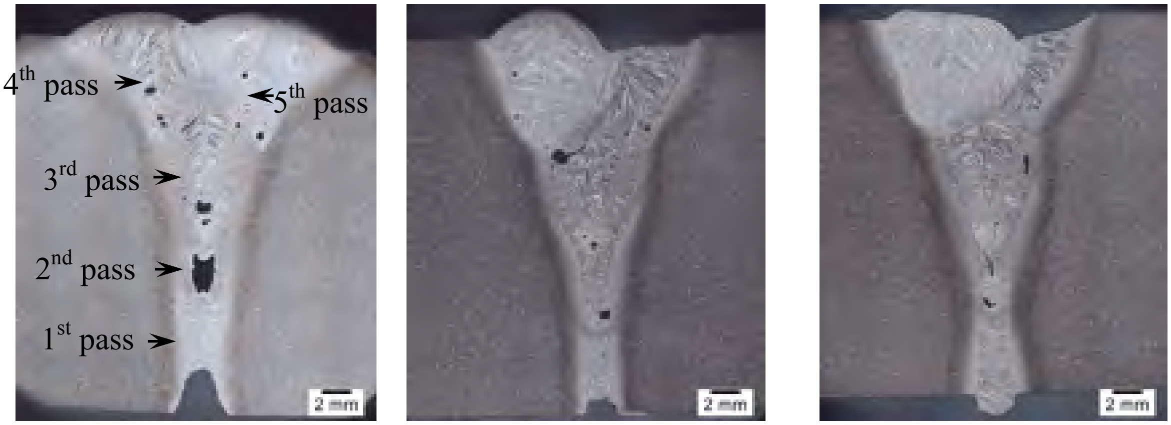
4th pass
5th pass
3rd pass
2nd pass
1st pass
2 mm
2 mm
2 mm

(i) Full join (j) Full joint (k) Full joint

Figure 6-5 Transverse sections of the welds manufactured at different welding conditions: (a-c) for the laser root pass, (d) hybrid, trial #2, (e-h) tandem trial #3-6, (i-k) full joint

The surface fluctuation and repeated swelling on top and bottom surfaces of the welds have probably formed during keyhole formation on the liquid surface and preserved after solidification and will be discussed in detail further.

To better understand and analyze the variation in root weld stability during high power laser and laser-arc welding, the transverse sections of the welds were studied as demonstrated in Figure 6-5. Three different cross-sections extracted from laser-only root passes (i.e. without the arc and filler metal addition) are displayed in Figure 6-5a-c. The weld transverse sections of the root passes at laser-arc distances of 15 mm revealed a unique molten pool as shown in Figure 6-5d which is called hybrid bead. With increasing laser-arc distance to 19 mm and 25 mm (Figure 5e-h) at different laser powers and preheating temperatures (Table 6-2), two distinct weld pools were observed, one related to the laser and the other corresponding to the GMAW bead. This kind of process is called tandem laser-arc welding (TLAW). It is noted that a good overlap between the laser and GMAW weld beads was observed in tandem mode using 15 kW and 12 kW laser power with Y-shaped narrow-gap groove configuration. Compared with the results obtained in Chapter 5, no lack of fusion between the laser and GMAW beads were observed, even though the laser-arc distance was higher (19 mm). This is mainly due to the increase of the groove included angle from 27° to 40° and of the laser power from 5.2 kW to 12 kW. As discussed in Chapter 5, a larger groove can promote downward molten metal flow and minimise the risk of lack of fusion. Beside, higher laser power (with lower cooling rate) leads to a higher temperature of the laser bead just in front of the GMAW molten pool which can act as a preheating for GMAW bead and thus increase the penetration depth.

The transverse sections of the laser root passes (Figure 6-5a-c) display variation in FZ depth and different levels of metal loss from top and bottom surfaces. This variation is attributed to the wavy surfaces observed on the top and bottom surfaces in Figure 6-4a-b. During laser root pass welding, the laser with a high power density (~ 5.9×10^6 W/cm^{-2}) heats the material to a temperature up to the boiling point and leads to an intense metal evaporation and formation of a vapour capillary through the material, which is so-called keyhole effect. A strong pressure forms due to the metal evaporation which is called recoil pressure [10]. The keyhole is kept open by the pressure balance, mostly between recoil pressure and surface tension on the keyhole wall. This high recoil pressure can generate high velocity melt flow. Under high velocity melt flow, the keyhole cannot be fully stable. Any perturbation in recoil pressure can lead to the oscillation of the molten metal in the weld pool and induce waves on the melt surface [11]. The simulation of the weld pool during laser keyhole welding by Mazumder et al., 2002b [12] demonstrated that the entire melt pool around the keyhole is highly pressurized due to recoil pressure and makes the rear end of the keyhole swollen. He also demonstrated that the effective absorptivity of the laser changes during laser keyhole welding after the full penetration which can be associated with variation in recoil pressure, keyhole fluctuation and consequently the formation of a wavy surface after solidification. So the location where the top surface becomes deepened (Figure 6-5b) is related to the surface with high local laser absorptivity and consequently high recoil pressure during welding. According to several researches this fluctuation and instability in keyhole and recoil pressure are an intrinsic phenomenon that exists all the time even under constant laser power [13]. However grooving or gouging at the root surfaces observed during both laser and tandem laser-arc welding (marked as gouging) is related to the loss of material (detachment of droplets) during laser and arc-laser welding. This was confirmed by observing the metal droplets solidified inside the root shielding gas channel. This root gouging is observed as a deep root underfill in transverse sections (Figure 6-5 a,b,f). Some part of this metal loss is due also to the evaporation during keyhole welding at high laser power density. Further ejection of the metal droplets from the bottom and top of the weld pool is due to the recoil pressure induced by the metal vapors in the keyhole. The ejection of metal droplets occurs when the vapor recoil pressure exceeds the surface tension pressure of the liquid metal at the boundary of the weld pool [14]. This observation shows that the welding process almost evolves into a gouging/cutting process instead of welding, specifically at the top and bottom surfaces. This observation is compatible with the simulation model performed by Otto et al [15] during keyhole laser welding and cutting where a high recoil pressure can lead to the blowout and detachment of molten droplet from both the top and bottom of the workpiece (Figure 6-6). This phenomenon mostly happens during laser cutting. Since the driving force is recoil pressure, similar phenomenon can also occur during deep penetration laser welding process.

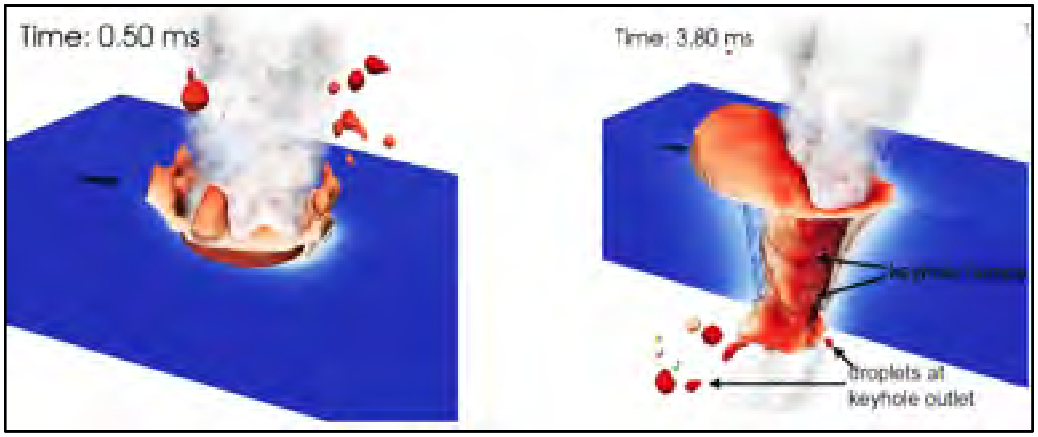

Figure 6-6 Vapour pressure cutting simulation using laser power [15]

During TLAW, the fluctuation in root surface exists at different laser-arc distances (Figure 6-4f,h,j,l), which is due to the predominating effect of the laser heat source on the root side. Reducing the laser power to 12 kW could be helpful in sustaining a more stable root, probably due to the reduction in laser power density, since the peak temperatures and molten metal velocity increased significantly with increasing laser power. This can also reduce the metal evaporation and consequently the recoil pressure and metal ejection. However, it is important to use appropriate parameters to assure (1) the pressure balance (mainly caused by surface tension and recoil pressure) in the keyhole boundary and (2) full penetration in root sides. Assuring pressure balance during deep keyhole welding and full penetration without defect is quite challenging due to the intrinsic fluctuation in pressure balances at the keyhole. Further study is required in this area.

Root humping was observed in trial #2 (at a laser-arc distance of 15 mm) constantly and trial #6 (TLAW root pass welding at 12 kW laser power) randomly. The liquid metal at the bottom of the root tends to drop-out, pushed by gravitational forces when the surface tension cannot balance the vapour pressure at the wall of the molten metal. Moreover, thermocapillary convection is very strong on upper and lower sides of the weld pool inducing large convective velocities and destabilizing the weld pool surfaces [16].

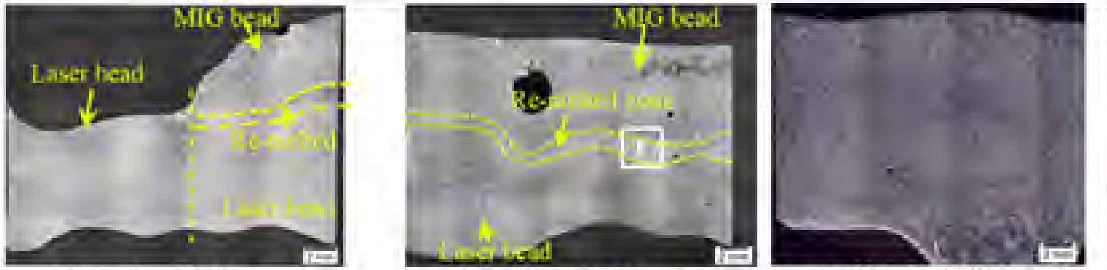
MIG bead
Laser bead
Re-melted
Laser bead
MIG bead
Re-melted zone
I
Laser bead

(a) Tandem D: 25 mm (b) Tandem, D: 19 mm (c) Hybrid D: 15 mm

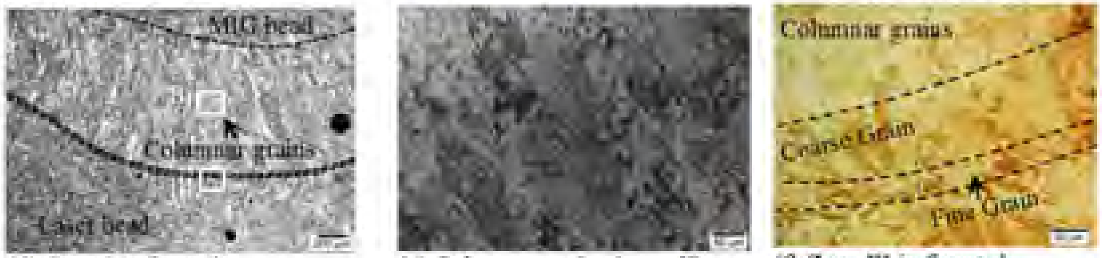
MIG bead
Columnar grains
Laser bead
Columnar grains
Coarse Grain
Fine Grain

(d) Zone I in figure b (e) Columnar grains (zone II) (f) Zone III in figure d

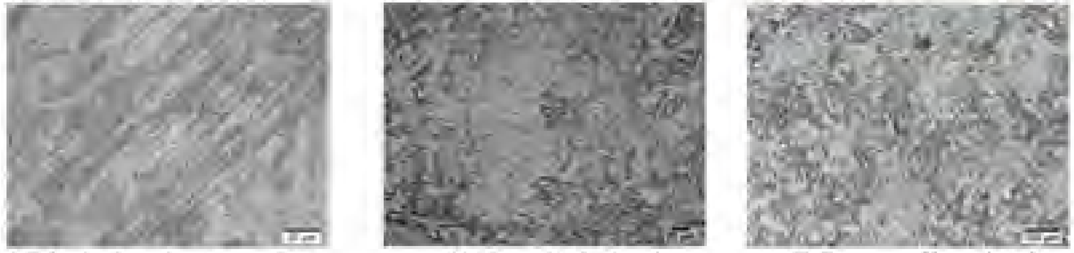

(g) δ ferrite in columnar grains (h) Top of MIG bead (i) Bottom of laser bead

Figure 6-7 Longitudinal cross-section of the root pass welds at different laser-arc

To better understand the interaction between laser and arc during TLAW of the root pass, the longitudinal sections of the weld for laser and TLAW at 25 mm laser-arc distance is displayed in Figure 6-7a. Figure 6-7b shows the longitudinal section for TLAW at 19 mm laser-arc distances (extracted form the end of the weld run) and Figure 6-7c for HLAW at 15 mm laser arc distance. The laser bead in Figure 6-7a, shows a periodic surface at both top and bottom as observed in Figure 6-4a-b. Two separated GMAW and laser weld beads could be observed at both 25 and 19 mm laser-arc distances.

As mentioned previously, there was a good overlap between the GMAW and laser beads, beside the GMAW bead healed the discontinuity at the laser top surface. These observations suggest that, welding in tandem mode compared to hybrid mode in thick plates, can help to reduce the root humping defect by decreasing the effect of gravity forces induced at the bottom of the root pass and help to achieve a more stable bead surface.

A narrow columnar grain zone ~1.2 mm wide was observed between the laser and GMAW beads (Figure 6-7d, e). These columnar grains are related to the re-melted zone by the second pass and demonstrate the depth of the overlap between two passes. Within these columnar grains, the residual delta ferrite was observed at previous austenite grain boundaries (Figure 6-7i). These stringers of delta ferrite are related to FZ microstructure as discussed in Chapter 4. A very narrow zone of fine grains was also detected adjacent to the coarse grain zone in the FZ of the laser bead which is related to the high temperature dual phase HAZ of ($\delta + \gamma$) region.

6.3.3 Defects

In addition to the visual imperfection of defects such as humping and severe root underfill during TLAW and HLAW, most of the defects observed in transverse sections of both root and filling passes were porosity and cracks.

The big porosities with irregular shape were formed mostly during filling passes at the bottom of each pass. Figure 6-8 a,b shows the porosity at the bottom of the second and third passes respectively during HLAW (Figure 6-5i, k). These irregular shaped porosities can reach a few millimetres in diameter and their formation is mainly due to the keyhole collapse that creates a closed space at the bottom of the keyhole where bubble and vapour can be trapped there. Lu et al. simulated keyhole-induced porosity formation mechanism during deep laser welding [17] and explained that the violent flow along the keyhole walls can lead to the formation of a liquid bridge, which causes a closed space at the bottom of the keyhole which cannot be refilled before solidification. Moreover in our study, the violent flow could also be enhanced due to the high wire feed speed of 21 m/min used during HLAW filling passes. Decreasing the wire feed rate during HLAW of filling passes can help reducing the porosity.

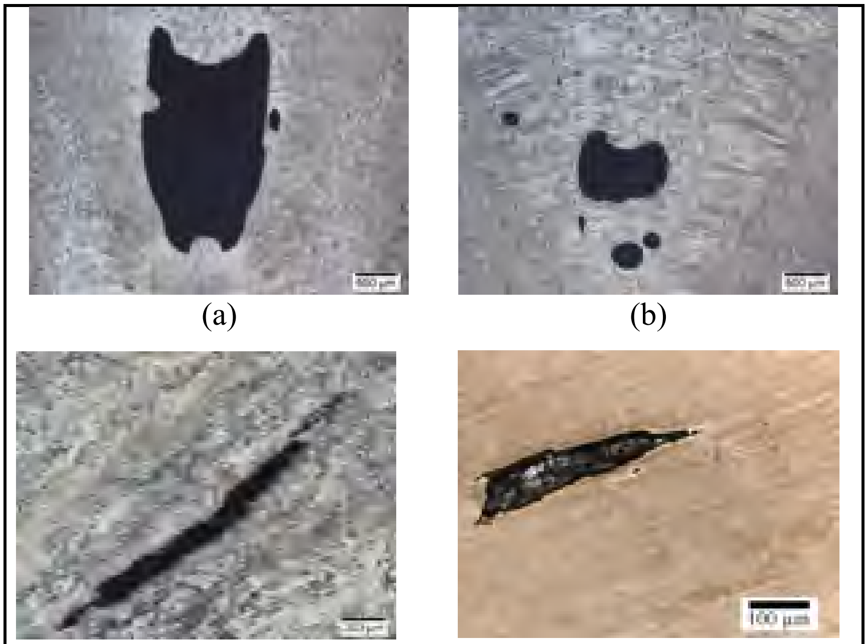

(a) (b)

(c) (d)

Figure 6-8 Defects observed in the weld cross-sections: (a,b) porosity at the bottom of second and third passes , (c,d) crack in the filling passes

Cracking was another defect observed in tandem root pass (inside GMAW bead) and hybrid filling passes (in top part of the bead) as shown in Figure 6-8c-d. These cracks lie predominately along the weld solidification direction. The cracks seem to propagate within the martensite structure and are aligned with the heat flow and growth direction. To better understand the mechanism for crack initiation and formation, an EDS chemical analysis near the tip of a crack was performed (Figure 6-9). The results show the high concentration of (C, Mo) and (Cr, O) at the edge of the crack which indicates the presence of chromium oxide and molybdenum carbide at the start and edge of the crack. This observation implied that the crack initiated at the interfaces or boundaries between the martensitic matrix and the carbides or oxide inclusions. It is possible that the oxide and carbide particles originate from slags and are entrapped in the solidifying columnar structure during welding. The carbide and oxide particles could induce a loss of ductility of the matrix which under the thermal stresses caused by welding was more sensitive to cracking.

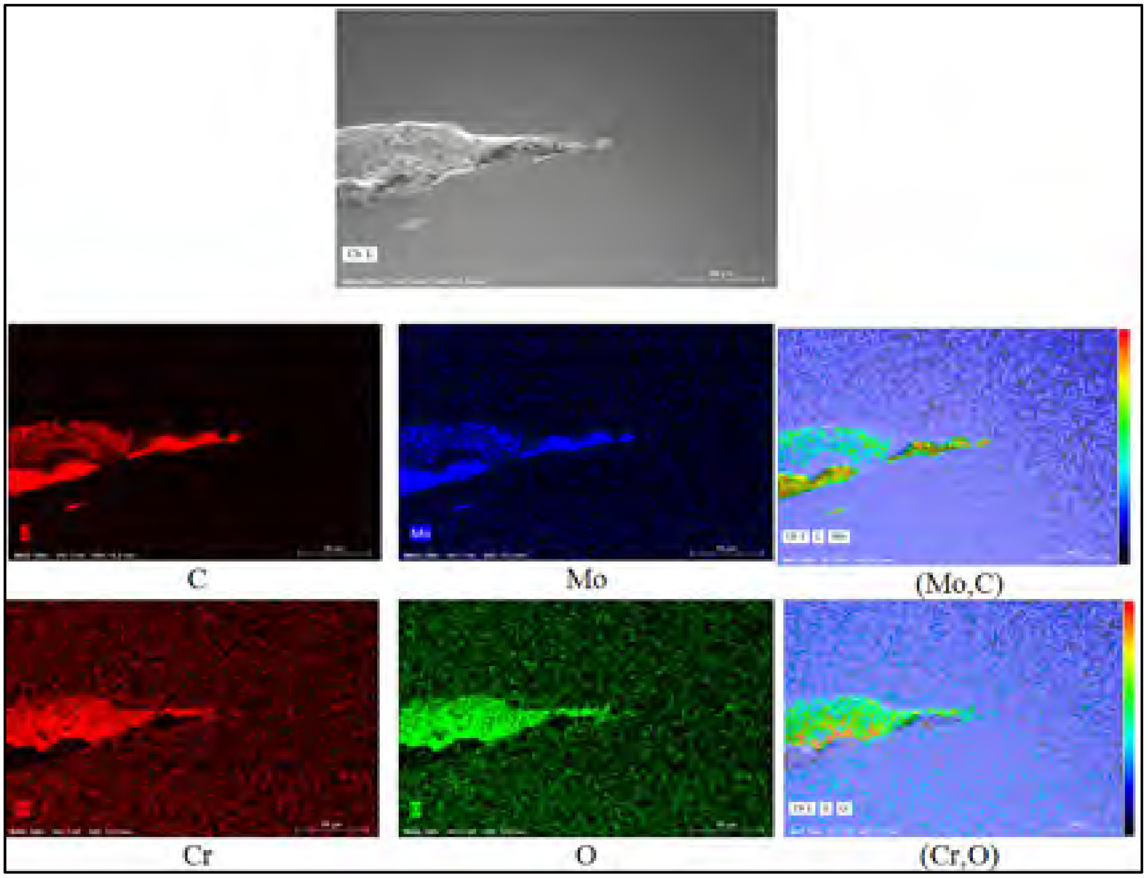

Figure 6-9 SEM-EDS mapping of the elemental distribution near the crack

6.3.1 Tensile tests

Transverse tensile properties such as ultimate tensile strength (UTS), yield strength (YS) and percentage of elongation (El. %) were evaluated for the bottom part of the full joint (related to pass 1,2) and top part of the full joint (related to pass 3-5) in as-welded condition and are presented in Table 6-3. The tensile properties display a higher value at the joint top compared to the joint bottom. Considering that the UTS, YS and El. % required in ASTM A743 standard are 755 MPa, 555 MPa and 15%, respectively, the transverse tensile properties at the top of the weld in as-welded condition met the specification requirements. For the bottom of the weld, the UTS and YS could pass the requirement sufficiently but the El. % for the weld bottom (8%) was noticeably lower than the minimum requirement of 15%.

Table 6-3 Tensile property of the full joint respectively at the top and bottom of the weld

Full joint	UTS (MPa)	YS (MPa)	El%	Failure location
Specification values	≥ 755	≥ 555	≥ 15	N/A
Top	872	734	19	BM
Bottom	779	730	8	FZ

To understand the failure mechanisms, the crack propagation path (Figure 6-10) and fracture surface (Figure 6-11) at both the top and bottom of the joint were analysed. The results indicated that for the bottom weld tensile sample, the fracture occurred within the FZ (Figure 6-10a) and for the top weld tensile sample, the fracture happened in the BM (Figure 6-10f). In the bottom weld fracture surface, several macro porosities were observed both inside the FZ (Figure 6-10a) and on the fracture surface (Figure 6-11a). These porosities are mainly related to keyhole collapse which was also detected in the bottom of the second and third passes in metallographic cross-sections (Figure 6-8a,b). The high amount of defects in the weld bottom part is the main reason for propagation of the crack inside the FZ. In addition to the porosity formed during welding (Figure 6-10b), elongated pores were newly formed near the fracture surface during tensile loading (Figure 6-10c). This was also observed in HLAW of 10 mm thick cast martensitic stainless steel [18]. A secondary crack was also observed in FZ near the failure location which propagates intergranularly between prior-austenite and packet grain boundaries (Figure 6-10d,e). The fractography examination also showed the evidence of grain decohesion during tensile fracture as displayed in Figure 6-11b which can be attributed to packet or prior-austenite grain boundaries as-well.

Fracture analysis for the top weld showed that the failure took place in BM, in spite of some porosity and longitudinal crack in FZ. This can be due to the fact that the area fraction of defect in FZ at the weld bottom was notably higher to that of the filling pass at the weld top. The growth of pre-existing pores was observed near the failure location in BM (Figure 6-10h,i), these pores grow and coalesce during tensile loading.

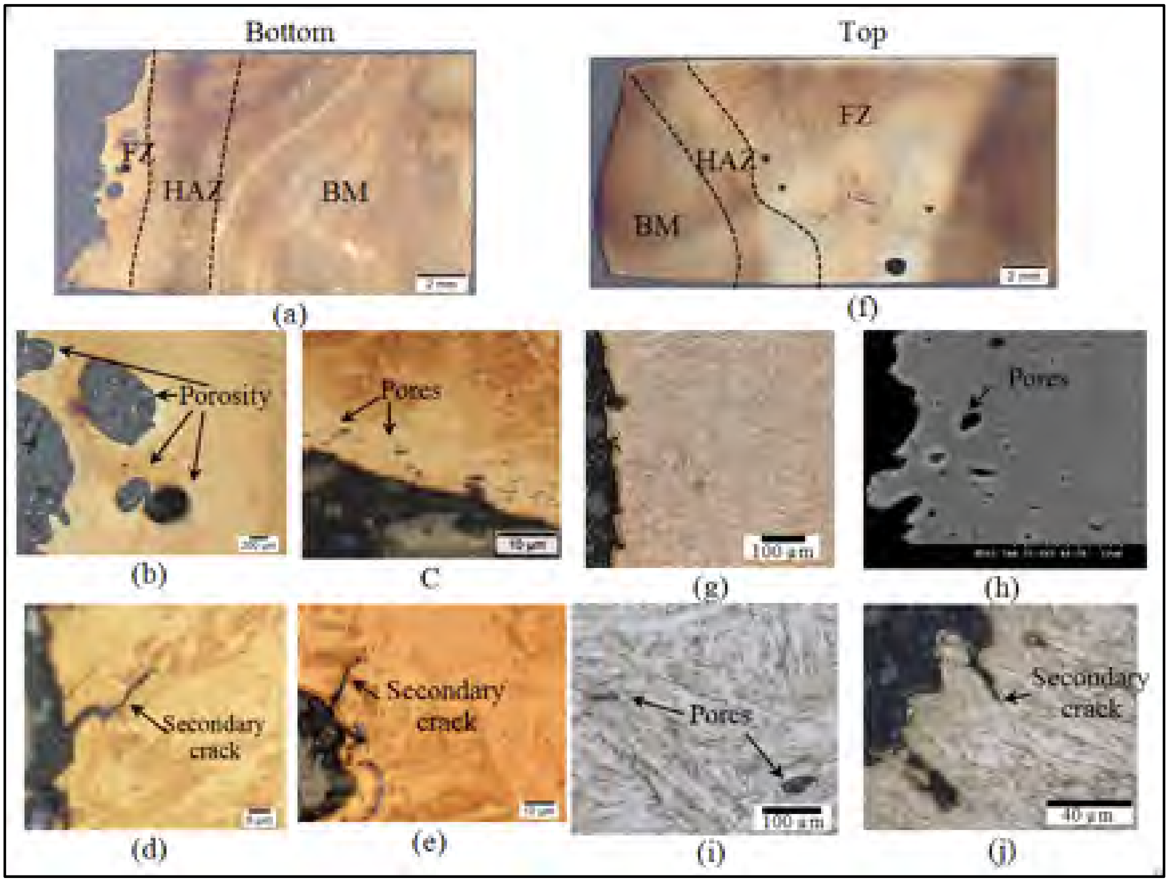
Bottom
Top
FZ
HAZ
BM
2 mm
(a)
FZ
HAZ
BM
2 mm
(f)
Porosity
(b)
Pores
C
100 µm
(g)
Pores
(h)
Secondary crack
(d)
Secondary crack
(e)
Pores
100 µm
(i)
Secondary crack
40 µm
(j)

Figure 6-10 Microstructure near the tensile fracture surface of the weld at bottom (left side in figures (a-e) and top (right side in figures (f-j) of the joint

This was also observed previously in transverse tensile testing of CA6NM HLAW, when the fracture occurred in BM (Chapter 3). The fracture propagated predominantly within the martensite in BM. Several secondary cracks, formed during tensile loading, were also observed in the fractography (Figure 6-10j). The fracture surface in the top weld tensile sample was typical of dimple-mode ductile fracture (Figure 6-11f), while for the bottom weld, a mixture of both dimple and cleavage fracture could be observed (Figure 6-11c).

6.3.2 Charpy impact property

The Charpy impact energies in the FZ of the tandem root passes at 19-mm laser-arc distance and two different preheating temperatures are listed in Table 6-4. The results show an increase in impact energy value from 88 J to 162 J with increasing preheat temperature from 40 °C to 90 °C.

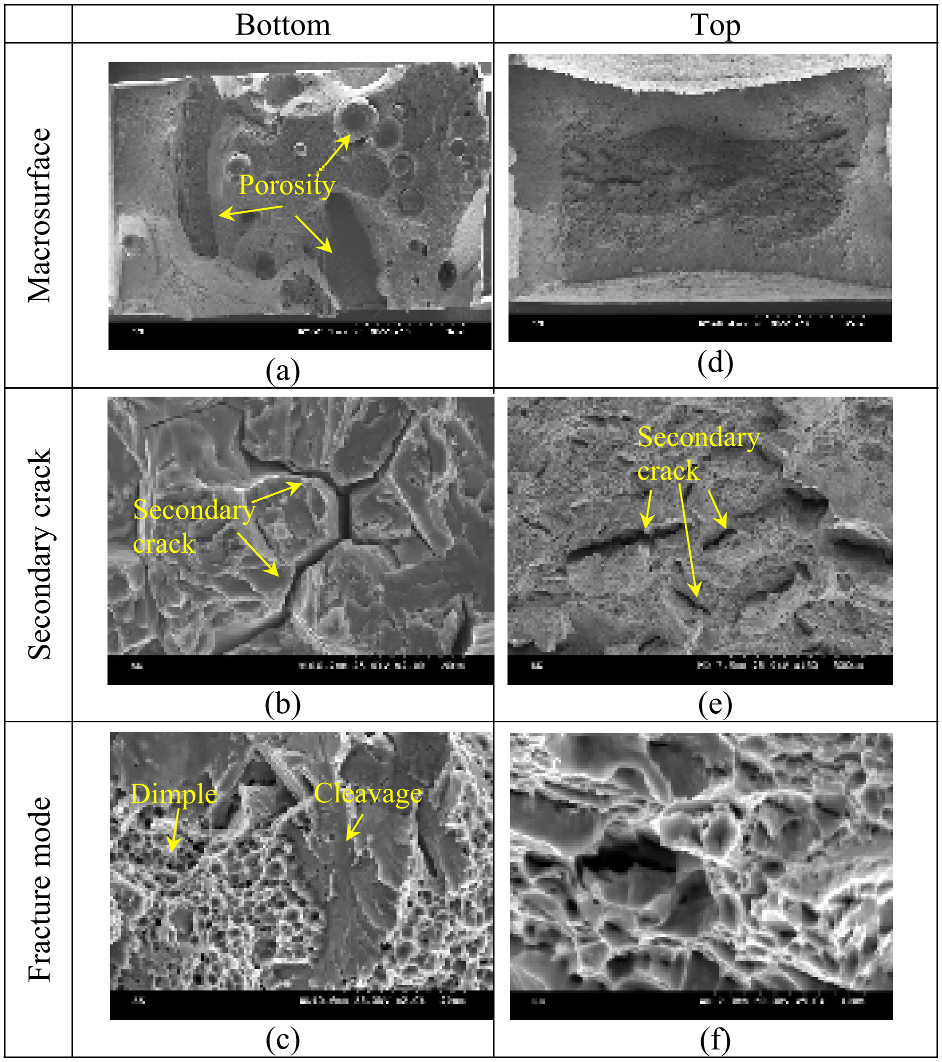
Bottom
Top
Macrosurface
Porosity
(a)
(d)
Secondary crack
Secondary crack
(b)
Secondary crack
(e)
Fracture mode
Dimple
Cleavage
(c)
(f)

Figure 6-11 Tensile fracture surface of the weld at bottom (a-c) and top (d-f) of the full joint

To investigate the reason for the significantly-scattered results, the fracture path during Charpy impact test for both samples was examined as demonstrated in Figure 6-12. For the sample with 40 °C preheating, the fracture took place within FZ (Figure 6-12a) but for the weld with 90 °C preheating the crack initiated from the notch in FZ and deviated to HAZ and then BM (Figure 6-12b).

Table 6-4 Impact energy of the 415 SS root pass at two different preheating temperatures

Full size Charpy test	**Charpy impact energy (J)**	**Fracture path**
Specification values	≥ 27[I]; ≥ 34[II]	-
TLAW, 40 °C preheating (#3)	88.0	Within FZ
TLAW, 90 °C preheating (#4)	162.0	From FZ to BM

[I]ASME Sect. VIII Div.1, [II]ALSTOM industrial specification.

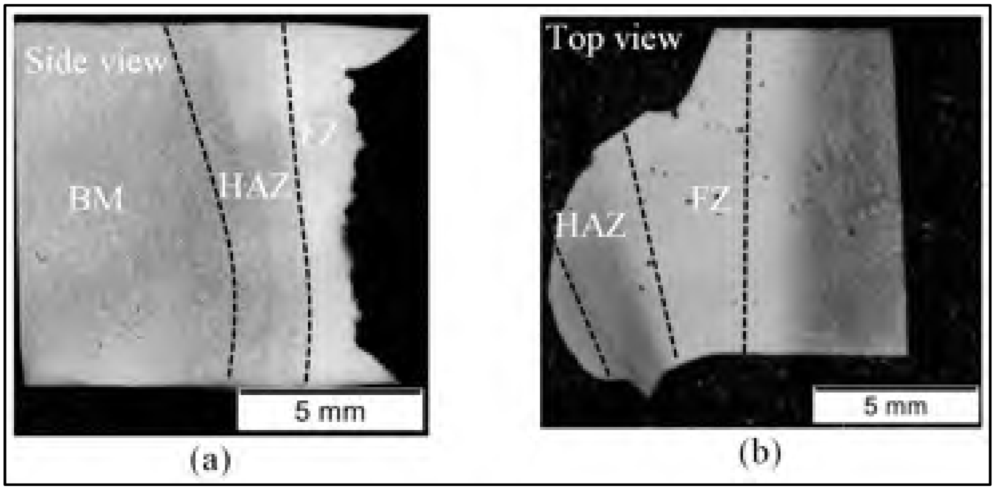

Figure 6-12 Fracture direction after Charpy impact test: (a) trial #3, and (b) trial #4

Therefore, the impact value for the tandem root pass with 90 °C preheating temperature is not truly representative of the properties of the FZ due to the fracture path deviation (FPD) phenomenon happening during the Charpy impact testing and the impact energy value is a mixture of the property in the FZ, HAZ and BM. FPD was also observed during laser welding of steels [19, 20] and was attributed to the narrow FZ and HAZ in laser weld and mismatch between the weld metal and BM hardness and strength. Since the strength of FZ is usually higher than that of BM in a defect-free weld, a crack propagating in a narrow FZ can deviate into the softer zone (BM). Figure 6-13 shows the general overviews of the Charpy impact fracture surfaces for the tandem root pass with different preheating temperatures. The

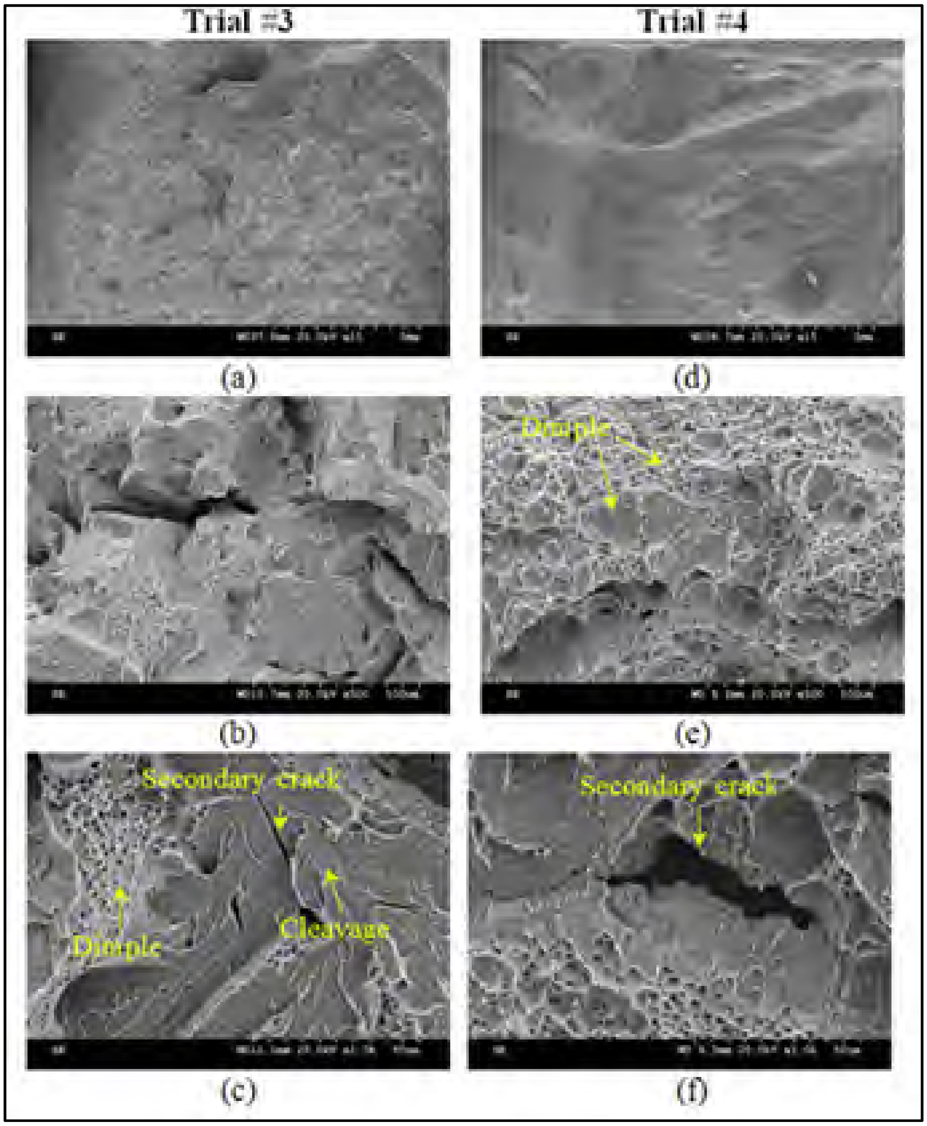
Trial #3
Trial #4
(a)
(d)
Dimple
(b)
(e)
Secondary crack
Dimple
Cleavage
Secondary crack
(c)
(f)

Figure 6-13 Charpy fracture surfaces of root pass: trial#3 (a-c) and trial #4 (d-f)

fracture surface topography of the weld with 45 °C preheating (fractured within FZ) exhibited a mixture of both dimple and quasi-cleavage (Figure 6-13b,c). Some secondary sharp cracks were also observed propagating between the cleavage facets (Figure 6-13c) during impact testing. For the tandem root weld at 90 °C preheating, showing FPD, the fracture surface displayed predominately dimple mode ductile fracture surface (Figure 6-13e) which is a mixture of the fine and coarse dimples. These dimples result from the formation and coalescence of microvoids. Some secondary cracks were also observed within the coarser dimples (Figure 6-13f). These cracks probably formed due to debonding of secondary phases, carbide or inclusions, from the matrix [21].

6.4 Conclusions

1. The root pass after laser welding at 15 kW laser power, displayed a wavy surface at both the bottom and top surface which formed on the liquid surface before solidification. During high power laser welding, an intense metal evaporation leads to high recoil pressure which can generate a high velocity melt flow and fluctuations of the weld surface. The severe underfill observed at the bottom surface is related to the metal ejection and loss of evaporative metal during high power laser welding.
2. At laser-arc distance from 15 mm to 25 mm, root humping was observed at 15 mm distance when the laser and arc formed a unique weld pool due to the effect of gravitational force and surface tension. With increasing laser-arc distance to 19 and 25 mm, periodic root humping (as observed in hybrid mode at 15 mm laser-arc distance) was no longer present; metal loss at the bottom surface was still substantial. Reducing the laser power down to 12 kW could help to sustain a more stable root probably due to reduced evaporation and recoil pressure. However, a fully stabilised TLAW or HLAW was not achieved yet due to the keyhole fluctuation. Using backing plates can be an alternative solution to protect the root side and avoid metal loss during keyhole laser welding.
3. Porosity and cracking were the main defects observed in transverse sections of the welds mainly in the filling passes using HLAW at 5.2 kW laser power. The large pores were formed predominately at the bottom of each filling pass due to the

collapse of the keyhole and the entrapment of vapour or shielding gases. The keyhole instability was enhanced due to very high wire feed rate. Longitudinal cracking was formed mainly at the interfaces between carbide or oxide inclusions and the martensitic matrix.

4. The tensile properties display a higher value at the top part of the weld as compared to the bottom part. The ultimate tensile and yield strength at the top and bottom of the weld could pass the minimum requirement (ASTM A743). Although the elongation for the weld bottom was lower than the minimum requirement (15%), the top weld elongation (19%) could pass the minimum value. The transverse tensile samples at top and bottom failed in the fusion zone and base metal, respectively during tensile loading. Microstructural analysis near the failure location showed the presence of large pores inside the narrow FZ at the weld bottom with the crack propagating intergranularly between prior-austenite and packet grain boundaries.
5. The Charpy impact energy for the tandem root pass at 40 °C preheating was 88 J which was quite higher than the minimum requirement of 34 J required by the turbine manufacturer, probably due to the high integrity weld and very low carbon content of the 415 SS base metal. Mixed dimple-quasi cleavage fracture modes were observed with secondary cracks being present at cleavage facets. For the weld at 90 °C preheating the fracture path deviation took place with the crack initiating at FZ and deviating from FZ to BM, leading to an increased impact value of 162 J. The fracture surface was a mixture of fine and coarse dimples with secondary cracking within the coarse dimples.

Acknowledgments

The authors are grateful to Alstom, Hydro-Québec, National Science and Engineering Research Council of Canada (NSERC) for the financial supports and NOVIKA Company for their technical supports. The authors also wish to thank E. Poirier and X. Pelletier of NRC Aerospace and for their technical assistance during welding and metallographic preparation

References

1) K. Devakumaran, M. Ananthapadmanaban, P. Ghosh, Defence Technology, 11 (2015) 147-156.
2) V. Semak, A. Matsunawa, Journal of physics D: Applied physics, 30 (1997) 2541.
3) H. Ki, J. Mazumder, P.S. Mohanty, Metallurgical and materials transactions A, 33 (2002) 1817-1830.
4) C. Bagger, F.O. Olsen, Journal of laser applications, 17 (2005) 2.
5) P. Kah, A. Salminen, J. Martikainen, Mechanika, 3 (2010) 68-74.
6) P. Kah, Reviews on Advanced Materials Science, 30 (2012) 112-132.
7) M. Wahba, M. Mizutani, S. Katayama, Materials & Design, 97 (2016) 1-6.
8) Boiler, ASME, andPressure Vessel Code. 1983. « SECTION VIII, DIVISION ».
9) M. Zubairuddin, S. Albert, M. Vasudevan, S. Mahadevan, V. Chaudhri, V. Suri, Materials and Manufacturing Processes, 31 (2016) 366-371.
10) Matsunawa, V. Semak, Journal of physics D: Applied physics, 30 (1997) 798.
11) Semak, Vladimir, and Akira Matsunawa, Journal of Physics D: Applied Physics, 30.18 (1997) 2541.
12) H. Ki, J. Mazumder, P.S. Mohanty, Metallurgical and Materials Transactions A, 33 (2002) 1831-1842.
13) Matsunawa, Technical Report, Lecture Note from a Course Given at ICALEO, San Diego, CA, 1999.
14) X. He, T. DebRoy, P. Fuerschbach, Journal of Physics D: Applied Physics, 36 (2003) 3079.
15) Otto, H. Koch, K.-H. Leitz, M. Schmidt, Physics Procedia, 12 (2011) 11-20.
16) M. Bachmann, V. Avilov, A. Gumenyuk, M. Rethmeier, Journal of Physics D: Applied Physics, 45 (2011) 035201.
17) F. Lu, X. Li, Z. Li, X. Tang, H. Cui, International Journal of Heat and Mass Transfer, 90 (2015) 1143-1152.
18) F. Mirakhorli, X. Cao, X.-T. Pham, P. Wanjara, J.-L. Fihey, Metallurgical and Materials Transactions B, 1-12.

19) W. Guo, D. Crowther, J.A. Francis, A. Thompson, Z. Liu, L. Li, Materials & Design, 85 (2015) 534-548.

20) Bezensek, J.W. Hancock, ASME/JSME 2004 Pressure Vessels and Piping Conference, American Society of Mechanical Engineers, 2004, pp. 9-15.

21) W. Becker, S. Lampman, Materials Park, OH: ASM International, 2002., (2002) 559-586.

SUMMARIES

This thesis presented a study on the hybrid and/or tandem laser-arc welding of thick martensitic stainless steels, specifically low carbon 13%Cr-4%Ni stainless steel, as applied in hydroturbine manufacturing.

In the first step, single pass HLAW of 10-mm thick CA6NM stainless steel was performed successfully and the effect of different welding speeds (0.5-1.2 m/min) on microstructural and mechanical properties of the welds was investigated.

- The most common imperfections observed during single pass HLAW of 10-mm thick CA6NM were root humping, porosity, underfill and excessive penetration. Root humping was just observed at a welding speed of 0.5 m/min which was related to high heat input and unstable keyhole. Porosity and underfill were also observed at this welding speed, but were reduced with increasing welding speed. At welding speeds of 0.75 m/min and above, the maximum amount of underfill and excessive penetration complied with the acceptance criterion according to the ISO 12932 standard related to HLAW of stainless steels.

- Fusion zone microstructure in the as-welded condition consists of untempered lath martensite and residual delta ferrite with different morphology formed predominately at previous Widmanstätten austenite boundaries. After post weld tempering at 600 °C, the untempered martensite changed to tempered martensite in the fusion zone accompanied with the formation of reversed austenite and chromium carbides. The reversed austenite was formed mostly along the martensite lath and interlath boundaries, preferentially at triple junction of lathes. Reversed austenite formed after post weld tempering, maintained near Kurdjumov-Sachs orientation relationship with the martensitic matrix.
- Four different heat affected zones were identified and interpreted according to the Fe-Cr-Ni pseudobinary phase diagram based on metallographic observations and microhardness measurements. The HAZ2 consisted predominately of coarse untempered martensite,

while HAZ3 exhibited a refined untempered martensite and residual delta ferrite. HAZ4 also revealed predominately untempered martensite with possible fully or partially dissolution of chromium carbides, due to the high temperature experienced in single phase austenitic region. HAZ5 related to the low temperature dual phase region of martensite and austenite displayed a mixture of both tempered and untempered martensite. After post weld tempering the untempered martensite in the entire heat affected zone transformed to tempered martensite. The fine reversed austenite films were observed in HAZ2 to HAZ5 mainly along martensite laths boundaries and lath triple cross-sections. Chromium carbides e.g. M_7C_3 and $M_{23}C_6$ can also form after post weld tempering in HAZs.

- After post weld tempering, the microhardness in both the fusion zone and heat affected zones was reduced. The fusion zone experienced a reduction in microhardness from ~354 HV (as welded condition) to ~308.7 HV (in PWHTed condition). The maximum hardness happened in HAZ4, a single phase austenitic region near the HAZ3/HAZ4, both in as-welded (~376 HV) and post-welded condition (~320HV). The minimum hardness occurred in HAZ5, a low temperature dual phase region of martensite plus austenite, both in as-welded and post welded condition. The reduction in hardness in different zones after post weld tempering is mainly due to the formation of tempered martensite and reversed austenite
- The ultimate tensile strength both in as-welded and PWHTed conditions met the minimum requirement of 755 MPa according to the ASTM A743 specification, reducing from 950 MPa to 850 MPa after post weld tempering. Th tensile fracture happened in the base metal for all samples. The fracture analysis near the failure surface reveals the presence of two types of cracks after tensile loading: (i) within the martensite matrix (with the formation, growth and coalescence of microvoids), and (ii) at delta ferrite/martensite interfaces (due to their poor bonding). The fractography analysis also indicated dimple mode ductile fracture.
- The Charpy notch impact energy values increased slightly with increasing welding speed from 0.75 m/min to 1.2 m/min both in as-welded and post welded conditions. After post weld tempering, the impact values were significantly enhanced compared to the as-

welded condition. At 1.2 m/min welding speed the impact value increased from 28.5 J to 45.5 J. The slightly higher impact energy with increasing the welding speed was observed and was attributed to the refined prior-austenite grains. The increase in charpy impact value after post weld tempering is mainly due to the formation of tempered martensite and reversed austenite. Fractographic analysis displays mixed dimple-quasi cleavage fracture modes with secondary cracks being present along the delta ferrite/martensite interface in the fusion zone.

The second step of this study involved root pass and multi-pass laser-arc welding of 25-mm thick martensitic stainless steels and the analysis and recommendations to solve the technical challenges experienced during root pass welding of thick plates.

- The most common welding defects detected during tandem and hybrid laser-arc root pass welding of 25 mm-thick martensitic stainless steel, using 5.2 kW laser power inside a narrow-gap groove design (5 mm root size with 27° full angle) were lack of penetration, lack of fusion, porosity and cracks. Lack of penetration was mostly related to the limited laser power. Lack of melting during tandem laser-arc welding, related to the narrow groove design, was resolved also using an optimum laser-arc distance of 6 mm and by applying HLAW on a laser root pass. Centerline hot cracking observed at the top of laser and GMAW in tandem beads is mainly related to the high carbon content of the base metal, high depth to width ratio of the weld inside the narrow groove and high cooling rate. Centerline hot cracking could be avoided by using a base metal with lower carbon content and controlling the depth to width ratio by reducing the wire feed speed.
- By increasing the laser power up to 15 kW and optimising the groove design (10 mm root size with 40° included angle), the lack of penetration and lack of fusion between GMAW and laser beads was resolved. However severe underfill and surface fluctuation at the bottom of the root appeared during laser and tandem laser-arc welding. This instability in the root pass was mainly due to the increase in evaporation and recoil pressure during high power laser welding. Optimising the laser power and laser-arc distance to 12 kW and 19 mm respectively could lead to the formation of a more stable root pass. Porosity and cracking were other imperfections detected in the weld cross sections. Porosities were formed mostly in irregular shape at the bottom of the hybrid laser-arc welding

filling passes due to the keyhole collapse. Longitudinal cracking was observed at the interface between carbide or oxide inclusions and the martensitic matrix.

- Transverse tensile testing was performed on full joint in top and bottom sections of the joint. The ultimate tensile and yield strength at the top and bottom of the weld could pass the minimum requirement. The elongations in top and bottom sections were 19% and 8% respectively, only the top part of the joint could pass the minimum requirement of 15%. The lower tensile property at the bottom of the root was due to the large pores inside the fusion zone at the weld bottom. Charpy impact test in the fusion zone performed for the root pass tandem laser-arc welding reached a high value of 88 J (for the sample fractured within the fusion zone) compared to Charpy tests of single pass hybrid laser-arc welds in as-welded condition. This could be due to the lower carbon content of 415 SS compared to CA6NM.

RECOMMENDATIONS FOR FUTUR WORK

This section presents some other aspects of the subject for further investigation in the future.

- To investigate the influence of different shielding gases (with addition of various oxygen content to argon) on penetration depth and Marangoni flow within the narrow groove configuration;

- To investigate the multiple effect of groove design, e.g. groove angle and root size on weld imperfection and Marangoni flow during hybrid and tandem laser arc welding of the root pass using both experimental and simulation approaches;

- To investigate the effect of laser-arc distance at different laser powers on the formation of hybrid or tandem weld pools using high speed camera to observe the interaction between laser and GMAW weld pools;

- To simulate the HAZ microstructure for low carbon martensitic stainless steel using Gleeble Thermomechanical system to predict continuous cooling transformation curves;

LIST OF BIBLIOGRAPHICAL REFERENCES

Bagger, C., and F.O. Olsen. 2005. « Review of laser hybrid welding ». *Journal of laser applications,* vol. 17, p. 2.

Cao, X., P. Wanjara, J. Huang, C. Munro and A. Nolting. 2011. « Hybrid fiber laser–Arc welding of thick section high strength low alloy steel ». *Materials & Design,* vol. 32, n^o 6, p. 3399-3413.

Carrouge, D. 2003. « Phase transformations in welded supermartensitic stainless steels ». *PhD thesis, University of Cambridge*.

Dilthey, U, F Luder and A Wieschemann. 1999. « Welding-Expanded capabilities in the welding of aluminium alloys with the laser-MIG hybrid process ». *Aluminium-Dusseldorf,* vol. 75, n^o 1, p. 64-75.

El Rayes, M., C. Walz and G. Sepold. 2004. « The influence of various hybrid welding parameters on bead geometry ». *Weld. J,* vol. 83, n^o 5, p. 147-153.

Folkhard, Erich, Günther Rabensteiner and Ernst Perteneder. 1988. *Welding metallurgy of stainless steels*, 98. Springer-Verlag Vienna, 6 p.

Gao, M., XY Zeng, QW Hu and J. Yan. 2008. « Weld microstructure and shape of laser–arc hybrid welding ». *Science and Technology of Welding & Joining,* vol. 13, n^o 2, p. 106-113.

Grünenwald, S, T Seefeld, F Vollertsen and M Kocak. 2010. « Solutions for joining pipe steels using laser-GMA-hybrid welding processes ». *Physics Procedia,* vol. 5, p. 77-87.

Jokinen, T., M. Karhu and V. Kujanpää. 2003a. « Welding of thick austenitic stainless steel using Nd: yttrium–aluminum–garnet laser with filler wire and hybrid process ». *Journal of laser applications,* vol. 15, p. 220.

Jokinen, Tommi, Miikka Karhu and Veli Kujanpää. 2003b. « Welding of thick austenitic stainless steel using Nd: yttrium–aluminum–garnet laser with filler wire and hybrid process ». *Journal of Laser Applications,* vol. 15, n^o 4, p. 220-224.

Kah, P. 2012. « Overview of the exploration status of laser-arc hybrid welding processes ». *Reviews on Advanced Materials Science,* vol. 30, n^o 2, p. 112-132.

Kah, P., A. Salminen and J. Martikainen. 2010. « The effect of the relative location of laser beam with arc in different hybrid welding processes ». *Mechanika,* vol. 3, n^o 83, p. 68-74.

Kim, CH, HS Lim and JK Kim. 2008. « Position welding using disk laser-GMA hybrid welding ». *J. Achiev. Mater. Manuf. Eng,* vol. 28, p. 83-86.

Kitahara, Hiromoto, Rintaro Ueji, Nobuhiro Tsuji and Yoritoshi Minamino. 2006. « Crystallographic features of lath martensite in low-carbon steel ». *Acta materialia,* vol. 54, n^o 5, p. 1279-1288.

Le Guen, E., R. Fabbro, M. Carin, F. Coste and P. Le Masson. 2011. « Analysis of hybrid Nd: Yag laser-MAG arc welding processes ». *Optics & Laser Technology,* vol. 43, n^o 7, p. 1155-1166.

Liu, Z., M. Kutsuna and G. Xu. 2006. « Microstructure and mechanical properties of co2 laser-mag hybrid weld of high strength steel-study on laser-arc hybrid welding of high strength steel (Report 2) ». *Quarterly journal of the Japan Welding Society,* vol. 24, n^o 4, p. 344-349.

Olsen, F.O. 2009. *Hybrid laser-arc welding*. CRC Press.

Paul, Christian, and Joni Nicolae. 2011. « Industrial applications for msg-laserhybrid welding process ». *Revista de Tehnologii Neconventionale,* vol. 15, n^o 4, p. 63.

Porter, David A, and Kenneth E Easterling. 2009. *Phase Transformations in Metals and Alloys, (Revised Reprint)*. CRC press, p. 66-71.

Qin, G.L.; Lei, Z.; Lin, S.Y. 2007. « Effects of Nd:YAG laser plus pulsed MAG arc hybrid welding parameters on its weld shape ». *Sci. Technol. Weld. Joining* vol. 12, p. 79-86.

Reutzel, E.W., M.J. Sullivan and D.A. Mikesic. 2006. « Joining pipe with the hybrid laser-GMAW process: weld test results and cost analysis *». Pennsylvania state univ university park applied research lab*.

Reutzel, EW, SM Kelly, MJ Sullivan, TD Huang, L Kvidahl and RP Martukanitz. 2008. « Hybrid laser-GMA welding for improved affordability ». *Journal of Ship Production,* vol. 24, n^o 2, p. 72-81.

Ribic, B, TA Palmer and T DebRoy. 2009. « Problems and issues in laser-arc hybrid welding ». *International materials reviews,* vol. 54, n^o 4, p. 223-244.

Sokolov, Mikhail, Antti Salminen, Mikhail Kuznetsov and Igor Tsibulskiy. 2011. « Laser welding and weld hardness analysis of thick section S355 structural steel ». *Materials & Design,* vol. 32, n^o 10, p. 5127-5131.

Song, Yuanyuan, Xiuyan Li, Lijian Rong and Yiyi Li. 2011. « The influence of tempering temperature on the reversed austenite formation and tensile properties in Fe–13% Cr–

4% Ni–Mo low carbon martensite stainless steels ». *Materials Science and Engineering: A,* vol. 528, n° 12, p. 4075-4079.

Steen, W.M. 1980. « Arc augmented laser processing of materials ». *Journal of Applied Physics,* vol. 51, n° 11, p. 5636-5641.

Steen, W.M. and M. Eboo. 1979. « Arc augmented laser welding ». *Metal construction,* vol. 11, n° 7, p. 332-335.

Thibault, D. 2010. « Contribution a l'etude du comportement en fatigue des aciers inoxydables 13% Cr-4% Ni: Contraintes residuelles de soudage et transformation sous contrainte de l'austenite de reversion ». École de technologie supérieure.

Vollertsen, Frank, Mr Stefan GrÜnenwald, Michael Rethmeier, Ing Andrey Gumenyuk, Uwe Reisgen and Ing Simon Olschok. 2010. « Welding thick steel plates with fibre lasers and GMAW ». *Welding in the World,* vol. 54, n° 3-4, p. R62-R70.

Webster, S., JK Kristensen and D. Petring. 2008. « Joining of thick section steels using hybrid laser welding ». *Ironmaking & Steelmaking,* vol. 35, n° 7, p. 496-504.

Zhang, Linjie, Xiaolong Gao, Mengjun Sun and Jianxun Zhang. 2014a. « Weld outline comparison between various pulsed Nd: YAG laser welding and pulsed Nd: YAG laser–TIG arc welding ». *The International Journal of Advanced Manufacturing Technology,* vol. 75, n° 1-4, p. 153-160.

Zhang, Mingjun, Genyu Chen, Yu Zhou and Shenghui Liao. 2014b. « Optimization of deep penetration laser welding of thick stainless steel with a 10kW fiber laser ». *Materials & Design,* vol. 53, p. 568-576.

Zhao, L., T. Sugino, G. Arakane and S. Tsukamoto. 2009. « Influence of welding parameters on distribution of wire feeding elements in CO 2 laser GMA hybrid welding ». *Science and Technology of Welding & Joining,* vol. 14, n° 5, p. 457-467.